NTNU
Norwegian University of
Science and Technology

Towards a New Ceramic-Glass Fiber Femtosecond Laser in the 2-3 Micrometer Wavelength Range

Cr2+ Doped Ceramic Glass Fibers and
Graphene Saturable Absorber Mirrors

Marte Bondø Augdal

ABSTRACT

Solid-state lasers, and in particular fiber lasers, are becoming the most commonly used lasers in science and industry, next only to diode lasers. This work has targeted the development of two novel types of laser active and passive media, an active medium based on Cr:ZnSe ceramic glass fibers, and a graphene based silver saturable absorber mirror. These are the two most important constituent parts of a novel type of broadband femtosecond fiber laser operating in the very interesting wavelength range between 2.2 and $2.6\,\mu$m.

The main challenge in developing a broadband glass fiber active medium lies in the fact that fiber lasers are usually doped with rare-earth ions. These ions preserve their preferred valency also in the amorphous structure of the fiber laser, but yield narrowband lasers operating only at specific wavelengths. To develop a broadband, tunable laser, transition-metal ions must be used. However, the aliovalent nature of these ions means that direct incorporation into a glass matrix leads to a range of valencies of the ions, inhibiting laser action. To overcome this problem, in this work a new methodological approach was applied to solving this problem – incorporation of ZnSe crystal micro-particles doped with Cr^{2+} into a phosphate glass matrix, retaining the valency of Cr^{2+} in the fixed local ZnSe crystalline environment of the ion.

To develop this new ceramic glass fiber, a number of technological steps have been undertaken.

- A standard melting technique was employed to fabricate phosphate glasses with low melting temperatures, and for incorporation of Cr:ZnSe into the glass matrix. This yielded the first reported successful incorporation of Cr:ZnSe particles in phosphate glasses, where the glasses were shown to retain the spectroscopic and luminescent properties of Cr:ZnSe.

- As the Cr:ZnSe micro-particles initially showed signs of dissociation at the high temperature, reducing the time of the Cr:ZnSe spent in the melted glass was identified to be a critical issue.

To further characterise the developed material, a number of characterisation steps have been undertaken:

- Absorption and fluorescence spectroscopy was performed. The fluorescence spectra showed

spectra characteristic of Cr:ZnSe, and an emission cross-section of the order of $10^{-18}\,\text{cm}^2$ was obtained at $2000\,\text{nm}$.

- A cut-back loss measurement technique showed that the losses in the glass were non-uniform across the samples, originating from the non-uniform distribution of Cr:ZnSe particles in the glass matrix. Large agglomerations of Cr:ZnSe particles led to large scattering losses, while regions of finely incorporated particles ($< 1\,\mu\text{m}$) showed low losses.

- The gain was calculated and compared with the losses. The average losses over the sample, of $\sim 6\,\text{cm}^{-1}$ at $2000\,\text{nm}$, were slightly higher than the measured gain of $\sim 4\,\text{cm}^{-1}$, showing loss reduction as the critical parameter to focus on in order to achieve an efficient gain material. Areas of finely incorporated particles showed losses below $1\,\text{cm}^{-1}$, showing that with homogeneous distribution of particles, the material will become even better as a laser material.

- Differential scanning calorimetry measurements were performed to identify the glass transition temperature $T_G \approx 300^\circ\,\text{C}$, and Raman spectroscopy of the glasses were used to identify the Cr:ZnSe Raman peaks in the phosphate glass matrix.

The spectroscopic study shows the good prospects of this material as a laser material.

For creation of ultra-short pulses in the broadband fiber laser, a passive laser element - a saturable absorber - should be developed and incorporated into the laser. Graphene saturable absorbers on silver mirrors were created, and used to successfully mode-lock a Cr:ZnS laser. In particular, the following technological and characterisation steps were undertaken:

- The graphene mirrors were fabricated by transferring CVD grown graphene from a Cu foil onto the silver mirror substrate by a standard transfer process. The process showed to be highly dependent on the handling of the materials, making it prone to human error. Difficulties with the adhesion of graphene to the underlying substrate were due to variations in the heat treatment, where soft baking on a hot plate made the process dependent on thickness and thermal conductivity of the substrate.

- The graphene saturable absorber on a silver mirror was used to successfully mode-lock a Cr:ZnS laser, yielding pulses of $109\,\text{fs}$ with an input laser power of 3W. The saturation energy fluence of the graphene saturable absorber mirror was calculated at $4.8\,\mu\,\text{J/cm}^2$, significantly lower than commonly reported values, but agreeing with the observed trend that the saturation energy fluence decreases with increasing wavelength.

Summarising, the undertaken approach towards development of a novel ceramic glass fiber laser proved to be successful, and allowed to make two main conclusions:

1. The developed ceramic glass fiber, preserving the valency of the active ions, showed promising spectral-luminescent properties as a laser active medium.

2. The developed passive saturable absorber based on graphene mirrors demonstrated very good laser performance and could be used in the future ceramic glass fiber laser.

SAMMENDRAG

Faststoff-lasere, og spesielt fiberlasere, er i ferd med å bli en av de mest brukte laserne innenfor vitenskap og teknologi, bare overgått av diodelasere. Denne oppgaven har fokusert på utvikling av to nye typer aktive og passive lasermedier, et aktivt medium basert på keramiske glassfibre med inkorporerte Cr:ZnSe mikropartikler, og et grafen-basert saturable absorber-sølvspeil. Disse er de to viktigste bestanddelene i en ny type femtosekund fiberlaser, som opererer i det veldig interessante bølgelengdeområdet mellom 2.2 og $2.6\,\mu m$.

Hovedutfordringen ved å utvikle et aktivt glassfibermateriale med bred båndbredde, ligger i det at fiberlasere vanligvis er dopet med jordalkalimetaller. Disse ionene bevarer sin foretrukne valens også i den amorfe strukturen til en fiberlaser, men gir en small båndbredde og lasere som opererer bare ved gitte bølgelengder. For å utvikle en bredbånd, tunbar laser, overgangsmetaller må brukes. Den aliovalente naturen til disse ionene betyr at direkte inkorporering i en glassmatrise gir ioner med et spekter av valenser, noe som demper laseraktiviteten.

For å overkomme dette problemet, har vi i denne oppgaven brukt en ny metodologisk framgangsmåte for å løse problemet - inkorporering av krystallinske ZnSe-mikropartikler dopet med Cr^{2+} i fosfatglass, som gjør at Cr^{2+} beholder valensen sin ved å inkorporeres i én bestemt posisjon i ZnSe-krystallen.

En rekke teknologiske steg har blitt gjennomført for å utvikle det nye keramiske glasset:

- En standard smelteteknikk ble benyttet for å fabrikere fosfatglass med lav smeltetemperatur, og for inkorporering av Cr:ZnSe-partikler i glassmatrisen. Dette resulterte i den første rapporterte suksessfulle inkorporeringen av Cr:ZnSe-partikler i fosfatglass, hvor glasset viste seg å beholde de spektroskopiske og luminescerende egenskapene til Cr:ZnSe.

- Siden Cr:ZnSe i begynnelsen viste tegn til å dissosiere ved høye temperaturer, har det å redusere tiden Cr:ZnSe-partiklene tilbringer i det smeltede glasset blitt identifisert som kritisk.

For å videre karakterisere det utviklede materialet, har en rekke karakteriseringssteg blitt gjennomført:

- Absorpsjons- og florescens-spektroskopi ble gjennomført. Fluorescens-spektraene viste

spektra karakteristisk for Cr:ZnSe, og et emisjons-tverrsnitt (emission cross-section) av størrelsesorden 10^{-18} cm^2 ble funnet ved 2000 nm.

- En cut-back tapsmålingsteknikk viste at tapene i glasset ikke var uniformt fordelt over prøven, på grunn av den ikke-uniforme fordelingen av Cr:ZnSe-partikler i glasset. Store klumper av Cr:ZnSe-partikler førte til store spredningstap, mens områder med små, fint fordelte partikler ($< 1\,\mu$m) viste små tap.

- Forsterkning (gain) ble beregnet og sammenlignet med tap. Gjennomsnittstapet over prøven, på $\sim$6 cm^{-1} ved 2000 nm, var litt høyere enn den målte forsterkningen på $\sim$4 cm^{-1}, noe som viser at tapsreduksjon er en kritisk parameter å fokusere på for å oppnå et materiale med effektiv forsterkning. Områder med fint fordelte partikler viste lavere tap, under 1 cm^{-1}, noe som viser at med homogen distribusjon av partikler vil materiale fungere enda bedre som et lasermateriale.

- Differential scanning calorimetry-målinger ble gjennomført for å finne glassovergangstemperaturen (glass transition temperature) $T_G \approx 300°$ C, og Raman-spektroskopi ble benyttet til å identifisere Raman-topper fra Cr:ZnSe i fosfatglassprøvene.

De spektroskopiske undersøkelsene gjennomført viser at materialet har gode utsikter som et lasermateriale.

For å skape ultra-korte pulser i bredbånds-fiberlaseren, må et passivt element - en saturable absorber - utvikles og inkorporeres i laseren. Grafen saturable absorbers på sølvspeil ble utviklet, og brukt til å mode-locke en Cr:ZnS laser. De følgende fabrikasjons- og karakteriserings-stegene ble gjennomført:

- Grafenspeilene ble fabrikert ved å overføre CVD-grodd grafen fra Cu-folie til sølvspeilsubstratet ved en standard overføringsteknikk. Prosessen viste seg å være svært avhengig av håndteringen av materialene, noe som gjorde den sårbar for menneskelige feil. Vanskeligheter med adhesjon av grafen til det underliggende substratet kom av variasjoner i varmebehandlingen, hvor baking på en varmeplate gjorde prosessen avhengig av tykkelsen og varmeledningen til substratet.

- Den utviklede saturable absorberen av grafen på sølvspeil ble brukt til å suksessfult mode-locke en Cr:ZnS laser, noe som ga 109 fs pulser med en input-effekt på 3W. Saturation energy fluence av graphenespeilet ble beregnet til 4.8μ J/cm^2, signifikant lavere enn ofte rapporterte verdier, men i overenstemmelse med den observerte trenden at saturation energy fluencen reduseres med økende bølgelengde.

For å oppsummere, den benyttede tilnærmingen til utvikling av en helt ny keramisk glassfiberlaser viste seg å være suksessful, og gjorde det mulig å trekke følgende konklusjoner:

1. Den utviklede keramiske glassfiberen, som beholdt valensen til det aktive ionet, viste lovende spektral-luminescente egenskaper som et aktivt lasermateriale.

2. Den utviklede passive saturable absorberen basert på grafenspeil demonstrerte veldig god ytelse i en laser, og kan bli brukt i den fremtidige keramiske glassfiberlaseren.

PREFACE

This Master's thesis is the result of the author's work in the course TFY4905, Nanotechnology research project, comprising a workload of 30 ECTS credits, at the Department of Physics, NTNU.

As a Nanotechnology student specialising in Nanoelectronics, my main interest has long been in condensed matter physics, especially on the electronic and optical properties of materials. Writing a Master's thesis about laser physics seemed appropriate, as the field combines challenges in both material science and physics.

Even though lasers have been around for decades, the field still comprises challenges, and new limits are pushed every day to develop lasers with more power, shorter pulses and larger tunability. Taking part in development of novel materials that no one has ever before succeeded in has been highly motivating, and I take pride in being part of pushing human knowledge and technology forward.

I have used knowledge from my interdiciplinary background in physics, chemistry and materials science when writing this Master's thesis. In spite of hard work, I have enjoyed this period and learned a lot.

Trondheim
August 2017

Marte Bondø Augdal

Contents

List of Figures

List of Tables

Nomenclature

APS	Ammonium peroxydisulfate
CW	Continuous wave
DSC	Differential scanning calorimetry
FOM	Figure of merit
NZP	Phosphate glasses with elements PO_3, Na and Zn
PMMA	Polymethyl metacrylate
RE	Rare-earth ion
SA	Saturable absorber
TM	Transition-metal ion

1   INTRODUCTION AND MOTIVATION

Solid-state lasers, and in particular fiber lasers are rapidly becoming a "workhorse" of the laser technology, and are the most commonly used laser in science and industry, next only to diode lasers. Cheap fabrication and ease of use has made them easily accessible lasers, operating at a range of wavelengths and output powers [1]. As fiber lasers are commonly doped with rare-earth ions, they are naturally narrowband and operate only at specific wavelengths. While fiber lasers around 2 µm and around 3 µm already exist, a broadband, tunable fiber laser in the entire region between 2 and 3 µm has not yet been developed.

Broadband lasers, and ultrashort pulsed femtosecond lasers, are typically solid-state crystal lasers found in laboratories. These lasers are rather expensive and difficult to operate, making them hardly accessible for real-world applications, including industrial applications.

Developing a broadband and tunable fiber lasers, operating in the region between 2 and 3 µm would lead to a range of possible scientific and industrial applications. This laser would cover both the range of water absorption and the water-free wavelength range, making differential absorption measurements in living tissue and gases possible, and so be interesting for medical applications and sensors in the oil and gas industry [2]. Moreover, a broadband fiber laser could be used to create ultrashort pulses directly inside the fiber laser, currently only possible in more bulky and expensive crystalline lasers.

In the last decades, researchers have made numerous attempts at developing a broadband transition-metal doped fiber laser, mostly without success. The exception is a successful example of a tunable bismuth doped fiber laser [3], that allow broadband tunable operation around 1.3 µm This fiber laser still remain in the research phase.

Creating a broadband or ultrashort pulsed fiber laser faces physical and technological challenges. As of now, only rare-earth ions are used as active ions in fiber lasers. These ions are incorporated in the trivalent state, which is the preferred valency for rare-earth ions, and their properties do not depend on which host they are substituted into. This makes them suitable for incorporation into non-crystalline materials used to make fibers. These ions exhibit high gain, but also a narrow bandwidth, making it hard to create ultrashort pulses or broad tuning. For this end, one needs transition metal ions.

Transition metal ions yield a broadband emission, and can be used to create femtosecond pulsed lasers. The challenge lies in their aliovalent nature, where they easily change valency when incorporated into glasses. Preserving the desired valency is challenging. As the experience with bismuth glasses have shown [4], direct incorporation of transition metal ions into an amorphous fiber laser leads to a range of different valencies of the ions.

This is the main reason why broadband and femtosecond mid-infrared fiber lasers have currently not been realized.

To overcome the physical challenges, a novel approach to fabrication of a glass fiber is suggested in this work. The approach combines the advantages of the glass fiber and that of the crystalline host, where the valency of a transition metal ion is conserved by incorporation into a specific lattice site in the crystal.

Proposed solution

Transition-metal ions, in our case chromium, incorporated into a crystal powder preserve their valency. Subsequently introducing this powder into glass yields a gain material composed of a glass-ceramic composite that can be used to draw a fiber, and is therefore a promising solution to creating a transition metal doped glass fiber. This is fundamentally different to introducing transition-metal ions directly into the glass matrix, and resolves the issue of aliovalency in chromium.

In addition, to realize a short-pulsed mode-locked laser, a good passive saturable absorber material is needed. Graphene has proved itself to be a good and reliable saturable absorber with low saturation energy fluence [5, 6]. Such graphene saturable absorber mirrors have also been demonstrated to work in fiber lasers, creating a mode locked regime and a pulsed laser [7].

It was our intention to explore both of these approaches in this work - fabrication of a novel type of gain materials, and of graphene saturable absorber mirrors.

Major goal

The long term goal of this work is the development of a new type of ultrashort pulsed fiber laser. The laser would combine the robustness and user-friendliness of a fiber laser and the advanced ultra-short pulsed performance of a crystalline laser.

To this end, the thesis has focused on development and characterisation of a new type of gain material based on Cr:ZnSe micro-crystal doped phosphate glass fiber, and a new type of semiconductor graphene saturable absorber deposited on silver mirrors for pulse generation.

Specific objectives

In order to achieve the main goal, the following specific objectives were accomplished:

- Analysis of relevant literature
- Fabrication of pure phosphate glasses
- Doping of phosphate glasses with Cr:ZnSe micro-particles
- Spectroscopic characterisation of doped phosphate glasses
- Measurement and quantitative estimation of emission cross-section and losses
- Fabrication of a graphene saturable absorber on silver mirror
- Demonstration of mode locking
- Determination of pulse length and saturation energy fluence
- Analysis of obtained data for evaluation of the usability of the materials for laser purposes and correctness of the chosen approach

Results

Both aims - development and characterisation of the novel type of active gain material and of passive graphene saturable absorber mirrors, have been successfully realized.

Looking at the preceding literature, attempts by our colleagues at the Applied Physics Institute in Nizhnyi Novgorod at incorporating micro- and nano-crystals of Cr:ZnSe into chalcogenide glasses, showed a problem of dissociation of the micro- and nano-crystals in the high fabrication temperatures [8–10]. To resolve this issue, in this work micro- and nano-particles of Cr:ZnSe have been incorporated into phosphate glass, having a significantly lower melting temperature than chalcogenide glasses.

Although temperature is still a challenge, we have been able to demonstrate, for the first time, that the spectral-luminescent properties of the Cr:ZnSe crystals have been preserved inside the glass, showing that Cr has preserved its divalent state. This shows a possibility for resolving the problem of Cr taking on a range of valencies when incorporated in glass.

The challenge of dissociation of the micro-particles is still present, but a promising route to overcome this problem is presented in this work. The spectral and luminescent properties of the active material indicate its potential applicability as a laser material, although the losses in the material are yet to be reduced.

In the second part of the work, graphene saturable absorber mirrors have been created by transferring graphene onto a silver mirror.

The suggested fabrication technology of graphene saturable absorbers on silver mirrors yielded promising results, with the first mode-locked laser pulses obtained in a Cr:ZnS laser using this new mirror being demonstrated. A low saturation energy fluence of the fabricated graphene mirror was experimentally established, indicating correctness of our technological approach and usefulness of the developed mirror in the future compact all-fiber mode-locked laser.

Although not yet realized as a mode-locked all-fiber laser, the obtained first results indicate a very promising beginning.

Structure of the thesis

This thesis presents the results of the fabrication and the study of the spectral luminescent properties of two novel active and passive laser elements, based on micro-crystal doped glass-ceramic fibers and graphene saturable absorbers. The work has been done as part of the long term research effort aimed at developing a novel type of femtosecond pulsed glass-ceramic-fiber laser operating in the broad wavelength range between 2 and 3 µm.

The thesis is structured as follows:

Chapter 1 gives introductory comments, including motivation, problem setting, overall goal and specific objectives, as well as an account of the achieved results.

Chapter 2 focuses on the theoretical aspects of lasers relevant to this thesis, presents the difference between crystalline and fiber lasers, and gives a review of the current literature in the area.

Chapter 3 presents a brief theoretical description of the experimental methods for fabrication and characterisation of the fiber laser elements.

Chapter 4 provides details of the methodology of fabrication and characterisation of the fiber laser elements, and of testing of the samples in an existing laser setup.

Chapter 5 quantitatively describes the obtained experimental results, and uses them in quantitative estimations of critical values interesting for the laser materials.

Chapter 6 provides the analysis and discussion of the results with respect to applicability of the created active and passive elements in the targeted mode-locked laser, and suggests the strategy for future improvements.

Chapter 7 provides a summary of the thesis, listing the obtained results and highlighting the novel functional aspects of the developed materials and graphene structures, as well as providing an outlook for the future work needed to be done in order to realize an all-fiber broadband mid-IR laser source.

2   THEORETICAL AND EXPERIMENTAL BACKGROUND

The first section gives an introduction to the principles behind a laser. It begins by explaining the optical processes in a laser responsible for creating gain. The four-level scheme characteristic for transition metal ions, pump threshold, absorption and gain saturation are discussed. The section finishes by explaining principles of pulse generation.

The second section contains the theory needed to understand the fundamental difference between crystalline and fiber lasers, and why we are interested in merging their properties to create a new fiber laser material with a new functionality - broad bandwidth. The section starts with an introduction to different types of host materials, and explains how the crystalline field of the host material affects the active ions. Then the electronic properties of the active ions are described, with focus on the difference between rare-earth and transition-metal ions. The section finishes by summarising the fundamental differences between fiber lasers and crystalline lasers.

The third section presents the properties of the laser materials most relevant for this work.

The fourth section gives an overview of the current literature on ion doped fiber lasers, crystalline lasers and crystalline powder lasers, along with graphene saturable absorbers, that serves as the basis for development of this work. It begins with an overview of fiber lasers doped with rare-earth and transition-metal ions. Then lasing in nano-crystalline powders is demonstrated, and articles on incorporation of such nano-particles in glass are presented. Crystalline Cr:ZnSe lasers are presented as a motivation for choosing this particular micro-crystalline material to incorporate into phosphate glasses. In the end, articles on graphene saturable absorbers showing femtosecond pulse generation and mode-locking of fiber lasers are presented.

2.1   Laser Principles

A laser consists of an active medium that stores energy, surrounded by a resonant cavity. The energy is delivered by a pump source, which can be a flashlamp, a diode laser, another fiber or solid-state laser, or some other arrangement. Figure 1 shows a principal schematic of the laser components.
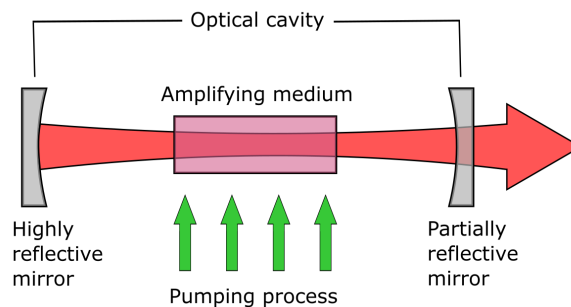
Figure 1: Schematic overview showing the main components in a laser

The active medium consists of a host material, with mechanical, thermal and optical properties making it capable of withstanding the stresses encountered during the laser operation while still transmitting light, and an active ion, capable of absorbing, storing and emitting light energy in a coherent way.

In more sophisticated mode-locked lasers, the cavity also incorporates a passive element – a saturable absorber (SA). Along with the active medium, these two are the most important elements of the future fiber laser that we aim to develop, and are therefore the focus of the present work.

Laser is an acronym for light amplification by stimulated emission of radiation. As the name implies, a laser emits light by the process of stimulated emission. For stimulated emission to occur a population inversion is needed, where more electrons are found in the excited state than in the ground state. To achieve population inversion, the active medium is placed in a resonant cavity. For solid state lasers the cavity is usually made by placing the active material between two mirrors. One mirror is completely reflective, while the other mirror transmits a small portion of the light, creating the output beam. With every pass through the active material the light is amplified, until population inversion is achieved and lasing can begin.

2.1.1   Absorption and Emission Processes

[1]An atom or molecule with two energy levels can emit or absorb energy according to different processes: spontaneous emission, non-radiative decay, stimulated emission and absorption. Figure 2 shows a schematic illustration of the three radiative processes.
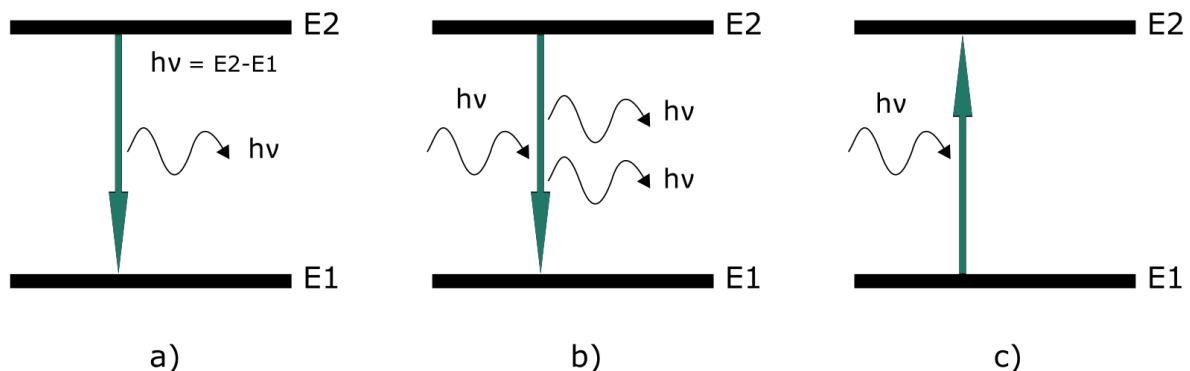
Figure 2: Schematic illustration of the three radiative processes in a laser medium. a) Spontaneous emission. b) Stimulated emission. c) Absorption

For an atom with energy levels where $E_1 < E_2$, an atom in level 2 will tend to decay to level 1. This can happen spontaneously, in a process known as spontaneous (or radiative) emission. The energy difference $E_2 - E_1$ is released in the form of a photon of energy $h\nu_0 = E_2 - E_1$. A second spontaneous decay mechanism is non-radiative decay, where the energy difference $E_2 - E_1$ is released as a phonon in the material. A third possibility is an incident electromagnetic wave of frequency $\nu = \nu_0$, forcing the atom to release its energy and undergo stimulated emission. The energy difference is delivered as a photon with the same frequency, phase and direction as the incident photon.

In the case of spontaneous emission, the atom emits a photon in an arbitrary direction. For

---

[1]This section is based on reference [11]

stimulated emission, the photon adds to the phase and direction of the incoming wave, creating a coherent wave of photons.

An atom initially in energy level 1, will remain in this level until some external stimulus is applied to it. For an incident photon of frequency $\nu = \nu_0$, there is a finite probability that the atom will be excited to level 2. This is called absorption.

Transition cross-sections

The probabilities of optical transitions are determined by the transition cross-sections. The transitions depend on the wavelength, and typically a resonance wavelength can lead to a strong peak in the cross-section. For a laser gain medium, the absorption cross-section at the pump wavelength, and the emission cross section at the laser wavelength, are the most relevant cross-sections.

The probability of absorption depends on the amount of atoms in the lower energy level, N_1, the photon flux F in the material, and the absorption cross-section σ_{abs} of the material, by

$$\left(\frac{dN_1}{dt}\right)_{abs} = -\sigma_{abs}FN_1$$

If N ions in a medium with an absorption cross-section σ_{abs} absorb energy, the absorption coefficient is given by $\alpha_{abs} = \sigma_{abs}N$.

The probability of stimulated emission is in an equivalent way given by

$$\left(\frac{dN_2}{dt}\right)_{em} = -\sigma_{em}FN_2$$

where σ_{em} is the emission cross-section of the material. The gain coefficient for a medium with emission cross-section σ_{em} is given by

$$g = \sigma_{em}n_2N \tag{1}$$

where n_2 is the achievable fraction of excitation.

Typical values of the absorption and emission cross-sections of a laser crystal, are in the range $10^{-18} - 10^{-20}\mathrm{cm}^2$. Ions in glasses often show smaller cross-sections due to inhomogeneous broadening.

A measure of the transition cross-sections can be obtained from the absorption and emission spectra of a material. The absorption cross-section can be calculated from the absorption spectra of a material with known ion concentration. The fluorescence spectra can be used to obtain the spectral profile of the emission cross-section, given that no reabsorption processes occur.

The value of the emission cross-section can be calculated using the Füchtbauer-Ladenburg equation [12, 13]:

$$\sigma_{em}(\lambda) = \frac{1}{8\pi n^2 c \tau_r} \frac{\lambda^5 I(\lambda)}{\int I(\lambda)\lambda d\lambda} \tag{2}$$

$I(\lambda)$ is the fluorescence spectrum of the sample, and τ_r is the radiative lifetime of the material, the lifetime measured when only spontaneous emission depopulates the laser level.

For the non-stimulated processes of spontaneous emission and non-radiative decay, the probabilities of the processes occurring are determined by

$$\left(\frac{dN_2}{dt}\right)_r = \frac{N_2}{\tau_r}$$

$$\left(\frac{dN_2}{dt}\right)_{nr} = -\frac{N_2}{\tau_{nr}}$$

where τ_{nr} is the non-radiative decay lifetime.

2.1.2 Laser Gain

For a material to lase, a net gain in laser photons is needed when a plane wave passes through a section of the active material, and the gain needs to exceed the loss.

The change in photon flux F of a plane wave travelling through an active material of length l, will be given by the difference between stimulated emission events creating photons, and loss processes removing photons, per unit time.

Losses in the laser cavity include losses due to output coupling of light, and internal losses in the material. With R_1 and R_2 being the reflectance of the cavity mirrors, and α_{loss} the absorption (loss) coefficient at laser wavelength, a beam of initial photon flux F_0 will in one round trip have achieved the photon flux

$$F_2 = F_0 R_1 R_2 \exp[2l\sigma_{em}(N_2 - N_1) - 2l\alpha_{loss}] \tag{3}$$

The round-trip gain, G, is given as $G = F_2/F_0$. The threshold condition for laser oscillation is $G = 1$, which gives the critical inversion

$$N_c = N_2 - N_1 = \frac{\alpha_{loss}}{\sigma_{em}} + \frac{1}{2l\sigma_{em}} \ln\left(\frac{1}{R_1 R_2}\right)$$

The critical inversion N_c is the population inversion needed to start and maintain oscillation. The first term in the equation is due to the losses inside the cavity, while the second term is the losses due to the mirror transmission.

Losses in non-ideal lasers

In an ideal laser, the only losses originate from absorption in the gain medium and output coupling. In reality, several non-radiative decay processes lead to losses in the resonator. On a round-trip, the attenuation will amount to a reduction in the flux equal to $\exp(-2l\alpha_{loss})$, as found in Equation (3).

The combined effect of radiative and non-radiative processes means that the time variation of the upper state population N_2 can be written as

$$\frac{dN_2}{dt} = -\left(\frac{N_2}{\tau_r} + \frac{N_2}{\tau_{nr}}\right) = \frac{N_2}{\tau}$$

where $\frac{1}{\tau} = \frac{1}{\tau_r} + \frac{1}{\tau_{nr}}$.

When measuring the decay of spontaneously emitted light from a sample experimentally, one measures the overall lifetime τ. τ_r and τ_{nr} can be found by also measuring the quantum efficiency, $\eta_Q = \frac{\tau}{\tau_r}$, defined as the percentage of input photons that leads to radiative emission.

2.1.3 Laser Schemes

[2]A strong light flux is not in itself sufficient to create laser action. For a material with two laser levels 1 and 2, the condition $N_1 \geq N_2$ is always fulfilled at thermal equilibrium.

---

[2]This section is based on reference [14]

To obtain a population inversion, the laser system needs more than two levels. Laser schemes commonly uses three or four levels, as shown schematically in Figure 3. In a four-level scheme, the atom is excited from the ground level 0 to the upper level 3, where it rapidly decays to level 2. A population inversion is achieved between level 2 and 1, before the atom again rapidly decays from level 1 to 0. The three-level scheme works in a similar fashion, except that population inversion is achieved between level 2 and 0 (level 1 is absent in the three-level scheme).
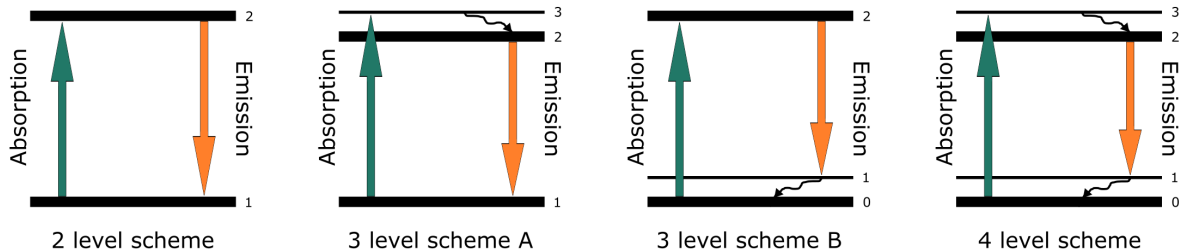
Figure 3: Two, three and four level laser schemes

The advantage of the four level scheme over the three level scheme is that a population inversion is easily achieved. In a three level laser scheme, one needs $N_2 > N_1$ for population inversion to be achieved. In a four level laser, any atom raised to the upper laser level creates a population inversion, as the short lifetime of level 1 leaves it almost completely empty.

The upper laser level decouples the pump and laser fields. By storing energy in the upper laser level, the fields are decoupled. The pump and laser radiation have different wavelengths, so they are decoupled in frequency (this is called Stokes shift or Stokes loss). The direction and polarization of the laser light might be independent of the direction and polarization of the pump energy, decoupling the laser and pump in space.

Pump threshold

The minimum intensity needed in a pump to initiate laser action is given by

$$I_{th}^{pump} = F \cdot h\nu^{pump} = \frac{\alpha_{loss}}{\alpha_{pump}} \frac{h\nu}{\sigma_{em}\tau} \frac{\nu^{pump}}{\nu} \tag{4}$$

From this expression, it can be seen that a high emission saturation intensity ($h\nu/\sigma\tau$) increases the pump threshold. An increase in Stokes shift ($h\nu^{pump}/h\nu$), giving the loss of photon energy in the laser process, also increases the threshold. The figure of merit (FOM) ($\alpha_{pump}/\alpha_{loss}$), shows the ratio of absorbed pump power that is transferred into losses. High losses result in a low figure of merit. FOM scales inversely with the pump threshold, meaning a higher FOM reduces the pump threshold.

In the absence of non-radiative decay, $\tau = \tau_r$, where

$$\frac{1}{\tau_r} = 8\pi c n^2 \sigma_{em}(\lambda_0) \frac{\Delta\lambda}{\lambda_0} \frac{1}{\lambda_0^3}$$

giving a threshold pump intensity

$$I_{th} \propto \frac{1}{FOM} \frac{\Delta\lambda}{\lambda_0} \frac{n^2}{\lambda_0^4} \tag{5}$$

The factor λ^4 in the denominator decreases the threshold for longer wavelengths, lowering the threshold for transitions in the mid-IR. This means that laser action is more easily achieved in

the IR range. The threshold pump intensity also scales with the bandwidth $\Delta\lambda/\lambda_0$, meaning that broadband materials often have high thresholds. To achieve a broadband material without a very high threshold pump intensity, it is advantageous if the transitions happen in the mid-IR range.

Absorption and gain saturation
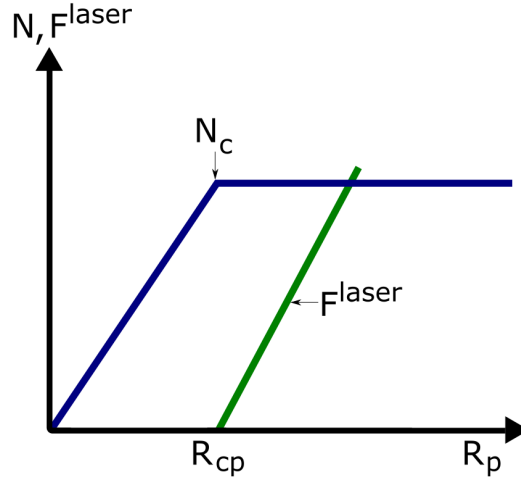
Figure 4: Qualitative representation of the population inversion N and the photon flux F^{laser} in the material, as a function of pump rate R_p

[3] After lasing has started, an increase in pump rate $R_p = \sigma_{abs}F^{pump}N_0$ yields an increased flux in the material, but not a higher population inversion. Figure 4 shows a qualitative representation of this relationship.

As the laser flux in the material is increased, the material's ability to absorb energy is reduced. The absorption saturation intensity is defined as the intensity where the material's absorption α is only 50% of the absorption at threshold, α_0. The value of the absorption coefficient is given by

$$\alpha(I) = \frac{\alpha_0}{1 + I/I_{sat}}$$

In a four-level scheme, the absorption saturation intensity I_{sat}^{abs} is given by

$$I_{sat}^{abs} = \frac{h\nu}{\sigma\tau}$$

Gain in a laser material saturates as well. The increase in F^{laser} does not increase linearly with F^{pump}, as the losses in the material becomes more prominent with increasing laser flux. The gain saturation intensity is the intensity where the gain in the material, g, is only 50% of the gain at threshold, g_0. The gain coefficient is given by

$$g(I) = \frac{g_0}{1 + I/I_{sat}}$$

where for a four-level laser,

$$I_{sat}^{gain} = \frac{h\nu}{\sigma\tau} \tag{6}$$

---

[3]This section is based on reference [15]

Knowing the emission cross-section σ_{em} and the radiative lifetime of a material, τ_r, one can estimate the gain saturation intensity I_{sat}^{gain}. Knowing the gain, the losses and the gain saturation intensity is sufficient to quantitatively evaluate if the material has prospects as a laser material or not.

2.1.4   Mode-Locking

So far continuous wave (CW) lasers have been discussed, producing a continuous output beam.

By applying a mode-locking technique, ultrashort laser pulses with a broad bandwidth can be obtained. These pulses can achieve high peak powers, as the entire output energy of the CW laser now is concentrated in an ultrashort pulse. The peak power can be as high as N times the average power of the laser, where N is the number of axial modes oscillating in the laser, typically on the order of a few hundred up to 10^6 [16].

The output of a laser typically shows wide fluctuations in irradiance, originating from the interference of longitudinal resonator modes with random amplitude and phase relations [17]. These random fluctuations can be transformed into a well-defined single pulse circulating in the laser resonator, by introduction of a non-linear material known as a saturable absorber (SA) into the cavity. We say then that the laser is passively mode-locked.

A peak of intensity near the value of the saturation intensity I_s of the SA, will experience lower amounts of losses than a peak of lower intensity. With a few passes of the laser radiation in the material, the low intensity fluctuations are completely dampened, and a single pulse oscillates in the laser.

The spectral distribution in the laser has now moved from a large number of discrete spectral lines of varying amplitude and random phase distribution, as seen in CW operation, to a fixed phase relationship and spectral intensity distribution. In the time domain, the laser has moved from a random intensity distribution characteristic of thermal noise, to an output of well defined pulse trains.

The radiation circulates inside the cavity with a repetition rate determined by the round-trip time of the cavity. Each time the pulse hits the output coupler mirror a pulse leaves the laser, giving a pulse repetition rate of $(c/2L)$, where L is the cavity length.

By Fourier's theorem, a short pulse of light can be considered as the sum of electromagnetic waves with a fixed phase relationship and a continuous range of frequencies, interfering destructively everywhere except for at the pulse peak. The larger the number of frequency components involved, the shorter the possible pulse duration [18]. The general relationship between the time and frequency is given by

$$\Delta \nu t_p \geq \psi$$

where t_p is the pulse duration and $\Delta \nu$ is the gain bandwidth of the laser, given at full-width-half-maximum of the intensity curve. ψ is of the order of unity, and depends on the pulse shape. For a sech^2 pulse, common in mode-locked lasers, $\psi = 0.31$. The width of the individual mode-locked pulses is limited to

$$t_p = \frac{0.31}{\Delta \nu}$$

This shows that generation of ultrashort pulses requires a broad bandwidth.

In addition to mode-locking by passive saturable absorbers, other types of mode-locking techniques exist. In Kerr lens mode-locking, a non-linear effect of a material is used where high laser irradiance produces an increase in the refractive index of the material, creating a self focusing

effect of the beam. An aperture in the cavity creates high losses for the unfocused CW beam, while ensuring high transmission for the self-focusing laser pulse.

The mode-locking obtained in this work is a combination of mode-locking by a saturable absorber and Kerr lens mode-locking. As the work focuses on development of a saturable absorber, this will be the focus of both the theory and discussion.

Saturable absorbers

Important parameters for the SA is saturation energy fluence, modulation depth and recovery time.

The modulation depth is the maximum possible change in optical loss, and so describes how much the light signal amplitude can be varied around its unmodulated value [19].

The recovery time is the decay time of the excitation after a pulse hits the SA. To achieve mode-locking, the saturable absorber needs a very short recovery time, on the order of the fluctuation itself [16].

The saturation energy fluence, J_{sat}, is the energy per unit area needed for saturation, i.e. the point where the absorption is $1/e$ of its initial value [20]. A low value of the saturation energy fluence means that mode-locking can be obtained at low intensities.

The saturation energy fluence can be estimated by measuring the minimum output power that sustains mode-locking in a laser. Equation (7) shows the calculation of J_{sat} from the output power P_{out}. Needed for the calculation are the beam spot size A on the saturable absorber, the repetition rate F_{rep} of the laser pulses, and T_{loss}, the transmission after accounting for losses in the output coupler and other losses.

$$J_{sat} = \frac{E_{intra}}{A} = \frac{P_{intra}}{F_{rep}}\frac{1}{A} = \frac{P_{out}}{T_{loss}}\frac{1}{F_{rep}}\frac{1}{A} \tag{7}$$

Non-linear optics

[4]Propagation of a light wave travelling in a medium is commonly described by a linear dependence of the polarization on the electric field of the light wave,

$$\mathbf{P} = \epsilon_0 \chi \mathbf{E}$$

In laser beams, the light irradiance can easily become large enough that the polarization response of the medium to the electric field is non-linear. At field strengths corresponding to the the field strength of an electron at about 1 Å from an ion, the non-linear polarization is significant. The polarisation is given by

$$\mathbf{P} = \epsilon_0(\chi \mathbf{E} + \chi^{(2)} \mathbf{E^2} + \chi^{(3)} \mathbf{E^3} + ...)$$

where χ is the normal linear susceptibility of the dielectric, and $\chi^{(2)}$, $\chi^{(3)}$, etc., are second, third and higher order terms.

The origin of the non-linear response is from the non-linear movement of the outer, more loosely bound electrons in the medium. Under strong electric fields, a non-linear equation of motion for the electron is needed, of the form

$$\ddot{x} + \omega_0^2 x + \alpha x^2 = \frac{e}{m}E\cos\omega t$$

---

[4]This section is based on reference [17]

leading to an induced polarization

$$P = \epsilon_0(\chi E_0 \cos \omega t + \chi^{(2)} E_0^2 \cos^2 \omega t + \chi^{(3)} E_0^3 \cos^3 \omega t + ...)$$

The polarisation P oscillates at harmonics 2ω, 3ω, ..., and radiates waves at these higher frequencies. This leads to interesting possibilities using non-linear optics.

While a range of second order non-linear processes exist, only the third order non-linear processes are relevant for this work. A third order non-linear process is applied in Kerr lens mode-locking, where the non-linear refractive index n_2 is used to achieve the self-focusing effect described earlier.

2.2 Laser Materials

2.2.1 Active Materials

For a material to be desirable for laser operation, it must possess strong absorption lines, sharp fluorescent lines, and a reasonably high quantum efficiency for the fluorescent transition of interest [21]. These characteristics are generally shown by solids (crystals or glass) that incorporate small amounts of elements in which optical transitions can occur between states of inner, incomplete electron shells. This element is called an active material, or active ion. Depending on the type of active ion and the interaction with the surrounding lattice host, the properties of the laser varies.

Host materials

[5]Typical host materials for laser active ions are crystalline solids and glasses. Laser hosts require good optical, mechanical and thermal properties, to withstand the severe operating conditions of practical lasers. Desirable properties include hardness, chemical inertness, absence of internal strain and refractive index variations, resistance to radiation induced colour centers, and ease of fabrication [21]. Several interactions between the host crystal and the active ion restrict the number of useful material combinations. Ideally, the size and valence of the additive ion should match that of the host ion it replaces. Spectroscopic properties like transmission in the operating range is also important.

Crystalline materials: Crystalline laser hosts generally offer high thermal conductivity, narrow fluorescence linewidths and great hardness. Crystalline materials can be used to incorporate ions into specific lattice sites, to preserve their valences. The downside to crystalline materials is that growth of crystals is slow and expensive, and the optical quality and doping homogeneity are often poor.

Ceramics: Polycrystalline ceramics can be produced with good optical quality, and with power outputs and efficiencies comparable to single crystal lasers. Ceramics are easier to produce than single crystals, can be produced in larger quantities and sizes, and with higher doping concentration, than crystalline materials.

Glasses: Glasses are easy to fabricate, also in large quantities and as large structures. The optical quality of the glass can be excellent. Glasses can be used to draw fibers, to create compact and robust fiber lasers. The lack of a well defined crystalline field surrounding the active ions, makes it hard to control the valency of the ions incorporated, resulting in larger fluorescence linewidths than in crystals due to inhomogeneous broadening. This

---

[5]This section is based on reference [21]

increases the laser threshold for glass lasers. Glasses have lower thermal conductivity than crystalline materials, leading to large thermally induced birefringence and optical distortion when operated at high average powers.

Crystalline field

[6]In an ionic crystal, electrons are highly localized and can be associated with a particular ion. However, they also feel the influence of the electrons and nuclei around it. These interactions can be considered as a crystalline field that the electrons are subjected to. The crystalline field is external to the ion, and has a definite symmetry. By knowing the symmetry, one can predict the splitting of the energy levels of the electrons. The crystalline field can be approximated into three different schemes: the weak, medium, and strong field approximation, indicating the strength of the crystal field in comparison to the electrostatic interaction between electrons in an ion.

A modification of the crystal field theory, called the ligand theory, takes into account the overlap between the ion and the ligand orbitals. The distribution of ligands around a central ion determines the amount of overlap, and hence the splitting of the orbitals in the ion. An ion placed in an octahedral site will experience an overall larger crystal field splitting than an ion placed in a tetrahedral site, as the latter only interacts with four ligands, meaning less overlap between the orbitals.

This crystal field splitting mainly happens in the outer electron shells of the ion, as the deeper shells are shielded. Valence electrons located in the outer electron shells will be more affected by the surrounding crystalline field than valence electrons that are shielded by other electron shells. This is the reason why transition-metal ions are more affected by the crystalline field than rare-earth ions, discussed below.

2.2.2   Active Ions

Most solid-state lasers emit radiation based on 4f-4f transitions in rare-earth (RE) ions or 3d-3d transitions in transition-metal (TM) ion doped crystals.

The probabilities of these transitions happening, depend on a set of quantum mechanical selection rules, that allow certain transitions, but completely inhibit others.

The spectroscopic properties of the active ions depend on how they interact with the surrounding lattice, which again depends on the types and positions of the electronic energy levels in the ion.

Energy transitions

When interacting with a photon, an atom or molecule can undergo a transition, moving into an excited electronic, vibrational or rotational state.

Quantum mechanical selectrion rules for the different types of transitions exist, and determine whether a transition is allowed or not [23].

Selection rules for electronic transitions:

- $\Delta S = 0$

---

[6]This section is based on reference [22]

- $\Delta L = 0, \pm 1$ ($L = 0 \leftrightarrow L = 0$ is not allowed)

- $\Delta J = 0, \pm 1$, ($J = 0 \leftrightarrow J = 0$ is not allowed)

- The Laporte selection rule states that the parity of the wavefunction must change upon transition

Selection rules for vibrational transitions:

- $\Delta v = \pm 1, \pm 2, \ldots$ are all allowed for anharmonic potentials, but the intensity of the peaks weakens as Δv increases

- $\Delta v = 1$ is called the fundamental vibration, while larger Δv is called overtones

Selection rules for rotational transitions:

- $\Delta J = \pm 1$

- $\Delta J = 0$ is allowed when an electronic or vibrational transition is present, but then only when there's a net angular momentum in one of the electronic states

The most common types of transitions between energy levels in a laser are vibronic transitions, rotational-vibrational transitions, and pure rotational transitions.

Vibronic transitions are transitions that involve both an electric and a vibrational transition. A photon excites an ion to both an excited electronic and vibrational state. For an ion located at an inversion center, the d-d and f-f transition are parity forbidden by the Laporte rule. But in the presence of thermal vibrations, the corresponding ion-phonon interaction relaxes the selection rule, by periodically positioning the ion outside of the center of symmetry, partially allowing the electric dipole transition [24].

The restrictions on d-d and f-f transitions can also be partially lifted when the ion is placed in a crystal field with no inversion symmetry. While ions placed in octahedral or cubic lattice sites experience a symmetric crystalline field, tetrahedral sites do not contain this inversion symmetry, allowing the electronic transitions to take place [25].

Configurational coordinate diagram

A configurational coordinate diagram shows the potential energy curves of an ion in a crystal lattice, and visualises both the interaction between the ion and the surrounding lattice, and the width of the optical transitions.

The curves are shown as a function of distance of an ion to its neighbours, Q. This curve can be approximated by a parabola near the equilibrium position Q_0.

As the electrons in the excited state orbital are more loosely bound to the ion than the electrons in the ground state, the excited state potential energy curve has less curvature [25]. The spatial distribution of the excited state orbitals can be different to that of the ground state, resulting in a different equilibrium position Q_0' of the excited state parabola. Interactions with orbitals of nearby ions shift the equilibrium position.

According to the Franck-Condon principle, optical transitions in the configurational coordinate diagram are vertical. An electron excited from state A in Figure 5 reaches state B in the excited state. The electron loses energy by generating lattice vibrations, and relaxes to state C, before emission of a photon leaves it in state D. The electron then relaxes back to state A. This explains Stoke's law in a qualitative way, showing why energy absorption is higher than emission in most cases [25].
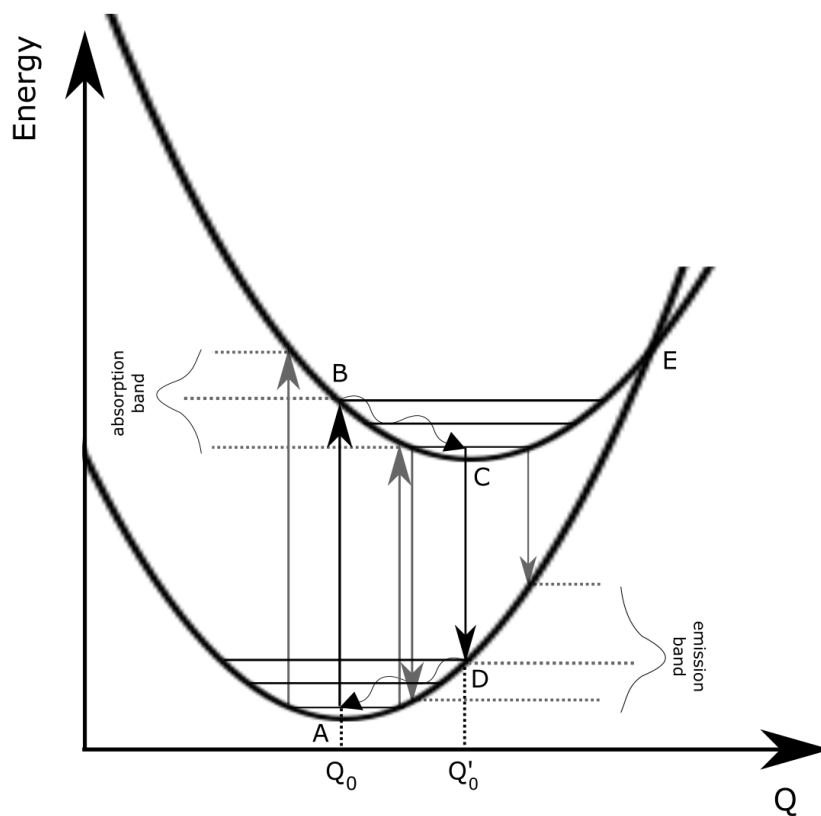
Figure 5: Configurational coordinate diagram, explaining luminescence transitions according to the Franck-Condon principle.

At finite temperature, the electron oscillates around the equilibrium position along the configurational coordinate curve, up to the thermal energy kT. Depending on where the particle is along the parabola at the time of the transition, the energy difference between the two parabolas may be different. This results in broadband absorption and emission spectra. How broadband the emission is, depends on the shift in the equilibrium positions of the ground and excited parabolas. If the two parabolas are exactly above one another $Q_0 = Q'_0$, the energies of all transitions are nearly equal, and the transition is narrowband. If the parabolas are shifted, the transition energy will be lower or higher than for Q_0, resulting in broadband absorption or emission.

When two configurational coordinate curves intersect, an electron in the excited state can cross the intersection in point E in Figure 5, and reach the ground state by non-radiative decay. This decay process is thermally activated, and the decay rate increases with temperature according to the relation

$$\frac{1}{\tau_{nr}} \propto e^{-\frac{E_{act}}{kT}}$$

where E_{act} is the activation required for the process, given as the energy difference between point C and E.

Rare-earth ions

Lanthanide rare-earth ions are commonly used as active ions in solid-state lasers. They are normally incorporated into a material in the trivalent state, after the atom has given up its two outermost 6s electrons and a 4f electron.

The fluorescence spectra of rare-earth ions arise from electronic transitions in the partially filled 4f shell. The 4f states are well shielded from the surrounding crystalline field by the filled 5s and 5p outer shells. These shells are spherically symmetric, and do not affect the 4f electrons. The result is limited interaction between the lanthanide rare-earth ion and the crystal field of the surrounding lattice. Due to the shielding by the outer shell electrons, the crystal field splitting is weak in comparison to the spin orbit coupling and the electrostatic interactions among the 4f electrons, even in the presence of strong local fields from the crystal. The primary change from the free-ion energy levels is due to the Stark effect of the crystal field, which splits the energy levels in many closely spaced levels, referred to as manifolds (Figure 6a).

The energy level structure of rare-earth ions vary only slightly from one host to another, making incorporation of rare-earth ions into a range of host materials possible. As the ion keeps its preferred trivalent state also in a non-crystalline environment, incorporation into glass is possible.

In a configurational coordinate diagram, the low interaction with the surrounding crystalline field means the excited state parabola will not be significantly shifted compared to the ground state parabola, as shown in Figure 7a. This results in narrowband emission from rare-earth ions.

Transition-metal ions

The optical transitions in transition-metal ions occur in the outer, open 3d-shell. These electrons are not shielded from the crystal field in the same way as the valence electrons in rare-earth ions are. For this reason, transition-metal ions are strongly affected by the host material they are incorporated into, and their optical properties vary from host to host.

a) Rare earth ions

b) Transition metal ions
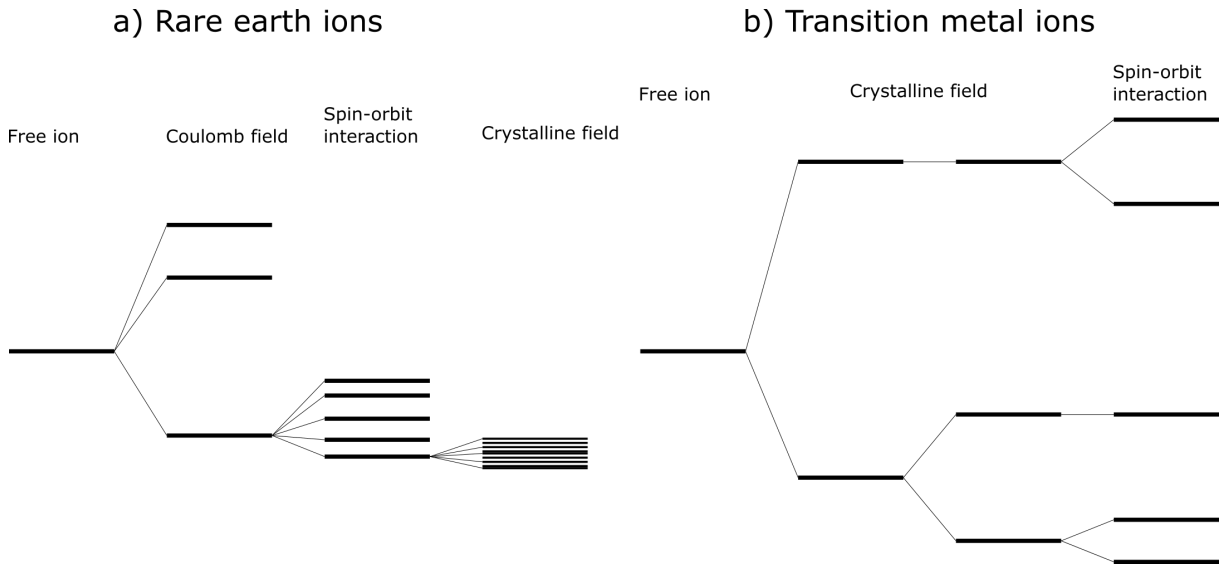
Figure 6: Splitting of energy levels in a) rare earth, and b) transition metal ions subjected to a crystalline field

a) Rare earth ions

b) Transition metal ions
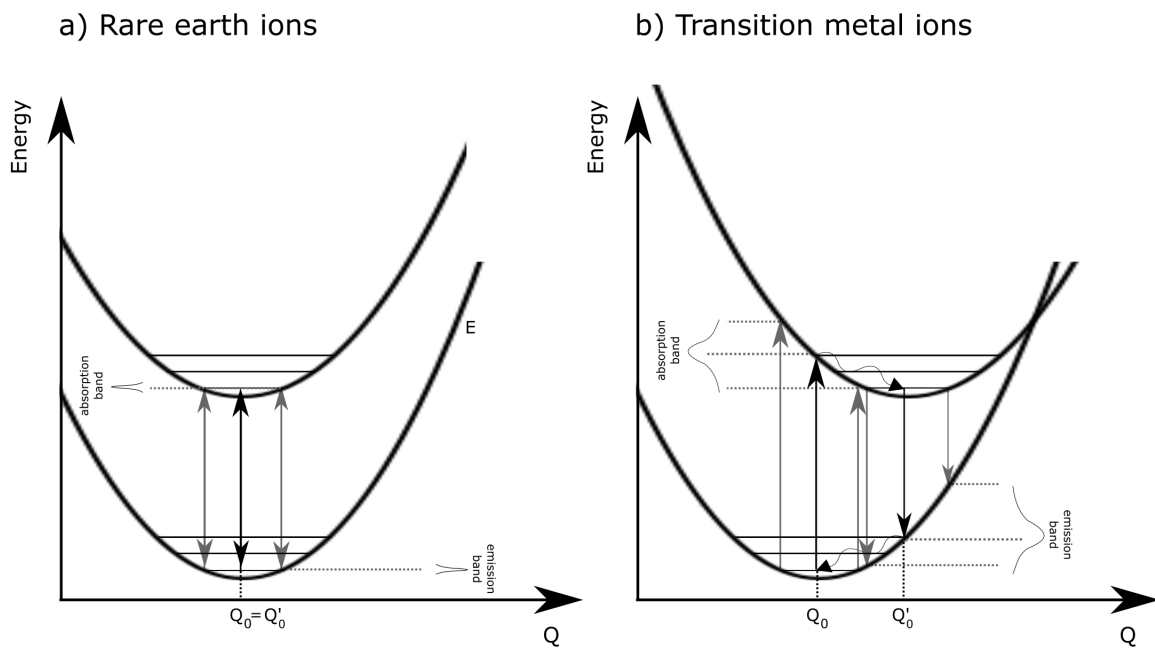
Figure 7: Configurational coordinate diagram of a) rare earth, and b) transition metal ions subjected to a crystalline field

While rare-earth ions are usually incorporated in the trivalent state, transition-metal ions are aliovalent, they can be incorporated into a host material in a range of different valencies. Which valency the ion is incorporated with, depends on the coordination of the lattice site of incorporation. For this reason, a challenge with transition-metal ions is incorporation into only one specific lattice site in a crystal, giving ions with one valency.

The crystal field potential in transition-metal ions is comparable to or larger than the electrostatic interactions, and larger than the spin-orbit coupling. The crystal field splitting is large in comparison with the separation of the different spectral terms, illustrated in Figure 6b [22].

Due to the very strong interactions with the surrounding crystalline field, the electronic states of the transition metal ion undergo a strong perturbation, and are to a large extent defined by the surrounding material. In a configurational coordinate diagram, the excited state parabola is strongly shifted, giving broadband emission (Figure 7b). This makes transition metal ions tunable, and suitable for extremely short pulse generation.

Broadening and losses in ion doped materials

[7]The bandwidth of a laser states its ability to absorb and emit light over a range of wavelengths. It determines the laser's ability to be tuned, and to produce short pulses.

Due to the inverse relationship between wavelength and frequency, the bandwidth scales with central wavelength, by

$$\Delta\nu = \frac{c}{\lambda^2}\Delta\lambda$$

This shows that e.g. 1 nm is worth more gigahertz at shorter wavelengths than at longer. To be able to compare bandwidths across wavelength regions, the relative bandwidth $\Delta\lambda/\lambda$ is used.

As seen in Equation (5), the threshold power intensity increases with increased relative bandwidth, meaning that the toll paid for broad bandwidth, is the increase in threshold [26]. The factor λ^4 in the denominator decreases the threshold for longer wavelengths, lowering the threshold for transitions in the mid-IR. This means that in the mid-IR, materials with broader bandwidths can be realized, without obtaining an unrealistically high threshold.

Broadband gain in ion-doped laser materials are determined by the particular ion-lattice interactions, homogeneous and inhomogeneous broadening, and overlapping of spectral lines.

In rare-earth ions the linewidths of the individual transitions between the Stark sublevels is not very broad, as already discussed. Typically they are of the order of $1\,\mathrm{cm^{-1}}$. Broadband gain can still be obtained by inhomogeneous broadening in disordered crystals, glasses and fibres. Inhomogeneous broadening makes it possible to achieve bandwidths up to $100-3000\,\mathrm{cm^{-1}}$. Certain rare earth ions, like Tm^{3+} and Ho^{3+}, possess under crystal field splitting many closely spaced Stark sublevels, giving stronly overlapping transition bands making continuous tuning over $100-200\,\mathrm{nm}$ possible around $2\,\mathrm{\mu m}$.

In transition-metal ions in a crystalline environment, the shifted equilibrium of the excited energy parabola in the configurational coordinate diagram provides larger bandwidths than anything obtained in rare-earth ions, reaching thousands of $\mathrm{cm^{-1}}$. Compared to this effect, inhomogeneous broadening is insignificant.

While a large shift of the parabolas leads to a broader gain bandwidth, it also increases the probability of non-radiative decay. As the two parabolas overlap (point E in Figure 5), excited

---

[7]This section is based on reference [26]

energy can escape by non-radiative decay, and the energy of this overlapping will lower as the perturbation increases. This sets a limit to the maximum bandwidth obtainable, given by

$$\frac{\Delta\nu}{\nu_0} \leq 2.3\sqrt{\frac{kT}{h\nu_0}}$$

where $h\nu_0 = E_0$ is the energy distance between the electronic levels. The equation predicts that the maximum relative bandwidth obtainable for the vibronic transitions scales with wavelength as $\lambda^{1/2}$, something that has been observed experimentally [27].

Generally, there are two main mechanisms for non-radiative decay in transition-metal ion doped lasers. Thermally activated non-radiative decay, as already described, is bandwidth dependent. Direct multiphonon processes happen when $p = \Delta E/h\omega$ phonons of energy ω is generated, bridging the energy gap ΔE. As p increases, the probability of the process happening decreases. This process does not depend on the bandwidth, but depends on the maximum phonon frequency of the lattice, as low-phonon materials will need a high p. It sets a limit for continuous-wave laser operation at longer wavelengths, and room temperature lasers beyond 3 µm is very uncommon.

2.2.3 Fiber Lasers vs. Crystalline Lasers

Fiber lasers

Active glass optical fibers are currently one of the most efficient solid-state laser media, with excellent beam quality. An all-fiber construction using Bragg gratings to form a laser cavity provides small size and weight, along with user-friendliness and reliability. Because of the large surface area to volume ratio of the fiber, efficient cooling is achieved.

For reasons already discussed, incorporation of transition-metal ions in fiber lasers is challenging, as the amorphous structure of the glass material leads to a range of possible sites for ion incorporation, making it hard to preserve the valency of the transition-metal ion.

For this reason fiber lasers commonly incorporate rare-earth ions in their preferred trivalent state. This means that fiber lasers are mainly narrowband and not tunable. As seen, some inhomogeneous broadening happens, especially in glass matrices, but not nearly to the extent as can be achieved with transition-metal ions.

Crystalline lasers

Crystalline lasers incorporate both rare-earth and transition-metal ions. As the properties of rare-earth ions do not change significantly from host to host, the same properties can be achieved in a rare-earth ion doped crystalline and fiber laser.

The advantage lies in the possibility to incorporate transition-metal ions into the crystalline matrix, yielding a broadband emission which can be used to make a broadly tunable or ultrashort pulsed laser.

Extremely high power can be achieved using crystalline lasers. But they are still rather expensive and difficult to operate, making them hardly accessible outside of a laboratory.

Combining the tunable and ultrashort pulse generating abilities of a transition-metal ion doped crystalline laser, with the ease of fabrication and use of a fiber laser, would yield a versatile glass-ceramic fiber laser suitable for a range of applications.

2.3   Selected Laser Materials

This section summarises the desirable physical properties of the laser materials used in this work.

2.3.1   Phosphate Glasses

Due to their low melting and glass transition temperatures, a wide transmission range from UV to NIR, high thermal expansion and optical characteristics, and easy fabrication, phosphate glasses have been the subject of many investigations over the years [28], and have been used to create fiber lasers.

Vitreous phosphate glasses consists of a random chain of phosphate tetrahedra. The tetrahedra are classified using Q^i terminology, where i represents the number of bridging oxygens per tetrahedron [29]. Pure phosphate glass contains only Q^3 tetrahedra, while metaphosphate glass, created from e.g. $NaPO_3$, contains only Q^2 tetrahedra.

Alkali, alkaline earth and some transition metal oxides can be melted with phosphates, to create glasses with better durability and new properties. The properties of these glasses have been shown to depend more on the interchain crosslinking with the metal ions, than on the internal phosphate chain bonds.

Oxides like ZnO works as depolymerizing agents, shortening the lengths of the phosphate chains by breaking the bonds between the middle chain groups. In a metaphosphate glass with groups of Q^2 coordination, Q^1 groups are created. ZnO is shown to bond exclusively to chain end groups of the Q^1 coordination [30].

Increasing ZnO contents leads to a decrease in Q^2 groups and an increase in Q^1 groups. It is possible to calculate the amount of Q^2 and Q^1 sites by using the formulas [28]

$$C(Q^2) = 100(2 - R) \tag{8}$$

$$C(Q^1) = 100(1 - C(Q^2)) \tag{9}$$

where $R = ([ZnO] + [Na_2O])/[P_2O_5]$, and $[ZnO]$, $[Na_2O]$ and $[P_2O_5]$ are the concentrations in molpercent. This can again be used to calculate the average chain length, L_{CH}, defined as the number of P atoms in the chain.

$$1/L_{CH} = (R - 1)/2$$

Phosphate glasses demonstrate a higher solubility of II-VI semiconductor nanocrystals, compared to silicate glasses [31], making them suitable materials for incorporation of such crystals. Their fabrication is simpler than for chalcogenides. Glasses doped with semiconductor nanocrystals are shown to demonstrate both glassy and semiconductor behaviour [32]. Features that are specific for semiconductor crystals, like a sharp edge of optical absorption, has been shown in these glasses.

2.3.2   II-VI Semiconductors

II-VI semiconductors are attactive as crystalline hosts for mid-IR laser applications, for many reasons.

II-VI compounds have a tendency to crystallize as tetrahedrally coordinated structures. As already discussed, active ions placed in tetrahedral coordination experience a smaller crystal

field splitting than ions placed in octahedral coordination, placing the transition in the mid-IR range [33]. The lack of symmetry in tetrahedral sites also lifts the Laporte selection rule, allowing d-d and f-f transitions, increasing the absorption and emission cross-sections of the materials.

Strong electron-phonon interaction of transition-metal ions in II-VI semiconductors results in significant broadening, making such materials promising for ultrabroadband mid-IR tunability and ultrashort pulse generation [34].

II-VI compounds often consists of heavy anions, only supporting the lowest phonon modes ($850\,\mathrm{cm}^{-1}$ in YAG vs $250\,\mathrm{cm}^{-1}$ in ZnSe [35]). The very low optical phonon cut-off makes them transparent in a wide spectral region, and decreases the non-radiative decay rate, beneficial for achieving a high fluorescence quantum efficiency at room temperature [36]. This is a very important material property, as the non-radiative decay sets the fundamental limit for laser operation at long wavelengths, as discussed in Section 2.2.2.

Cr:ZnSe

ZnSe is a type II-VI semiconductor with a zinc-blende crystal structure with partially ionic bonds. This means that all the active ions incorporated into the crystal are located at a tetrahedral site, ideal for laser applications.

Chromium exhibit unique spectroscopic characteristics when placed in a II-VI semiconductor. The atom enter the ZnSe lattice mainly as Cr^{2+}, substituting for the Zn atoms, placing the Cr^{2+} in a tetrahedral coordination. This leads to energy levels in the band gap of ZnSe. The ground term (^5D) of the Cr^{2+} ion is split into a triplet $^5T_2$, and a higher energy doublet ^5E. According to the Laporte selection rule, electric-dipole transitions between d-states are parity forbidden, but the absense of inversion symmetry lifts this restrictions, as discussed in Section 2.2.2. The restriction is also weakened due to phonon coupling, where vibrations can create a mixing of d and p orbitals. This means that transitions between the energy levels are symmetry allowed, while transitions to all other upper levels are forbidden [33].

The last point is important, as it means excited state absorption (ESA) is not a problem in Cr:ZnSe [37]. ESA is a two-step excitation process, where an already excited ion is excited into an even higher-lying excited state, either by the pump or laser radiation. The ESA often overlaps with the emission spectrum of transition metal ions, sometimes completely inhibiting the laser operation [26]. It is often referred to as the "laser material killer", as ESA at laser wavelength renders many promising broadband materials with otherwise excellent parameters unusable. A vibronic material completely without this problem, is very rare.

Spectroscopic investigations of Cr:ZnSe in the visible/near-IR region show two absorption bands [38]. The broad band around 1500-2000nm is the intra-center absorption $^5T_2-^5E$, and shows Cr:ZnSe as a promising candidate for laser action in this region. A strong and broad absorption band is observed around $500\,\mathrm{nm}$, corresponding to the charge transfer process $Cr^{2+} \rightarrow Cr^+ + h\nu_{VB}$.

The Cr:ZnSe laser can be pumped both into the absorption band around $1.8\,\mathrm{\mu m}$, and at $500\,\mathrm{nm}$ [39]. The large Stokes loss when pumping into the band around $500\,\mathrm{nm}$ limits the total laser efficiency. For this reason, direct excitation into the $1.8\,\mathrm{\mu m}$ band is advantageous, as lasers operating in this regime has become more and more available.

The emission spectra of Cr:ZnSe shows a large emission band centered around $2200\,\mathrm{nm}$. This emission is attributed to the intra-centre transition of Cr^{2+} between the first excited state, ^5E, and the ground state $^5T_2$. The transition can happen by the following processes, illustrated in Figure 8 [33]:

a) Pumping with an excitation energy slightly larger than the band-gap of Cr^{2+}:ZnSe puts an electron in the conduction band by releasing a hole in the valence band. This excitation is captured by the Cr^{2+} ion in the ground state, to obtain the Cr^{2+*} excited state. The excited state relaxes to the ^5E excited energy level by non-radiative decay processes, before emission of a mid-IR photon leaves the Cr^{2+} back in the ground state (Figure 8a).

b) Pumping with an excitation energy larger than the band-gap of Cr^{2+}:ZnSe, the Cr^{2+} ion is ionised to the Cr^+ state by receiving the excited electron. Recombination with the hole in the valence band gives rise to the excited state Cr^{2+*}, which relaxes to the ^5E excited energy level, and emission is obtained (Figure 8b).

c) Pumping with excitation energy lower than the band-gap of Cr^{2+}:ZnSe is done by an incident photon ionising the Cr^{2+} ion to the Cr^+ state by releasing a hole to the valence band. A second pump photon ionises the Cr^+ ion to the excited state Cr^{2+*}, by raising an electron to the conduction band. Emission is obtained as in the previous mechanisms (Figure 8c).
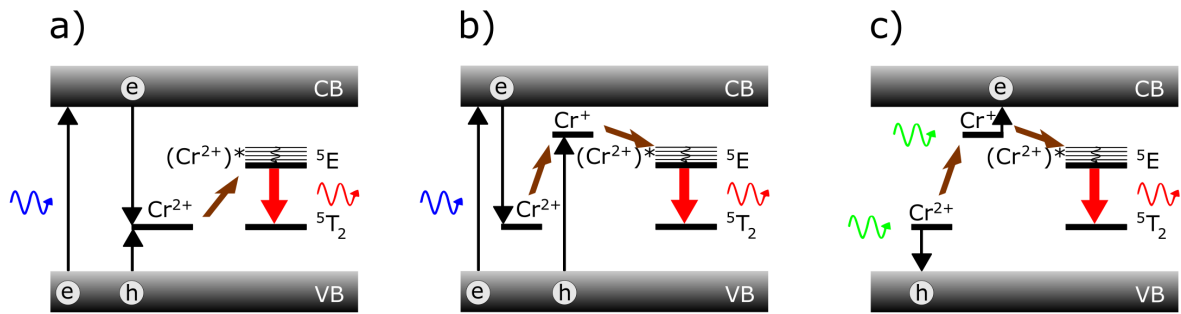
Figure 8: Transitions between energy levels of Cr^{2+} in ZnSe

The intra-centre transition shows a radiative lifetime of about 7.3 µs, and a build up time of about 1.8 µs, sufficient for laser action [38]. The lifetime does not show a significant temperature dependence up to 300K.

The most commonly used fabrication methods for doping ZnSe with Cr are thermal diffusion, physical vapour transport, Bridgeman method, and hot-pressed ceramic [36]. To provide the desired characteristics, a doping concentration of about $10^{18} - 10^{19} cm^{-1}$ is needed. Below this concentration, there is not sufficient absorption in Cr^{2+} ions to provide stimulated emission. Above this concentration, the photoluminescence lifetime is too short for laser operation [38]. This decrease is thought to happen due to concentration quenching, where excitation energy is transferred between neighbouring Cr^{2+} ions by non-radiative transitions, until it reaches a quenching state, e.g. a defect. Another explanation is that Cr is not only incorporated in the optically active Cr^{2+} state, but also in the Cr^{3+}, Cr^+ and metallic Cr form, killing the luminescence and reducing the corresponding fluorescence lifetime [33].

Cr:ZnSe possesses many favourable characteristics, like a high emission cross section σ_{em} (on the order of $10^{-18} cm^2$) and short radiative lifetime τ_r [40]. The high activation energy E_{act} in Cr:ZnSe crystals leads to a decreased non-radiative decay rate and a high fluorescence quantum efficiency [36]. High chemical and mechanical stability, along with good thermal conductivity, is another advantage of the material.

2.3.3   Saturable Absorbers

Semiconductor saturable absorber mirrors (SESAMs) are currently the most commerically available saturable absorber, as the well-developed semiconductor industry are able to create these

components with good control over the parameters. These saturable absorbers are yet rather expensive and bulky, and have a drawback of operating only over a limited wavelength range ($<\sim 100\,$nm), set by the resontor behaviour of the semiconductor quantum well structure and the bandwidth of the high-reflector coating [19, 41].

Mode-locking using single-wall carbon nanotube saturable absorbers have been demonstrated in the wavelength region $800 - 2070\,$nm [42, 43]. Limits in the diameter of the currently producible SWCNTs, and other fabrication issues, has been a restriction to the transition wavelengths of such saturable absorbers [44].

For this reason, graphene saturable absorber mirrors have emerged as a promising alternative.

Graphene saturable absorber mirrors

The unique optical and electronic properties and the high thermal conductivity of graphene, makes it promising as a saturable absorber.

The electronic structure of graphene can be described as a Fermi cone, with a linear dispersion relation near the Fermi energy. This makes the optical transitions independent of frequency for a broad range of photon energies, making them suitable for broadband operation, overcoming the limitations of SESAMs and SWCNT saturable absorbers.

After excitation of electrons at a certain wavelength into the conduction band, high energy electrons cool down, gradually filling the lower states in the conduction band. The edges of the conduction and valence band fills until the states near the edge of the conduction and valence band are full, blocking further absorption. At this point, the material becomes transparent to all photons of energy up to just above the band-edge.

Graphene saturable absorbers have low saturation intensity and ultrafast response times of a few hundred femtoseconds, making them suitable for ultrafast pulse generation. The modulation depth, describing how much the light signal amplitude is varied around its unmodulated value, is significantly lower to that of SESAMs, and comparable to that of SWCNT saturable absorbers [19]. Single-layer graphene typically has a modulation depth around 1% [45], which in many cases is too low. By stacking graphene layers, the modulation depth can be improved, but at the cost of an increased saturation intensity.

To achieve stable mode-locking, the graphene should cover the entire laser beam spot area. This spot is limited by diffraction to a few tens of micrometers. Large areas covered in graphene can be made by overlapping of small graphene sheets. However, overlapping sheets makes it difficult to control the uniformity, and therefore the insertion loss and thermal durability, of the graphene saturable absorber [46].

2.4   Literature Overview

2.4.1   Fiber Lasers with Active Ions

Current literature on ion doped fiber lasers, centres around rare-earth ion doped fibers.

The first demonstration of a glass fiber laser was done in 1964 [47], and interest sky-rocketed after Payne et al. created rare-earth ion doped low-loss fibers in 1985 [48]. Since that time, the performance of fiber lasers have steadily increased, and fiber lasers emitting in a range of wavelengths between the UV and mid-IR have been created [49, 50], along with fiber lasers of CW output power as high as 100 kW [51].

As most of the fiber laser advances centers around rare-earth doped fibers, a lot of research has centered around single-frequency lasers with sub-kilohertz linewidth [52].

Due to the broadened gain bandwidth of rare-earth ions incorporated into glass compared to crystalline hosts, mode-locked glass fiber lasers have been fabricated. Sell et al. produced an 8 fs mode-locked laser using an Er^{3+} doped fiber system [53], and several other femtosecond fiber laser systems with short pulses have been fabricated [54, 55]. These are not all-fiber lasers, but rather a system of optics where the fiber laser works as the active medium.

Bi doped fiber lasers

The first successful transition metal ion doped fiber laser was fabricated in 2005, and incorporated bismuth ions into an aluminosilicate glass matrix [56]. Depending on glass composition and excitation wavelength, IR luminescence is observed in the spectral region $1000 - 1600$ nm [57]. Out of this, a range of Bi fiber lasers has been developed in the spectral region $1150 - 1215$ nm.

Mode-locking has been achieved, generating 50 ps laser pulses [58].

These fiber lasers have seen challenges in preserving the valency of the incorporated Bi ions, as energy level diagrams of several valencies of Bi ions are needed to explain the observed absorption and emission bands [3]. Varying performance and problems with ESA in Bi fiber lasers has also been reported [4].

Cr^{4+} doped chalcogenide glasses

E.J. Aronson demonstrated incorporation of Cr^{4+} in a range of different chalcogenide glasses [59]. The glasses showed broad near-IR emission in the very interesting wavelength range $1050 - 1200$ nm. However, the low concentration of active ions and the low quantum efficiency of the material made them not particularly useful as laser materials.

2.4.2 Lasing in Crystalline Nanoparticles

The feasibility of making fiber lasers based on transition metal ion doped nanoparticles, has been demonstrated in articles showing lasing in such nanoparticles.

Lasing in powders can be achieved without a laser cavity. Instead, stimulated emission and multiple scattering inside a highly disordered material, like powders and porous glasses, provides optical gain [60]. In this way the material works as both an active and scattering medium. The emission properties of such lasers, called random lasers, depend only on the active medium, and not on the resonator configuration. Interference in the multiple-scattering process determines the mode structure of the random laser.

The first demonstration of lasing in powders was done in powdered $Na_5La_{1-x}Nd_x(MoO_4)_4$ in 1986 [61]. Later, gain was demonstrated in II-VI compound nanoparticles, namely in close packed strctures of undoped CdSe nanoparticles [62].

Lasing has been demonstrated in Cr:ZnSe powders [63, 64]. Different grain sizes, ranging from nanometers to micrometers, were investigated, with the lowest threshold found in the sample with the largest grain size.

It has been shown that delivering the pump energy deep inside the powder instead of at the surface, reduces the threshold and increases the slope efficiency[8] of the stimulated emission [65].

---

[8]Slope efficiency $\eta_s = dP_{out}^{laser}/dP^{pump}$, the slope of a plot of the laser output power vs. the input pump power

As a larger portion of the pump energy creates scattering in the material, the efficiency increases.

2.4.3   Crystalline Nanoparticles in Glass Matrices

Introducing nanocrystalline powders into glass matrices as a way of creating a new class of nanophotonic solid state laser, was suggested by I. Sorokina [35].

Incorporation of Cr:ZnSe and Cr:ZnS nanoparticles into chalcogenide As_2S_3 glasses were attempted by Mironov et.al [66]. Luminescence of the materials were obtained, but losses in the semiconductor doped glasses were about three times the losses in the pure glasses.

Similar investigations were done by Martyshkin et.al, incorporating Cr:ZnSe and Cr:ZnS micro- and nanocrystals into As_2S_3:As_2S_3 [67]. They were able to show random lasing in the semiconductor doped chalcogenide glasses.

In general, phosphate glasses exhibit a better solubility of semiconductor nanocrystals than silicate glasses. The low volatility of chalcogenide glasses limits the amount of nanocrystals that can be incorporated. For that reason, phosphate glasses has been proposed as a host for micro- and nanocrystalline semiconductors. About 1 wt% CdS and CdSe has been dissolved in phosphate glass, used for fiber-optic temperature sensing [31]. This is higher than the ~ 0.1 wt% dissolvable in silicate glasses.

2.4.4   Crystalline Cr:ZnSe Lasers

The first demonstration of lasing in Cr:ZnSe was made by Page et al. [40]. Since that time, the performance of the material has greatly improved, and Cr:ZnSe has been used to fabricate both CW and pulsed lasers.

Continuous wave lasers with slope efficiency of 63% and tunability between 2138-2760 nm have been demonstrated [68]. The limiting factor for the bandwidth is the optics used in the set-up. With two different sets of optics, a tuning range from 2.0 to 3.1 µm has been demonstrated [68].

The broad emission bandwidth indicates that Cr:ZnSe lasers are suitable for ultrashort pulse generation, and indeed, femtosecond pulses have been obtained in Cr:ZnSe lasers. Mode-locked laser pulses as short as 41 fs have been demonstrated [5], along with several lasers with $\sim$100 fs pulses [69, 70].

2.4.5   Graphene Saturable Absorbers

The first demonstration of graphene as a saturable absorber happened in 2009 [71]. Thorough investigations of the SA kinetics of graphene revealed them to be promising for low-noise laser pulse generation [72]. When implemented into the laser, the graphene exhibited extremely large normal dispersion compared to SWCNTs or SESAMs, but also a low saturation intensity and low non-saturable losses.

Graphene SAs have been used to produce pulses from 0.8 µm [45] to 2.9 µm [73], showing that broadband operation is possible. The modulation depth of the graphene SAs are generally low, but shown to be controllable by varying the number of graphene layers [72, 74]. Increasing the amount of layers increases the modulation depth, but at the cost of an increase in saturation intensity.

The modulation depth also show some trend of decreasing with wavelength (1.8% at 800 nm and 0.4% at 1500 nm [75]), the same with the saturation energy fluence ($66\mu\,J/cm^{-2}$ at 800 nm [45], compared with $14\mu\,J/cm^{-2}$ at 1500 nm [75]). This wavelength dependence of the saturation energy fluence generally favours the use of graphene SAs in the mid-infrared region [19].

Graphene saturable absorbers have been fabricated both using bath sonicating of graphite [46], and by transfer of CVD grown graphene [74].

Graphene has been used to successfully mode-lock crystalline Cr:ZnSe lasers [44], obtaining pulses as short as 41 fs [5]. Fiber lasers mode-locked using graphene saturable absorbers have also been demonstrated, Er^{3+} doped fiber lasers have demonstrated mode-locked pulses down to 174 fs [76, 77], and wavelength tuning of the pulses generated [78]. This demonstrates that mode-locking of fiber lasers using graphene saturable absorbers is possible. It has yet to be demonstrated on a transition-metal ion doped fiber laser, which is the long term goal of the present research.

3 EXPERIMENTAL METHODS

3.1 Fabrication Methods

3.1.1 Glass Fabrication

Melting

Glasses are commonly fabricated from compound powders, heated into a liquid, then cooled below the glass transition temperature T_G to form the brittle state commonly associated with a glass. During the heating, chemical bonds are destroyed and new ones created, giving a structure of polymer chains with covalent bonds, and cross-links with ionic bonds.

Phosphate glasses composed of the elements PO_3, Na and Zn, are referred to as NZP glasses. NZP glasses of chemical formula $(50-x/2)Na_2O$-x-ZnO-$(50-x/2)P_2O_5$ can be made by the compounds $NaH_2PO_4 \cdot 2H_2O$ and ZnO according to the chemical reaction

$$75NaH_2PO_4 \cdot 2H_2O + 25ZnO \rightarrow 37.5Na_2O - 25ZnO - 37.5P_2O_5 + 225H_2O$$

This process produces surplus water, that needs to be removed from the glass before cooling. This is done by melting the powders gradually, giving the water time to evaporate from the mixture.

Using the compounds $NaPO_3$ and ZnO, the reaction becomes

$$75NaPO_3 + 25ZnO \rightarrow 37.5Na_2O - 25ZnO - 37.5P_2O_5$$

This process does not create water, but while the atmosphere and the powders always contain traces of water, a gradual heating is necessary to yield a good result.

Annealing

After a rapid quenching of the liquid glass to a temperature just below the glass transition temperature T_G, the glass is kept at this temperature for a few hours. This is called annealing, and is done to relieve stresses in the material. At this temperature, the glass is too hard and brittle for large deformations, but soft enough to allow microscopic flow of molecules, relaxing internal stresses.

After annealing, the glass is slowly cooled to room temperature.

Cr:ZnSe incorporation

Micro- and nanocrystal of ZnSe doped with Cr^{2+}, can be incorporated into the phosphate glass matrix during the fabrication process. This can be done either by mixing the Cr:ZnSe powder with the compound materials before melting, or by adding Cr:ZnSe powder to either crushed or melted glass before annealing.

Cr:ZnSe dissosiates at 700° C, making it important to keep the fabrication temperature low.

3.1.2 Graphene Transfer

Graphene is easily grown on sheets of Cu foil using Chemical Vapour Deposition. This CVD grown graphene can be transferred to any substrate using a simple transfer technique.

Creating structural integrity

The first step in the transfer process is creating structural integrity. Monolayer graphene has a thickness below 1 nm, leaving it prone to mechanical damage.

A protective polymer, usually polymethyl metacrylate (PMMA) is used to coat the graphene. A thickness of about 500 nm provides mechanical stability while not being too thick to make the removal difficult. PMMA comes with polymer chains of different length (molecular mass). Longer polymer chains provides more structural integrity, but is harder to remove than shorter chains [79]. The amount of solids dissolved in the solvent affects both the thickness of the resulting PMMA layer, and its ease of removal. A PMMA type with short polymer chains, but a large enough amount of solids to ensure sufficient thickness, is beneficial.

When soft baking the PMMA after spin coating, keeping the temperature below the glass transition temperature $T_G = 105°$ C, makes for an easier removal [80]. This is not optimal when PMMA used as an e-beam resist, but for the purpose of structural integrity, it is sufficient.

Copper etching

The second step is removing the Cu foil. Any graphene covering the underside of the Cu foil is removed using oxygen plasma, before a common Cu etchant like ammonium peroxydisulfate (APS, $(NH_4)_2S_2O_8$) is used to remove the Cu.

Transfer

The resulting graphene, protected by PMMA, is transferred to a suitable substrate.

Graphene adheres to the substrate only by weak Van der Waals forces. To increase the adhesion, the distance between the graphene and the substrate has to be reduced to a minimum. This is done first by drying the substrate in air, then by a soft baking on a hotplate.

Acetone removes PMMA by being absorbed into the PMMA structure, expanding the structure and breaking it apart. This process might disrupt the underlying graphene. For a gentle removal of PMMA, submerging the sample in isopropanol and gradually adding acetone, prevents the PMMA structure from expanding too quickly and distorting the graphene.

3.2 Characterisation Methods

3.2.1 Absorption Spectroscopy

Absorption spectroscopy is a spectroscopic technique that measure the absorption of radiation of a sample at different wavelengths.

Absorption spectroscopy is used as an analytical tool to determine the presence of particular materials, and can also be used to quantify the amount of this material. The absorption spectrum depends on the atomic or molecular composition of the material, as radiation is absorbed at wavelengths corresponding to the energy difference between two quantum mechanical states of the molecules.

The most common way of measuring the absorption is by transmitting radiation through the sample, and detecting the transmission. The absorption coefficient can be calculated from the transmission using Lambart Beer's law [81]

$$\alpha = \frac{1}{l} \ln(T) \tag{10}$$

where l is the thickness of the sample, and T is the transmittance, given by $T = \frac{I}{I_0}$, the transmitted flux of radiation divided by the incident flux of radiation. The absorption coefficient can again be used to calculate the active ion concentration in the material,

$$\alpha = N\sigma_{abs}$$

where N is the ion concentration and σ_{abs} is the absorption cross section between two energy levels in an ion, given in cm^{-1}.

3.2.2   Fluorescence Spectroscopy

Fluorescence spectroscopy is a spectroscopic technique that measures the emission of radiation of a sample at different wavelengths.

As each material emits at different wavelengths according to its electronic structure, fluorescence spectroscopy can be used as an analytical tool to determine the presence of particular materials, and to quantify its amount.

Fluorescence spectroscopy is one of the most important characterisation methods for laser materials, as the fluorescence spectrum, along with the radiative lifetime of the material, allows calculation of the emission cross-section using the Füchtbauer-Ladenburg relation given in Equation 2.

3.2.3   Cut-Back Loss Measurements

Losses in a fiber or glass can be measured using a cut-back method. This method got its name from originally being used with fibers, where the transmission through a fiber was measured, before it was cut into a shorter length and measured again [82].

In an equivalent fashion, the transmitted optical power through a glass slab is measured for two different thicknesses L_1 and L_2 of the glass sample. The transmission is detected using a standard powermeter.

The transmission loss $\alpha(\lambda)$ at wavelength λ is expressed as

$$\alpha(\lambda) = \frac{10}{L_1 - L_2} log_{10} \frac{I_2(\lambda)}{I_1(\lambda)} \tag{11}$$

where I_1 and I_2 are the optical powers received after transmission through the sample of length L_1 and L_2 respectively.

3.2.4   Differential Scanning Calorimetry

Differential scanning calorimetry (DSC) is a thermoanalytical technique that measures the amount of heat required to increase the temperature of a sample, as a function of temperature [83]. To quantify this amount of heat, a reference sample with known heat capacity is used. The sample and the reference is kept at nearly the same temperature throughout the measurement.

When a sample undergoes a phase transition, more or less heat will be required to increase the temperature of the sample, as phase transitions usually are endothermic or exothermic. The same is true for physical changes like glass transitions, that changes the heat capacity of the material. By observing the difference in heat flow between sample and reference, DSC measures the amount of heat absorbed or released during the transition.

For this reason, DSC measurements are ideal for determining T_G.

3.2.5   Raman Spectroscopy

Light scattering from materials is mostly inelastic, light scatters with no change in wavelength. This is called Rayleigh scattering. A small amount of the light will scatter inelastically, and exhibit a small shift in wavelength. This is called Raman scattering. Raman spectroscopy is a spectroscopic technique that uses the inelastic Raman scattering, to observe vibrational and rotational modes in materials [84]. For Raman bands to be observed, the molecular vibration must cause a change in polarisability of the material.

A laser is typically used to irradiate the material with monochromatic light. An incident photon raises the molecule from the ground state to an excited "virtual" state. This state rapidly decays, producing a scattered photon. If the molecule goes back into the ground state, the scattered photon has the same wavelength as the incident photon, and we have Rayleigh scattering. If the transition is into a vibrational state of the material, the emitted photon will have a different energy to the incident photon.

If the final vibrational level is of higher energy than the ground state, the scattered photon has lost energy and has a longer wavelength than the incident photon, this gives Stokes Raman scattering. The photon may also gain energy by interacting with a molecule in a higher vibrational level than the ground level, the scattered photon will then have a shorter wavelength than the incident photon. This is called anti-Stokes Raman scattering. The strength of the anti-Stokes spectrum is lower than that of the Stokes spectrum, as it is partly determined by the population of molecules in the higher vibrational level, given by the Boltzmann factor $\exp(-\Delta E/kT)$, where ΔE is the energy of the higher vibrational level.

Raman spectra can be analysed to obtain information about material composition, by identifying the Raman peaks. Comparison of Stokes/anti-Stokes ratio gives temperature information. Stress states shift the Raman peak positions, as does temperature to a smaller extent. Crystallinity and crystallographic orientation, defects and relative concentrations are just parts of what can be analysed using Raman spectroscopy [85].

Raman spectroscopy of phosphate glasses

Raman bands in phosphate glasses are typically broad, and originate from stretching of the bonds between phosphate groups and internally in the phosphate groups.

Raman bands in the frequency range $600 - 850 \, \text{cm}^{-1}$ originate from the in-chain stretching of the P-O-P bonds. The band in the frequency range $950 - 1400 \, \text{cm}^{-1}$ are due to out-of-chain P=O stretching. Scattered overlapping bands around $300 \, \text{cm}^{-1}$ and $500 \, \text{cm}^{-1}$ are also observed, due to complex vibrations like skeletal deformation of phosphate chains [86, 87].

The band around $600 - 850 \, \text{cm}^{-1}$ is shifted to larger wavenumbers as the phosphate chain length decreases. This shift is attributed to a change in the P-O-P bond angle, arising when network modifiers break phosphate chains and create cross-linking, resulting in smaller bond angles [87, 88].

The band around $950 - 1400 \, \text{cm}^{-1}$ decreases in intensity as the amount of network modifying metal oxides increases, and is nearly invisible with high metal oxide contents [28, 87]. This is consistent with depolymerization of the three dimensional network from the metal oxides, reducing the amount of P=O bonds.

At the same time, with increasing metal oxide content a peak around $1160 \, \text{cm}^{-1}$ appears, indicating the formation of Q^2 tetrahedra of two bridging and two non-bridging oxygen atoms. The relative amplitude of this peak increases with metal oxide content, and is due to the depolymerization of the phosphate network [88].

Raman spectroscopy of Cr:ZnSe

The Raman spectrum of Cr:ZnSe is different from that of glasses. Due to the highly symmetric crystalline structure, there are only a few narrow but strong vibrational peaks. Since ZnSe is a non-centrosymmetric material, the usual selection rules are lifted, and LO (longitudinal optical) modes can be observed, in addition to the usual TO (transverse optical) modes. In centrosymmetric materials, LO vibrations do not cause a change in polarizability.

The Raman spectrum of ZnSe is identified by the first LO peak at $252 \, \text{cm}^{-1}$, and the TO peak at $206 \, \text{cm}^{-1}$ [89]. Weaker peaks at about 500, 750 and $1000 \, \text{cm}^{-1}$, originating from the higher order LO modes (2LO-4LO), can also be identified [90]. The peak around $150 \, \text{cm}^{-1}$ is the first overtone of the TA phonon (2TA, transverse acoustic). A weak but broad combination mode 2TA+TO around $270 \, \text{cm}^{-1}$ [91] can also be identified in certain samples.

Both intrinsic and Cr-doped ZnSe samples show these peaks. In samples doped with Cr, the LO peak is shifted to lower wavenumbers with higher Cr concentration, while the peak for the TO mode is unaffected [91].

The Raman peaks of the Cr-Se vibrations are located around $200 \, \text{cm}^{-1}$ and $230 \, \text{cm}^{-1}$. The peaks are broad and weak, and hard to identify below a Cr concentration of $1 \times 10^{20} \text{cm}^{-1}$ [91].

Raman spectroscopy of grahene

The Raman spectra of graphene consists of two main peaks. The G peak located around $1580 \, \text{cm}^{-1}$ is an in-plane vibrational mode, while the 2D peak around $2690 \, \text{cm}^{-1}$ is a second order overtone of the in-plane vibration D (around $1350 \, \text{cm}^{-1}$) [92].

For single layer graphene, the 2D peak is sharp and narrow. For multilayer graphene, the forces from the interactions between the layers results in a splitting of the 2D peak into a number of modes, combining to give a wider, shorter peak. Both the 2D peak and the G peak is shifted towards higher wavenumbers in multilayer graphene. Using the ratio of the peak intensities, I_{2D}/I_G, the number of graphene layers can be derived.

Due to crystal symmetries, the D peak is not allowed in defect free graphene. Only if the photon scatters on a defect or an edge boundary, will this peak be visible. There are three disorder peaks in graphene: D ($1350\,\text{cm}^{-1}$), D' ($1620\,\text{cm}^{-1}$) and D+G ($2940\,\text{cm}^{-1}$) [92]. As the amount of disorder in graphene increases, the intensity of these peaks also increases. Using the ratio of peak intensities, I_D/I_G, the level of disorder in the graphene can be determined. As the amount of defects increases, the ratio increase, as a higher defect density creates more scattering from defects. This happens until a point of high defect density, where a more amorphous carbon structure attenuates all Raman peaks, and the ratio decreases.

3.2.6 Autocorrelator Measurements

Optical autocorrelators are used to measure the duration of ultrashort laser pulses with picosecond or femtosecond duration. Regular photodetectors are too slow to measure such short pulses.

In an interferometric autocorrelator, an incoming laser pulse is split into two equal pulses using a beam splitter. The laser pulses are reflected by mirrors back to the beam splitter, and the two pulses arrive collinearly and with the same polarization at a non-linear detector [93]. Figure 9 shows a schematic of an interferometric autocorrelator.
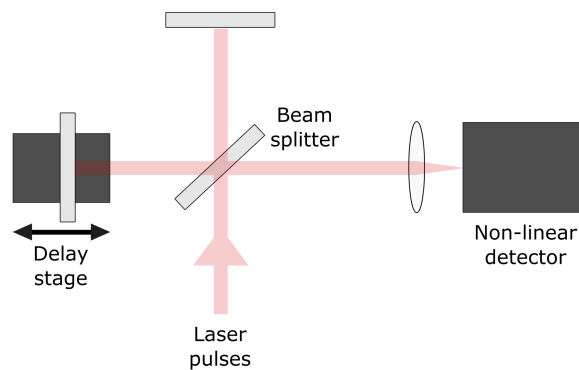
Figure 9: Schematic of an interferometric autocorrelator setup

One of the mirrors are placed on a delay stage, used to vary the optical path of the pulse. With a certain optical path difference, the two pulses will not overlap in the detector.

Detectors based on two-photon absorption processes can be used. These detectors are not sensitive at the pulse wavelength, due to a band-gap larger than the photon energy. The detector needs to absorb two photons arriving simultaneously to bridge the bandgap and register a detection.

Assuming the laser pulse was initially coherent, pulses arriving simultaneously will undergo constructive interference, while half a wavelength difference in optical path leads to destructive interference. This leads to an autocorrelation trace showing fast oscillations with a period equal to the optical wavelength.

Maximum signal is obtained when the two pulses undergo perfect constructive interference, leading to twice the amplitude compared to the single pulse, and an intensity four times that of the original signal. In the detector this yields 16 times the original signal. For perfect destructive interference, the measured intensity is zero. Large arm difference means the two pulses do not overlap and interfere in the non-linear crystal, giving an intensity in the detector of only twice that generated by a single pulse. For this reason, the peak signal is always eight times higher than the background signal in an autocorrelator experiment.

Every peak in the signal corresponds to a difference in optical path equal to an integer value of the wavelength, $\Delta l = m\lambda$. Knowing the wavelength and the speed of light, the time between each peak can be calculated. For laser light at $2.4\,\mu m$, there will be $8\,fs$ between every peak.

Ultrashort pulses from mode-locked lasers often show the sech^2 shape. The pulse duration for such pulses is ~ 0.65 times the width of the autocorrelation signal [94]. The autocorrelation signal width is defined as the full width at half maximum.

4 SAMPLE PREPARATION AND CHARACTERISATION

4.1 Phosphate Glasses Doped with Cr:ZnSe

4.1.1 Fabrication

Phosphate glasses with chemical formula $(50-x/2)Na_2O$-$xZnO$-$(50-x/2)P_2O_5$, x=25, were fabricated using a standard melting technique. Different processes for the incorporation of Cr:ZnSe in the phosphate glass matrix were attempted, with the goal of finding a process that reduced the temperature of the process of incorporating Cr:ZnSe.

(a) Compound powders

(b) Mortar used to finely grind and mix powder

(c) Platina crucible with powder

(d) Furnace to melt powder into glass

(e) Mould for annealing the glass

Figure 10: Images of different steps in the fabrication of phosphate glasses

Standard process

10 g NZP glass were fabricated using these chemicals:

35

- 12.051 g $NaH_2PO_4 \cdot 2H_2O$ (Sigma-Aldrich), above 99% purity

- 2.090 g ZnO (Sigma-Aldrich) above 99 % purity

The chemicals were ground into a fine powder using a mortar and finely mixed, before being transferred to a platinum crucible. The crucible was put into a preheated furnace, and gradually heated using a standard heating scheme (Table 1). The melted glass was transferred to a preheated mould and put in an annealing furnace at 280° C for two hours. Figure 10 shows images from the process.

The mould was cooled to room temperature in air, before the glass was removed.

Table 1: Standard heating scheme

Sample	wt% ZnSe:Cr	Heating scheme
Standard	-	200° C(30mins) - 400° C(30mins) -
		600° C(30mins) - 750° C(60mins)

Series 1: Addition of Cr:ZnSe before melting

0.200 , 0.400 , 0.600 , 0.800 and 1.000 g Cr:ZnSe was added to the powders in the standard process, to create glasses with 2, 4, 6, 8 and 10 wt% Cr:ZnSe, respectively. Pure glass without Cr:ZnSe was fabricated as a reference.

Table 2: Heating scheme for the fabrication of NZP glass with 10, 8, 6, 4, 2 and 0 wt% Cr:ZnSe. The table also shows systematic names given to the samples, for easy referencing.

Sample	wt% ZnSe:Cr	Heating scheme
NZP-25-17	10	Standard
NZP-25-18	8	Standard
NZP-25-19	6	Standard
NZP-25-20	4	Standard
NZP-25-21	2	Standard
NZP-25-31	0	Standard

Series 2: Remelting of pure, crushed glass

In an attempt to lower the melting temperature below 700° C (the dissociation temperature of Cr:ZnSe [95]), pure NZP glass was fabricated using the standard process. The glass was crushed and ground into a fine powder using a mortar, and remelted using the heating scheme shown in Table 3. The powder was checked at regular intervals, and the heating was stopped once melting was achieved.

Table 3: Heating scheme for the pure, crushed glass fabricated using the same process as for NZP-25-31.

Sample	wt% ZnSe:Cr	Heating scheme
NZP-25-22	0	500° C(30mins) - 550° C(30mins) - 600° C (30mins) -
		650° C(30mins) - 690° C(30+90mins)
NZP-25-23	0	690° C(30+30+60+60mins) - 750° C(60mins)

Series 3: Remelting of crushed glass with added Cr:ZnSe powder

It was observed that the addition of Cr:ZnSe decreased the viscosity of the melted glass. In an attempt to reduce the melting temperature, clear glass was fabricated using the standard process, crushed and mixed with Cr:ZnSe powder, before remelting using the heating scheme in Table 4. The heating was stopped once melting was achieved.

Table 4: Heating scheme for pure, crushed glass mixed with Cr:ZnSe powder.

Sample	wt% ZnSe:Cr	Heating scheme
NZP-25-24	10	200° C(30mins) - 400° C(30mins) - 600° C(30mins) - 700° C(60mins) - 750° C(60mins)

Series 4: Addition of Cr:ZnSe powder to melted glass

In order for the Cr:ZnSe not to dissosiate due to long term exposure to temperatures above 700° C, Cr:ZnSe powder was added to melted glass (fabricated using the standard process) 10 minutes before quenching. The crucible was removed from the furnace, powder was added, and the crucible was gently moved about in order to mix the glass and the Cr:ZnSe powder.

Two attempts were made at adding Cr:ZnSe to the melted glass. In one attempt, Cr:ZnSe was added at 750° C, while in the other, Cr:ZnSe was added at 700° C. In both cases, addition of Cr:ZnSe resulted in exhaustion of fumes, and the powder was not evenly mixed in the glass. Table 5 shows the heating scheme of the process.

Table 5: Heating scheme for the fabrication of pure NZP glass. Cr:ZnSe powder was added after melting.

Sample	wt% ZnSe:Cr	Heating scheme
NZP-25-25	10	Standard - add Cr:ZnSe - 750° C(10mins)
NZP-25-26	5	Standard - 700° C(10mins) - add ZnSe:Cr - 750° C(10mins)

Series 5: Pure glass fabricated using NaPO$_3$

NaH$_2$PO$_4 \cdot$2H$_2$O contains water, an impurity in the phosphate glass. The chemical was substituted for NaPO$_3$, in order to reduce the water content even further.

To create 10 g NZP glass with chemical formula $(50-x/2)$Na$_2$O-xZnO-$(50-x/2)$P$_2$O$_5$, x=25, these materials were used:

- 7.876 g NaPO$_3$ (Sigma-Aldrich), above 99% purity

- 2.096 g ZnO (Sigma-Aldrich) above 99 % purity

Two samples were fabricated using the standard heating scheme. Sample NZP-25-28 was crushed to powder and remelted, in an attempt to reduce the melting temperature of the glass, the heating scheme of the powder is shown in Table 6. Sample NZP-25-29 was first heated to 700° C, to investigate if the melting temperature had been reduced when changing compound powders.

Table 6: Heating scheme for the fabrication of NZP glass using NaPO$_3$.

Sample	wt% ZnSe:Cr	Heating scheme
NZP-25-27	0	Standard
NZP-25-28	0	200° C(30mins) - 400° C(30mins) - 600° C(30mins) - 700° C(60+60+60mins) - 750° C(60mins)
NZP-25-29	0	200° C(30mins) - 400° C(30mins) - 600° C(30mins) - 700° C(60mins) - 750° C(60mins)

Cutting and polishing

The glass was cut into discs of about 3 mm thickness by the glass workshop at NTNU, and polished for optical measurements. A Struers RotoPol-21 polishing machine was used at 150 rpm. SiC abrasive paper of granularity (P-grade) P1200, P2500 and P4000 were used for polishing.

4.1.2 Characterisation

Absorption spectroscopy, fluorescence spectroscopy, cut-back loss measurements, differential scanning calorimetry and Raman spectroscopy was performed on several glass samples. Table 7 gives an overview of the samples, and what characterisation methods they were subjected to.

The samples NZP-25-4 and NZP-25-5 are pure NZP glass samples fabricated using the standard process. These samples were borrowed from Radwan Chahal as a reference, before fabrication of NZP-25-31.

Table 7: Overview of the characterisation methods used on NZP samples, showing which samples were subjected to which form of characterisation

Series	Sample	wt% ZnSe:Cr	Abs.	Fluor.	Loss	DSC	Raman
Series 1	NZP-25-17	10	✓	✓		✓	
	NZP-25-18	8	✓	✓		✓	
	NZP-25-19	6	✓	✓		✓	✓
	NZP-25-20	4	✓	✓		✓	
	NZP-25-21	2	✓	✓		✓	
Series 2	NZP-25-22	0				✓	
	NZP-25-23	0				✓	
Series 3	NZP-25-24	10	✓	✓		✓	
Series 4	NZP-25-25	10	✓	✓	✓	✓	
	NZP-25-26	5	✓			✓	
Series 5	NZP-25-27	0	✓	✓		✓	
	NZP-25-28	0					
	NZP-25-29	0				✓	
Pure samples	NZP-25-31	0					
	NZP-25-4	0	✓	✓		✓	
	NZP-25-5	0					✓
Pure Cr:ZnSe	Cr:ZnSe crystal			✓			✓
	Cr:ZnSe pellet			✓			

Absorption spectroscopy

Absorption of the samples at different wavelengths was measured using an OLIS 14F UV/VIS/NIR spectrophotometer, and a Bruker Tensor 27 FT-IR spectrometer.

With the OLIS spectrophotometer, the transmission of the samples were measured in the spectral range $200 - 2600\,\text{nm}$. The number of increments were set to 500, and the reads per increment to 10 A baseline measurement of the empty sample holder was collected, and a verification measurement was run to make sure the background spectra was completely removed. The baseline was renewed every two hours. The spectrophotometer changed detector at $750\,\text{nm}$, and lamp at $340\,\text{nm}$, resulting in a jump in the spectra that had to be corrected.

With the FT-IR spectrometer, transmission spectra were recorded in the spectral range $1500 - 7500\,\text{cm}^{-1}$. A resolution of $10\,\text{cm}^{-1}$ was obtained.

Fluorescence spectroscopy
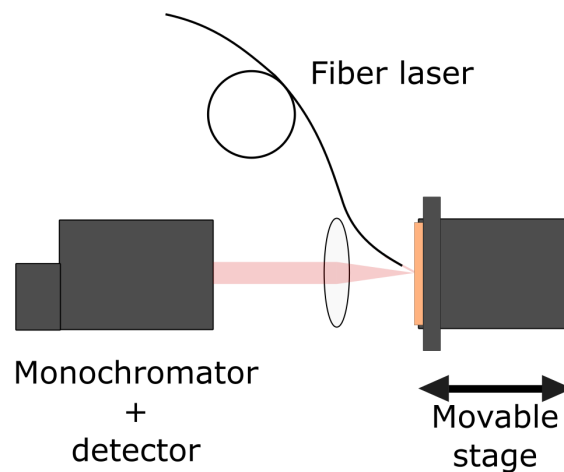
Figure 11: Setup used to measure the fluorescence spectra of the NZP samples

Fluorescence spectra of pure NZP glass, doped NZP glass, along with a piece of pure Cr:ZnSe and a pellet made of Cr:ZnSe powder, was gathered by exciting the samples with a $1.55\,\mu\text{m}$ Er laser with about $100\,\text{mW}$ output power, in a setup shown schematically in Figure 11. The sample was mounted on a movable stage, and laser light was delivered through a fiber, for easy positioning. The sample was adjusted to its optimal position by measuring the reflected fluorescence at $2000\,\text{nm}$. This wavelength was chosen as the photodetector's sensitivity decreases for longer wavelengths.

A SP CM110 1/8 meter monochromator collected the emitted light in the range $1600 - 2600\,\text{nm}$, with a step size of $10\,\text{nm}$. A photodetector attached to the output of the monochromator, received only light at certain wavelengths, measuring the intensity. Consecutive measurements at several wavelengths gave the fluorescence spectra.

Because of a very low emission signal, a lock-in amplifier was used to increase the signal-to-noise ratio. A frequency reference, set by a chopper which modulates the laser light before entering the fiber, was used. Only signal with this frequency reference is accepted, while noise signals at other frequencies are rejected and do not affect the measurement.

Cut-back loss measurements

The losses in a sample of phosphate glass doped with Cr:ZnSe was measured using a cut-back method.

Two samples of NZP-25-25 of thicknesses $L_1 = 2.48$ mm and $L_2 = 0.5$ mm were measured at $\lambda = 2.4$ µm and $\lambda = 2.04$ µm.

The samples were mounted on a stage, and the laser beam was directed through the samples. The transmitted intensity was measured at different points of the samples using a Thorlabs PM100A power meter.

To obtain the losses across the entire sample and not just in certain points, transmission spectra in the wavelength range $1000 - 2400$ nm were obtained using the OLIS spectrophotometer.

Differential scanning calorimetry

A Netzsch DSC 214 Polyma system was used to determine the glass transition temperature, T_G, of the samples. A small crystal of about 10 mg was placed in an aluminium pan with a lid that was sealed in place using a crimping press, and placed in the machine. The temperature was increased from 25 to $450°$ C with a heating rate of $10°$ C per minute. A flow of 40 mL/min N_2 was used to ensure the homogeneity of the temperature in the furnace.

Raman spectroscopy

Raman spectra of pure phosphate glass, phosphate glasses doped with Cr:ZnSe, and a pure Cr:ZnSe crystal were obtained using a Renishaw InVia Raman microscope, with fixed parameters

- Laser wavelength: 532 nm

- Acquisition range: $100 - 1500 \, \text{cm}^{-1}$

- Max laser power: 500 mW CW

- Magnification: 100×

After investigating several laser powers and acquisition times, 50% laser power and 10 s acquisition time were used for all measurements.

The doped NZP sample investigated contained areas with large Cr:ZnSe particles, and areas with lighter and darker red colour without visible particles. Raman spectra were gathered from all these areas.

4.2   Graphene Saturable Absorbers

4.2.1   Fabrication - Graphene Transfer

The aim of the work with graphene transfer, was to transfer graphene from a copper foil to a silver mirror. Before attempting the transfer to the mirror, the process was developed, and several attempts at transfer onto Si dummy wafers were made. After approximately ten practice rounds, graphene was transferred onto the silver mirror.

The steps in the transfer process are shown in Figure 12.
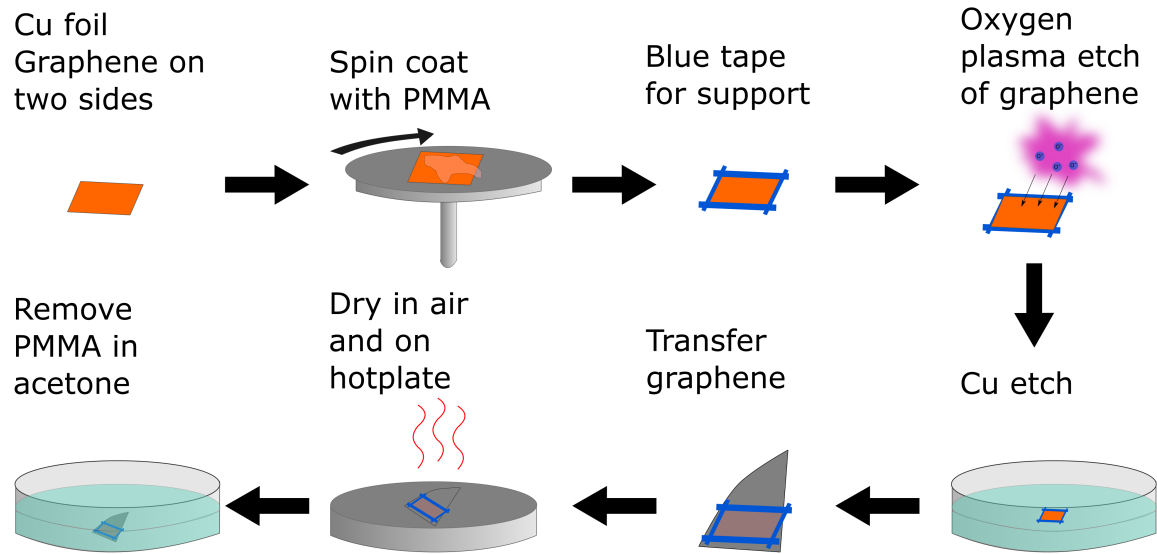
Figure 12: Overview of the steps used in the graphene transfer process

Creating structural integrity

CVD grown graphene on Cu foil was purchased commercially (Graphenea [96]). One side of the Cu foil was spin coated with PMMA, as a protective layer for the graphene underneath. The e-beam resist 200K PMMA A12 was chosen. This type of PMMA has shorter polymer chains (lower molecular mass) than the corresponding 950K PMMA found in the lab, making it easier to remove in the last step of the transfer process [97]. A12 means the polymer is dissolved in anisole, with 12% solids. A high amount of solids is chosen to achieve the desired thickness of the PMMA layer.

PMMA was spin coated at $6000\,\mathrm{rpm}$, with $1000\,\mathrm{rpm/s}$ acceleration, for $120\,\mathrm{s}$. This gives a PMMA thickness of about $500 - 600\,\mathrm{nm}$. The sample was soft baked at $100°\,\mathrm{C}$ for $10\,\mathrm{minutes}$, in order to evaporate the anisole and harden the resist.

Copper etching

Graphene on the back side of the Cu foil (not covered in PMMA), was removed using a Diener Electronics Femto plasma cleaner at 50% power, 50% oxygen flow, and $0.2\,\mathrm{mbar}$ pressure for $12\,\mathrm{seconds}$. Graphene is removed quickly in oxygen plasma, and the time is kept as low as possible to avoid curing the PMMA.

Before etching the Cu, a frame of blue tape was made around the sample. This provided mechanical rigidity to the sample, keeping it from folding over itself. The blue tape floats, keeping the sample floating in the Cu etch bath without turning.

Cu was etched by APS at a concentration of $15\,\mathrm{g}$ APS in $500\,\mathrm{mL}$ water. A magnetic stirrer gently stirred the solution at $100\,\mathrm{rpm}$, and the sample was placed floating on top. The sample was left overnight in the Cu etch, until all Cu was removed.

Transfer

The etched sample was scooped out using a piece of plastic foil, and transferred to DI water in several rounds, to remove residue APS.

Different ways of drying the sample were investigated:

- Drying in air, laying flat

- Drying in air, tilted

- Hotplate, 80° C

- Hotplate, 110° C

- Pressing graphene with N_2 gun

When transferring graphene onto the silver mirror, a process of drying in air at a tilted angle for two hours, followed by one hour on a hotplate at 80° C, was chosen.

PMMA was removed by submerging the sample in isopropanol, and gradually adding acetone until 50% of the solution contained acetone. The sample was moved to a beaker of pure acetone, and left there for two hours.

4.2.2 Characterisation

Raman spectroscopy

Raman spectroscopy of graphene on different substrates were carried out using the fixed parameters

- Laser wavelength: $532\,\mathrm{nm}$

- Acquisition range: $1100 - 3200\,\mathrm{cm}^{-1}$

- Max laser power: $500\,\mathrm{mW}$ CW

- Magnification: $100\times$

To optimise the parameters laser power and acquisition time, multiple Raman spectra were obtained on a CVD grown graphene sample on a SiO_2 substrate. This sample was chosen because SiO_2 has a relatively flat Raman response in investigated area.

The measurements made in this regard are shown in Table 8.

Table 8: Experiments performed to determine the optimal parameters for Raman spectroscopy of graphene

Laser power	Acquisition time
0.1 percent	10 s
0.5 percent	10 s
1 percent	10 s
5 percent	10 s, 20s, 30s
10 percent	10s, 20s, 30s
50 percent	10s

After optimisation, 5% or 10% laser power and $10\,\mathrm{s}$ acquisition time was used in all the Raman spectra of graphene samples.

Raman spectra of graphene transferred onto Si wafers and onto the silver mirror, were obtained. Points, lines and areas were mapped, to investigate the uniformity of the graphene samples.

Mode locking a Cr:ZnS laser

The silver graphene mirror was inserted into the laser cavity of a Cr:ZnS laser operating at $2.4\,\mu m$. To start the mode locking, the cavity was disturbed by moving the graphene mirror. Increasing the intensity of the laser beam was not sufficient for self starting.

Once mode locking was achieved, the input power of the laser was varied in the range $0.4 - 3.6\,W$, to find the threshold of the laser, and the region where mode locking is no longer sustained. The output power was measured for several input powers.

Autocorrelator measurements

Interferometric autocorrelator measurements were performed at $3\,W$ input power, to measure the duration of the mode locked laser pulses.

The raw autocorrelator data were obtained with the units time vs signal (in V). The data was processed to gain a spectrum with time-delay on the x-axis, and a normalized signal on the y-axis. The fringes were filtered out to get only the envelope function of the autocorrelation signal. This envelope function was used to find the pulse duration τ_{pulse}.

5 RESULTS

5.1 Phosphate Glasses Doped With Cr:ZnSe

5.1.1 Glass Fabrication

14 samples of NZP glass were fabricated, the overview is shown in Table 9.

Table 9: Overview of all the fabricated NZP samples

Series	Sample	wt% ZnSe:Cr	Heating scheme
Series 1	NZP-25-17	10	Standard
	NZP-25-18	8	Standard
	NZP-25-19	6	Standard
	NZP-25-20	4	Standard
	NZP-25-21	2	Standard
	NZP-25-31	0	Standard
Series 2	NZP-25-22	0	Table 3
	NZP-25-23	0	Table 3
Series 3	NZP-25-24	10	Table 4
Series 4	NZP-25-25	10	Table 5
	NZP-25-26	5	Table 5
Series 5	NZP-25-27	0	Standard
	NZP-25-28	0	Table 6
	NZP-25-29	0	Table 6

Series 1: Addition of Cr:ZnSe before melting

The glass obtained by this process had a colour gradient, with clear glass on top and darker red glass towards the bottom. Figure 13a shows four cross sections cut from a single sample, and how the colour changes between the samples. The red colour is assumed to originate from Cr^{3+} that has dissociated from the ZnSe, as Cr^{3+} and higher valencies of Cu is known to absorb in the visible part of the spectrum, cutting the green and blue frequencies [98]. The samples also included visible agglomerations of brown ZnSe particles, as shown in Figure 13b.

For all the samples created by this process, the red colour from Cr^{3+} was observed. The platinum crucible also contained some black residue after heating. This residue was absent when fabricating clear glass, indicating that its origin is the Cr:ZnSe. The presence of the residue shows that the Cr:ZnSe undergoes an undesirable chemical reaction during the process.

Series 2: Remelting of pure, crushed glass

The remelting of pure, crushed NZP glass did not result in a reduction of the melting temperature. In the first attempt, the glass powder melted at 690° C after two hours of heating. In the
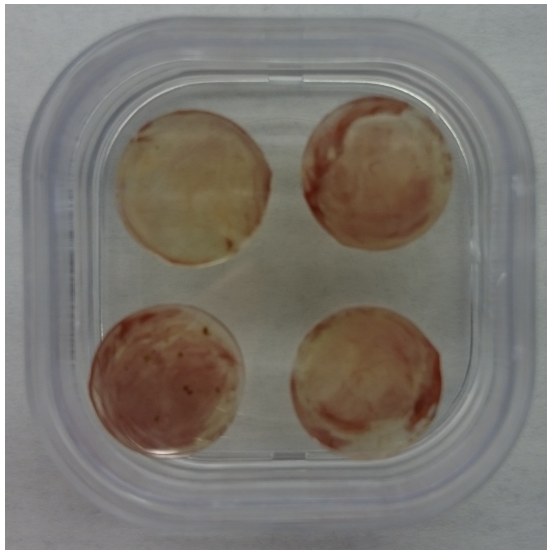
(a) NZP-25-19: Colour gradient of Cr:ZnSe doped NZP glass

(b) NZP-25-18: ZnSe agglomeration in NZP glass

Figure 13

second attempt, the powder melted first at 750° C. In both cases, the glass melt had a higher viscosity than when melting compound powders. Table 10 shows the details of the melting attempts.

Table 10: Results from the attempts of remelting of pure, crushed NZP glass.

(a) NZP-25-22

Temperature	Time	Result
500° C	30 mins	Not melted
550° C	30 mins	Not melted
600° C	30 mins	Not melted
650° C	30 mins	Not melted
690° C	30 mins	Not melted
690° C	90 mins	Melted

(b) NZP-25-23

Temperature	Time	Result
690° C	30 mins	Not melted
690° C	30 mins	Not melted
690° C	60 mins	Not melted
690° C	60 mins	Not melted
750° C	60 mins	Melted

Series 3: Remelting of crushed glass with added Cr:ZnSe powder

Table 11: Attempt at remelting of crushed glass with added Cr:ZnSe powder. NZP-25-24

Temperature	Time	Result
600° C	30 mins	Not melted
700° C	30 mins	Not melted
750° C	30 mins	Melted

The attempt to add Cr:ZnSe powder to crushed glass and then remelting, yielded a similar result as for the remelting of pure glass, as Table 11 shows. The glass only melted at 750° C, and the viscosity was higher than the first time the glass was fabricated.

The resulting glass showed an area of red coloured glass similar to that obtained with the

first process, and an area with clear glass containing large ZnSe particles, as shown in Figure 14a.

<table>
<tr><td>(a) NZP-25-24: Cr:ZnSe agglomerations in doped NZP glass</td><td>(b) NZP-25-25: Micro- and macro-crystals of Cr:ZnSe in NZP glass</td></tr>
</table>
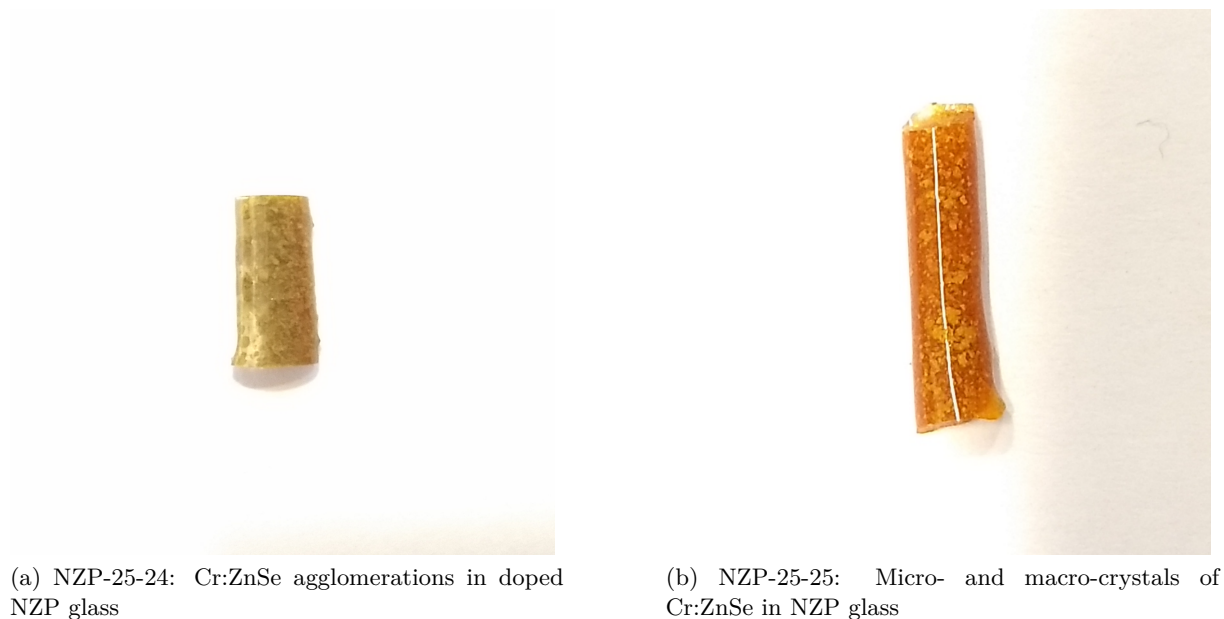
Figure 14

Series 4: Addition of Cr:ZnSe to melted glass

Addition of Cr:ZnSe to melted glass, both at 700° C and 750° C, resulted in exhaustion of black fumes, indicating that Cr:ZnSe is undergoing an undesired chemical reaction.

The resulting glass showed large areas of powder not completely incorporated into the glass matrix, a result of the poor mixing process. This area also showed a strong red colour to the surrounding glass, indicating dissociation of Cr:ZnSe.

As shown in Figure 14b, another area of the sample showed a bright orange colour, indicating that micro-particles of not dissociated Cr:ZnSe have been incorporated into the glass. Even though the time from addition of powder until quenching was kept short, it is evident that some of the powder has diffused into the melted glass.

Series 5: Pure glass fabricated using NaPO$_3$

Using NaPO$_3$ instead of NaH$_2$PO$_4$·2H$_2$O did not result in a reduction of the melting temperature of the glass, as shown in Table 12.

5.1.2 Characterisation

Absorption spectroscopy

Transmission spectra from the NZP samples investigated are shown in Figure 15. The spectra shows that pure NZP glass is transparent in the wavelength region $500 - 2700$ nm. If absorption of light by Cr:ZnSe is taking place, it would show as a dip in the intensity of the transmitted light in the region around 1700 nm. This is not visible in any of the obtained spectra.
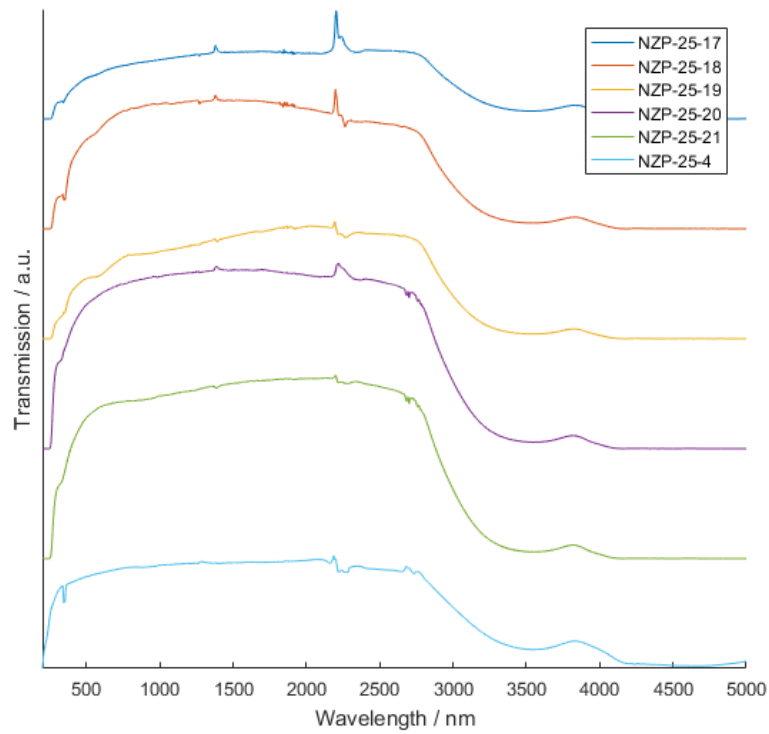
(a) Transmission spectra of phosphate glasses with different Cr:ZnSe doping concentration
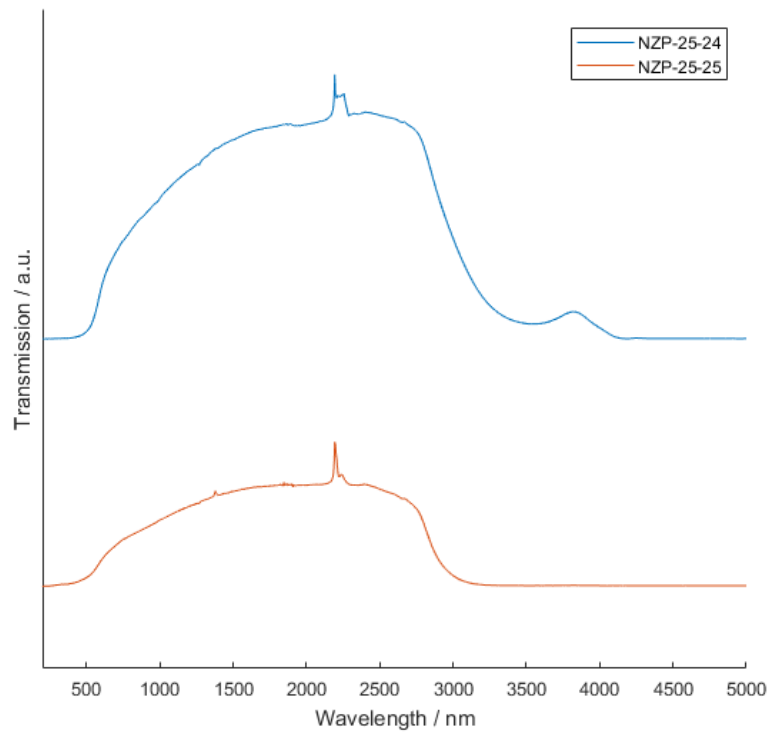
(b) Transmission spectra of phosphate glasses fabricated by adding Cr:ZnSe to melted or crushed glass

Figure 15

Table 12: Investigation of the melting temperature of glass made with $NaPO_3$. (a) Fabrication of pure NZP glass (b) Remelting of crushed NZP glass.

(a) NZP-25-29

Temperature	Time	Result
700° C	60 mins	Not melted
750° C	30 mins	Melted

(b) NZP-25-28, crushed glass

Temperature	Time	Result
700° C	60 mins	Not melted
700° C	60 mins	Not melted
700° C	60 mins	Not melted
750° C	60 mins	Melted

The spectra for NZP-25-17, NZP-25-18 and NZP-25-19 show a faint "shoulder" around 650 nm. This might originate from absorption of Cr^{3+} that has dissociated from ZnSe into the glass matrix [99].

The shoulder is not seen in the spectra for NZP-25-24 and NZP-25-25, even though these samples have similar or higher doping concentrations than the samples mentioned above. These samples do not show a clear cut-off below 500 nm, as the Series 1 samples do. Instead the transmission gradually decreases below 1500 nm.

Peaks in the transmission spectra are observed at around 2200 nm in most of the samples. This peak is barely present in the pure sample and in the samples with low doping concentration, while it is clearly visible in samples with high doping concentration. 2200 nm is in the region of water absorption, meaning water in the atmosphere to a large extent influences the spectra in this region.

Fluorescence spectroscopy

Fluorescence spectra from all the NZP glass samples, along with spectra of a Cr:ZnSe crystal and a pellet of Cr:ZnSe powder, are shown in Figure 16. The spectra of the pure crystal and the pellet was obtained as a reference, to interpret the spectra of the doped NZP glasses.

The fluorescence spectra from the pure Cr:ZnSe crystal and the powder pellet are shown in Figure 16a. The emission of all the samples peak at 2 µm, not around $2.2 - 2.4$ µm, as expected [40]. This is thought to be due to a decrease in sensitivity of the detector above 2 µm, where at 2.6 µm it is completely insensitive.

The measurements show a stronger signal from the powder pellet than from the pure crystal, mainly due to a higher Cr^{2+} concentration in the powder.

Figure 16b shows the signal obtained from NZP glasses from Series 1. Only the samples with 10 and 8 wt% Cr:ZnSe show a weak signal, with the strongest signal originating from the 8 wt% sample. This sample shows the presence of agglomerations of Cr:ZnSe particles near the surface of the glass sample, something that is not clearly visible in the 10 wt% sample.

Figure 16c shows significantly stronger emission signals obtained from NZP-25-24 and NZP-25-25, compared to the signal of the Series 1 samples.

An estimate of the emission cross-sections can be obtained from Equation (2) by using the emission spectra in Figure 16, and $\tau_r = 4.7$µs, the radiative lifetime measured in the glass sample NZP-25-24 [98]. The refractive index of the glass is estimated at 1.52, based on the reported refractive index of pure NZP glass [100].

The number density of Cr^{2+} ions in the area used for fluorescence measurements is estimated
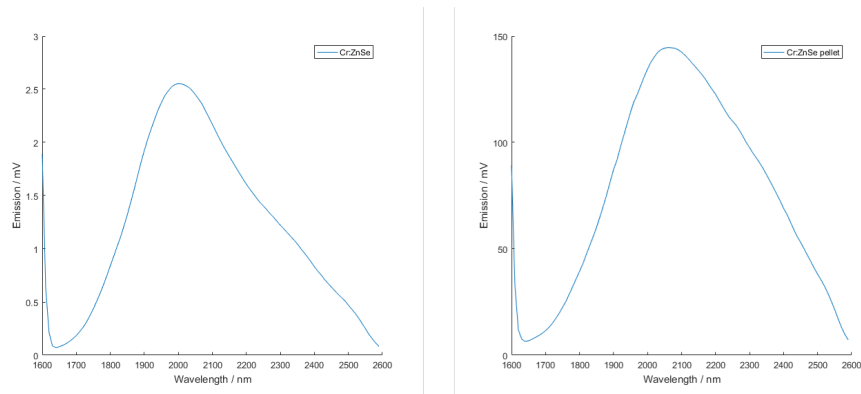
(a) Emission spectra of the pure Cr:ZnSe crystal, and a pellet made from Cr:ZnSe powder. Notice the different values on the axes
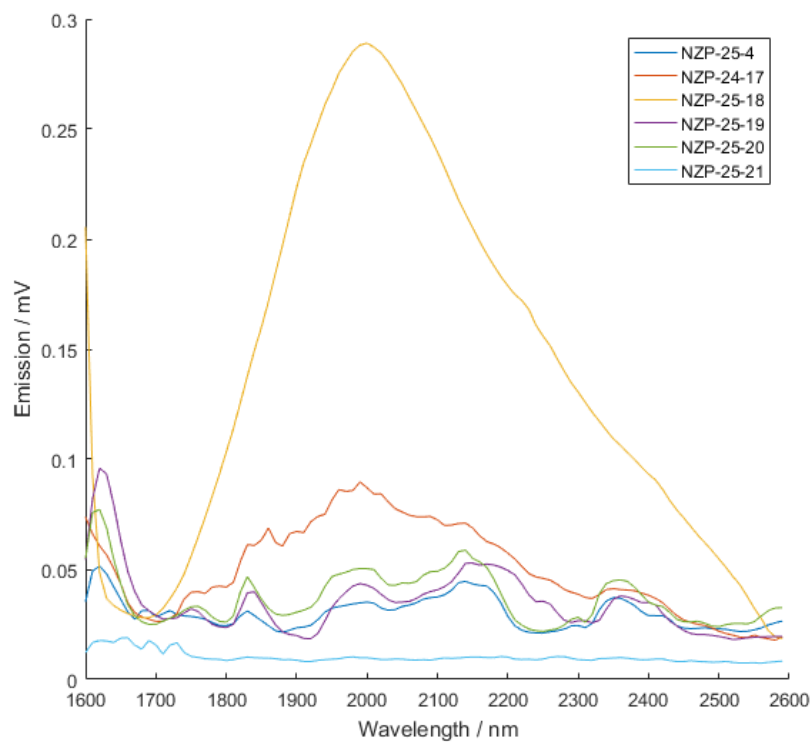
(b) Emission spectra from the NZP glasses doped with $10-2$ wt% Cr:ZnSe, along with a pure reference
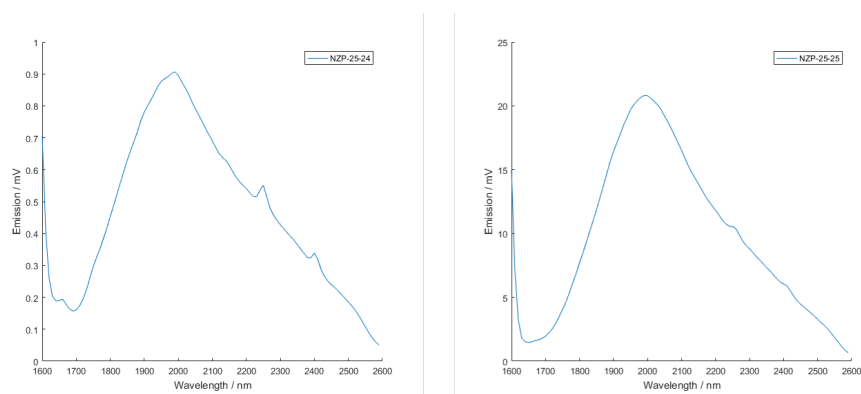
(c) Emission spectra from two NZP samples, fabricated by adding powder to melted or crushed glass. Notice the different values on the axes

Figure 16

49

at about $N \approx 5 \cdot 10^{18}$ cm^{-3} (see A.2). The achievable fraction of excited ions in the glass, n_2, is assumed to be 20%. Knowing this, Equation (1) gives the gain coefficients.

The emission cross-section σ_{em} and the gain g is calculated for NZP-25-25, and shown in Table 13 Calculations of the values are found in A.1 and A.3.

Table 13: Emission cross-section, gain and saturation intensity, calculated for NZP-25-25 at three different wavelengths using Equation (2), (1) and (6)

λ	σ_{em}	g	I_{sat}
2 µm	$4.1 \cdot 10^{-18}$ cm^2	4.1 cm^{-1}	5.1 kW/cm^2
2.2 µm	$3.8 \cdot 10^{-18}$ cm^2	3.8 cm^{-1}	5.1 kW/cm^2
2.4 µm	$3.0 \cdot 10^{-18}$ cm^2	3.0 cm^{-1}	5.9 kW/cm^2
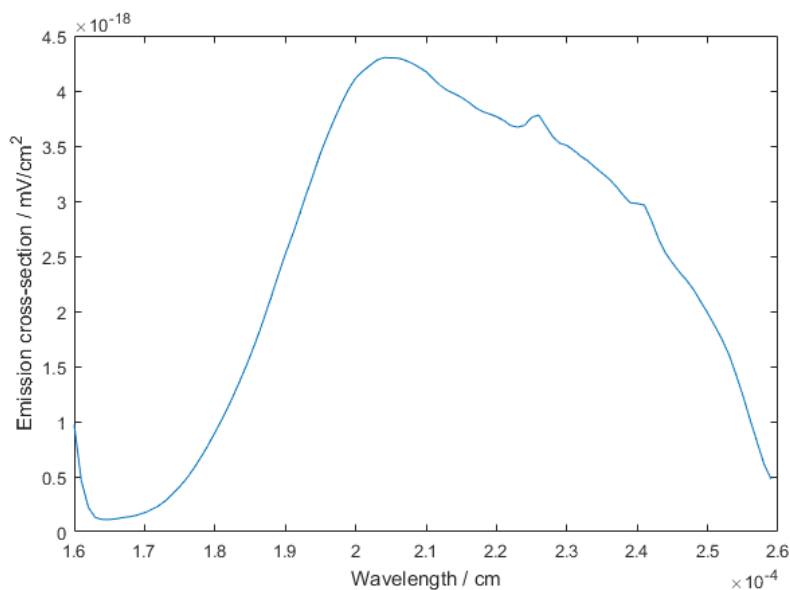
Figure 17: Calculated values for the emission cross-section σ_{em} for NZP-25-25, as a function of the wavelength

As the sensitivity of the detector decreases above 2 µm, the estimated cross-sections at $\lambda = 2.2$ and 2.4 µm are lower than the cross-section at 2.0 µm, even though the peak in the Cr:ZnSe emission should be closer to $2.2 - 2.4$ µm. Figure 17 shows the emission cross-section spectrum of the sample NZP-25-25, showing how it decreases above 2 µm.

Table 13 also show estimated values of the saturation intensity I_{sat}, calculated using Equation (6) (see A.4).

Cut-back loss measurements

The transmitted power when measuring two samples of different thickness in three different areas are shown in Table 14.

The transmitted intensities vary greatly with area of the sample chosen for transmittance. This is not surprising, as the sample show clear optical non-uniformity.

The loss in dB/cm is calculated in three different areas and at two different wavelengths using Equation (11), while a modification of Equation (10) is used to calculate the absorption coefficient α in cm^{-1} (see A.5). These values are also shown in Table 14.

Table 14: Transmitted intensities of NZP-25-25 at $\lambda = 2.4\,\mu m$ and $\lambda = 2.04\,\mu m$

λ	$I(2.48\,mm)$	$I(0.50\,mm)$	$\alpha(dB/cm))$	$\alpha(cm^{-1})$	Area
	2.55 mW		1.66	0.38	Clear area without powder
$2.04\,\mu m$	0.06 mW	2.75 mW	83.9	19.3	On powder spot
	1.98 mW		7.21	1.66	Edge of powder spot
	5.86 mW		7.74	1.78	Clear area without powder
$2.4\,\mu m$	0.03 mW	8.34 mW	123.4	28.4	On powder spot
	6.40 mW		5.81	1.34	Edge of powder spot
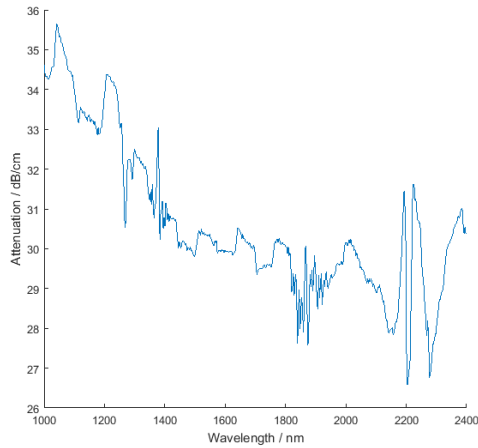
(a) Attenuation in dB/cm
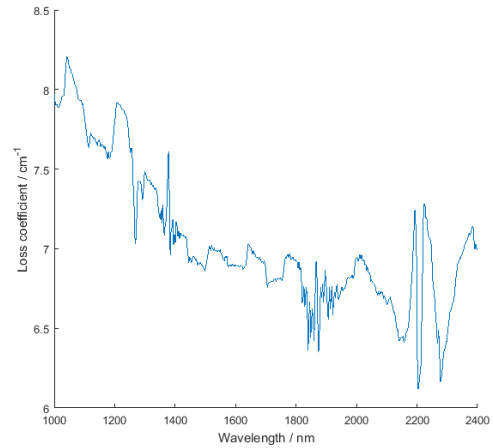
(b) Loss coefficinet in cm^{-1}

Figure 18: Loss spectra of NZP-25-25, obtained using the OLIS spectrophotometer on two samples of different thickness

Figure 18 shows calculated loss spectra obtained from the large aperture OLIS transmission spectra, giving the average loss over the whole sample at different wavelengths. Most notably, $\alpha(2.04\,\mu\mathrm{m}) = 29.7\,\mathrm{dB/cm} = 6.85\,\mathrm{cm}^{-1}$ and $\alpha(2.4\,\mu\mathrm{m}) = 30.4\,\mathrm{dB/cm} = 6.99\,\mathrm{cm}^{-1}$, confirming that the average value over the sample is located somewhere between that obtained for the clear area and the areas covered with Cr:ZnSe agglomerations.

Differential scanning calorimetry
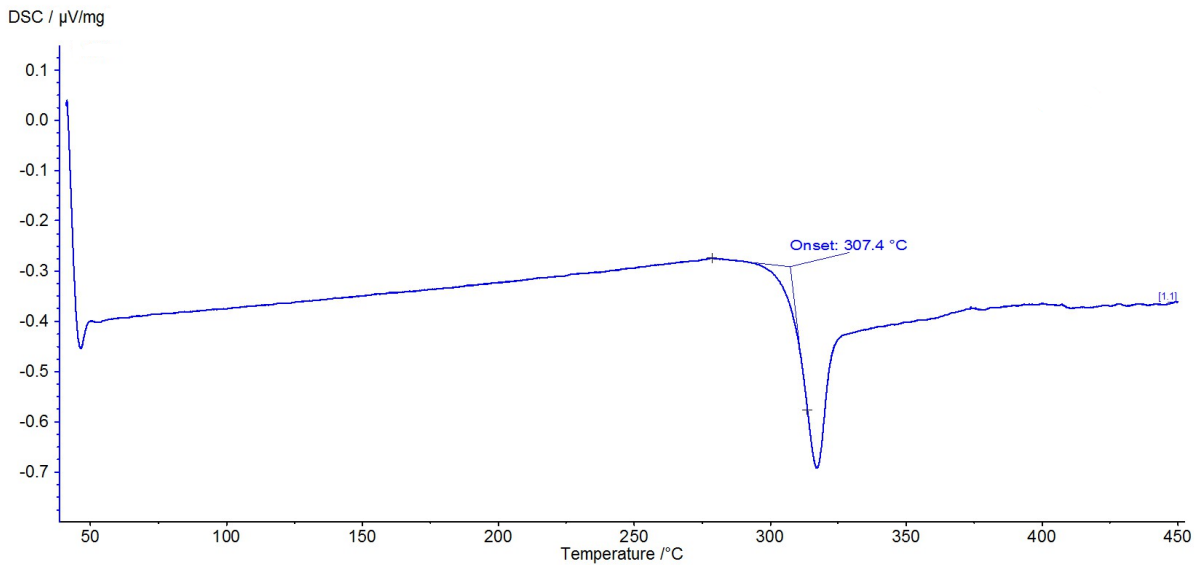
Figure 19: DSC spectra obtained for the sample NZP-25-17. The graph shows the energy needed to heat the sample, compared to a reference. The region where the energy requirement reduces drastically is identified as the region of the glass transition, giving the glass transition temperature T_G

The glass transition temperatures of the NZP samples are shown in Table 15, while Figure 19 shows a plot of a representative DSC graph.

The uncertainty of the DSC measurements are about $T_G \pm 5°\,\mathrm{C}$. Most of the measurements are within this uncertainty range. This means that even though the trend in the measurements of Series 1 is that T_G of the glasses increases with increased doping concentration, nothing definite can be stated regarding these samples.

The exceptions are sample NZP-25-4, NZP-25-25, NZP-25-26 and NZP-25-27. NZP-25-4 and NZP-25-27 are pure glasses, indicating that doping with Cr:ZnSe increases T_G of the glasses. NZP-25-25 and NZP-25-26 do not have a uniform distribution of Cr:ZnSe in the glass, but show large Cr:ZnSe agglomerations in certain areas, making other areas of the glass practically pure.

Raman spectroscopy

Raman spectra of pure NZP glass (NZP-25-5), and NZP glass doped with 6 wt% Cr:ZnSe (NZP-25-19) are compared in Figure 20. Three spectra are obtained from the doped NZP glass. The first is captured in an area with a light red colour of the glass. The second spectra is from an area with a dark red colour of the glass. The third spectra is captured when focusing the beam
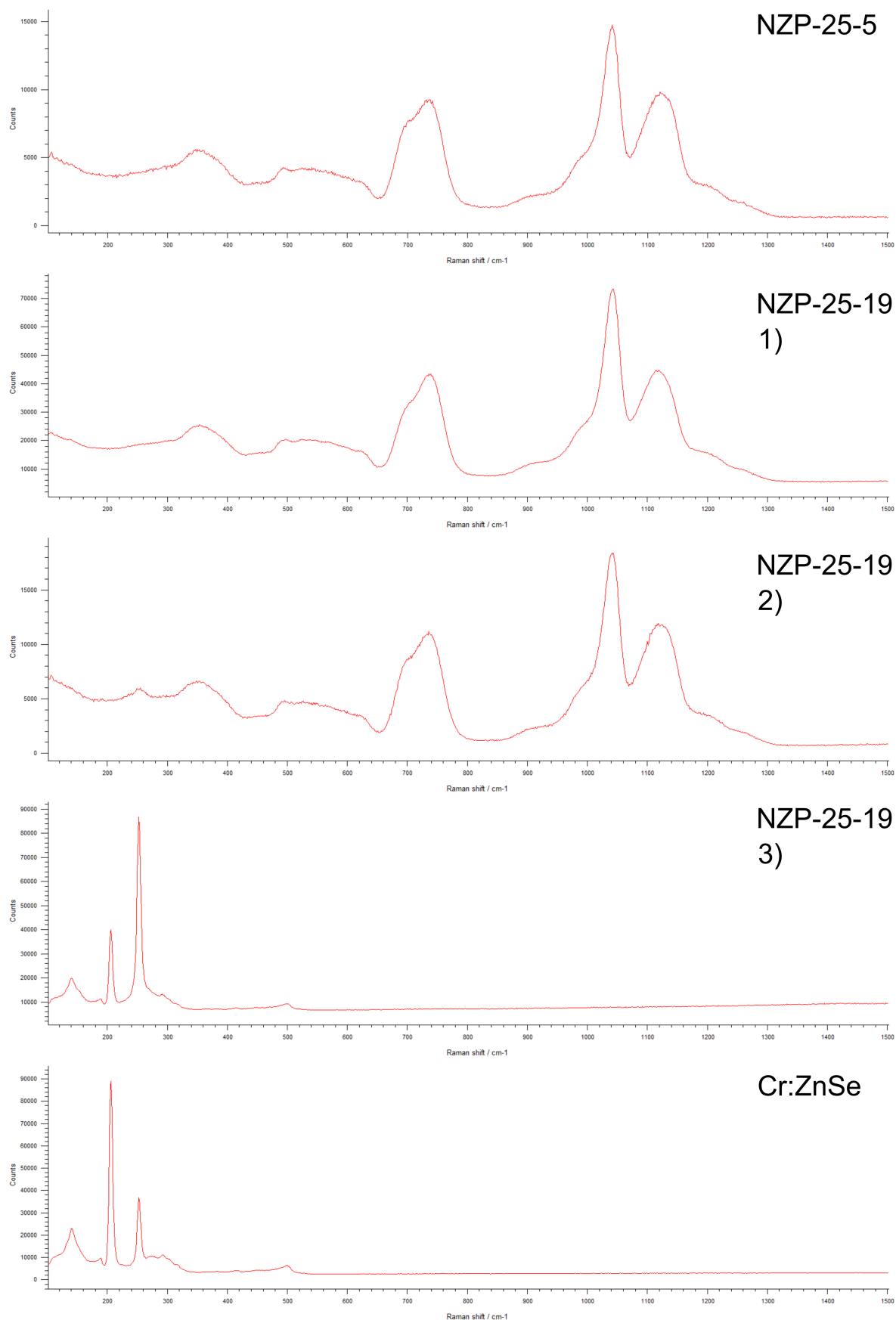
Figure 20: Raman spectra of NZP glass and Cr:ZnSe. The top figure shows the Raman spectra of pure NZP glass. The three figures of NZP-25-19, glass doped with 6 wt% Cr:ZnSe, show Raman spectra in areas of 1) light red colour, 2) dark red colour, 3) on Cr:ZnSe spot. The bottom figure shows Raman spectra of a Cr:ZnSe crystal.

Table 15: Glass transition temperature T_G of all the fabricated NZP glasses.

Sample	wt% Cr:ZnSe	T_G
NZP-25-17	10	307.4° C
NZP-25-18	8	307.4° C
NZP-25-19	6	305.2° C
NZP-25-20	4	304.8° C
NZP-25-21	2	303.7° C
NZP-25-4	0	299.6° C
NZP-25-24	10	305.9° C
NZP-25-25	10	294.7° C
NZP-25-26	5	294.4° C
NZP-25-27	0	293.5° C
NZP-25-29	0	302.1° C

on a Cr:ZnSe particle in the glass. The final spectra shows the Raman spectra of a pure Cr:ZnSe crystal.

The Raman spectra of the pure NZP glass show a spectra characteristic of a metaphosphate glass with a metal-oxide network modifier, as discussed in section 3.2.5. The expected peak around $700\,\text{cm}^{-1}$ is shifted to longer wavenumbers, due to the reduction in P-O-P bond angle with decreased chain length. The peak around $1270\,\text{cm}^{-1}$ is completely dampened due to the large ZnO content, while a new peak around $1130\,\text{cm}^{-1}$ appears. According to Equation (8) and (9), the produced NZP glass should contain 33% Q^2 groups and 67% Q^1 groups, something that agrees with the observed Raman spectra.

Figure 20 shows that the Raman spectra of pure NZP glass, and NZP glass doped with 6 wt% Cr:ZnSe, are very similar. In the second spectra of NZP-25-19, obtained in an area with a dark red colour, a small peak is visible around $255\,\text{nm}$. This peak coincides with the LO stretch in Cr:ZnSe, and is a possible source. This peak is clearly visible in the Raman spectra of NZP-25-19 on a Cr:ZnSe spot.

Comparing the Raman spectra of NZP glass focusing on a Cr:ZnSe spot with that of pure Cr:ZnSe, it is seen that these spectra closely resemble one other. The signal from the Cr:ZnSe particles in NZP glass overshadows the Raman spectra of the NZP glass itself.

5.2 Graphene Saturable Absorbers

5.2.1 Fabrication - Graphene Transfer

The attempts at graphene transfer on Si wafers yielded varying results with different processes. There were three steps in the process that influenced the quality of the final result: Cu foil handling, transfer and drying

Cu foil handling

Due to the thickness of the Cu foil, the handling had to be very careful, to avoid wrinkles in the material. The author spent several attempts practising cutting and handling techniques of the Cu foil. In the end, cutting the Cu foil by pressing a scalpel through the foil worked better than cutting by dragging the scalpel along the foil. Instead of lifting the cut out Cu sample away

from the surrounding Cu foil, the surrounding foil was moved, ensuring minimal movement of the Cu sample.

Transfer

The transfer process was critical, as the sample was only kept together by a 500 nm thick PMMA layer that would break if the surface tension with water was broken. It was critical for the entire graphene sheet to be placed on the plastic foil used for transferring.

Drying

The effects of the different drying mechanisms on the graphene sample are shown in Table 16. Drying in air is the most suitable way of increasing adhesion between the graphene and the substrate, as it does not lead to difficulties with PMMA removal. The only downside to this treatment is that it is time consuming. Heat treatment at low temperature speeds up the process of water removal and increases adhesion, but one has to be careful, as excessive heat treatment led to difficulties in removing PMMA.

Table 16: Different mechanisms for drying the graphene transfer sample, with outcomes

Process	Result
Drying in air, laying flat	Time consuming, increases adhesion
Drying in air, tilted	Reduces time, increases adhesion due to capillary forces
Hotplate, 80° C	Removes water, increases adhesion
Hotplate, 110° C	Difficult to remove PMMA
Pressing graphene with N_2 gun	Distorts and damages sample

The heat treatment did not reduce the amount of wrinkles in the graphene sheet, as seen in Figure 21. The wrinkles present after transfer, were still present after 10 minutes on a hotplate, and are shown in the finished sample as lines where graphene did not adhere.

In the end, transfer of graphene onto a silver mirror was achieved. Unfortunately, a large portion of the transferred graphene did not adhere to the silver mirror, and only the areas that show clear PMMA residue also had large amounts of graphene left.

This might have been due to the different thickness and thermal conductivity of the silver mirror compared to the thin Si wafers, making the heat treatment less effective. Another possibility is that the coating of the silver mirror inhibits the adhesion of graphene to the mirror.

5.2.2 Characterisation

Raman spectroscopy

Optimisation of laser power and acquisition time for Raman measurements of graphene, yielded the results shown in Figure 22. Below 5 % laser power, the Raman signal was too weak to detect the graphene peaks, showing only noise. A laser power of 50 % damaged the sample due to heating. Using 5 and 10 % laser power, a decent Raman spectra was obtained. An increase in acquisition time increased the signal to noise ratio, but also with 10 s acquisition time the signal was clearly visible. To reduce the time required to obtain maps of large areas, an aquisition time of 10 s was chosen.

(a) After 1 hour of drying in air
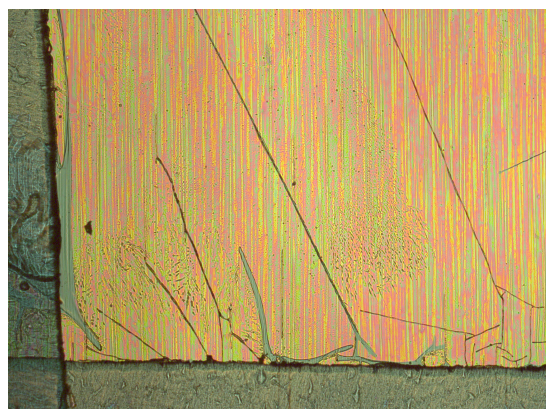
(b) After 10 minutes on a hotplate at 80° C

(c) After 2 hours in acetone to remove PMMA

Figure 21: Graphene on SiO$_2$ after transfer. The images are from different steps in the process of increasing adhesion to the underlying substrate, the last image is the final sample
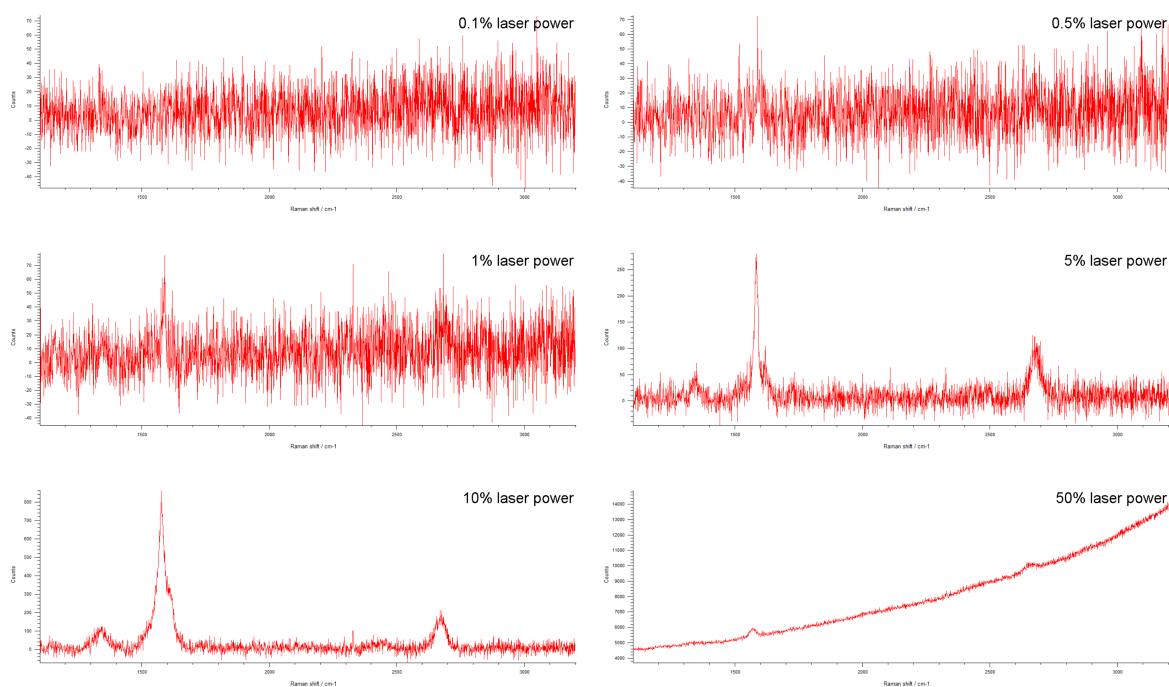
(a) Laser power optimisation. All spectra were acquired with a 10 s acquisition time. The Raman spectra of graphene is visible at 5 % and 10 % laser power, while 50 % laser power resulted in a temperature that damaged the sample
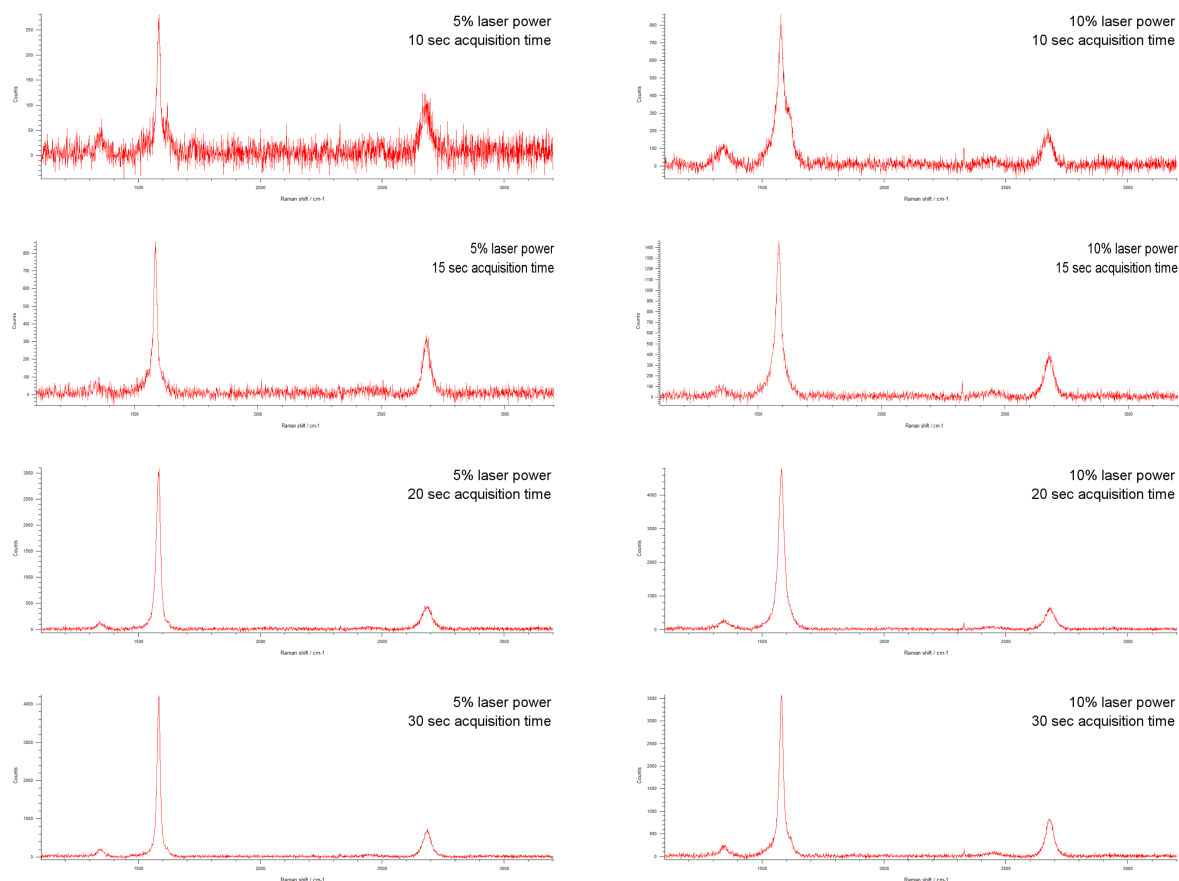
(b) Acquisition time optimisation. Increasing the acquisition time increases the signal and reduces the noise, but also with 10 s acquisition time the signal is clearly visibl

Figure 22

The Raman spectra obtained from the transferred graphene typically showed the two main peaks G and 2D, along with the disorder peak D. Maps with size 10×10µm of the transferred Raman samples, show the variation in the intensity ratio of the different peaks. The ratio of the intensities of the D and G peaks is a measure of the degree of defects in the graphene. As seen in Figure 23d, the ratio varies across the sample, with regions of higher and lower amounts of defects.

(a) Distribution of intensities of the G peak

(b) Distribution of intensities of the 2D peak

(c) Distribution of intensities of the D peak

(d) Ratio of intensities of the D and G peak
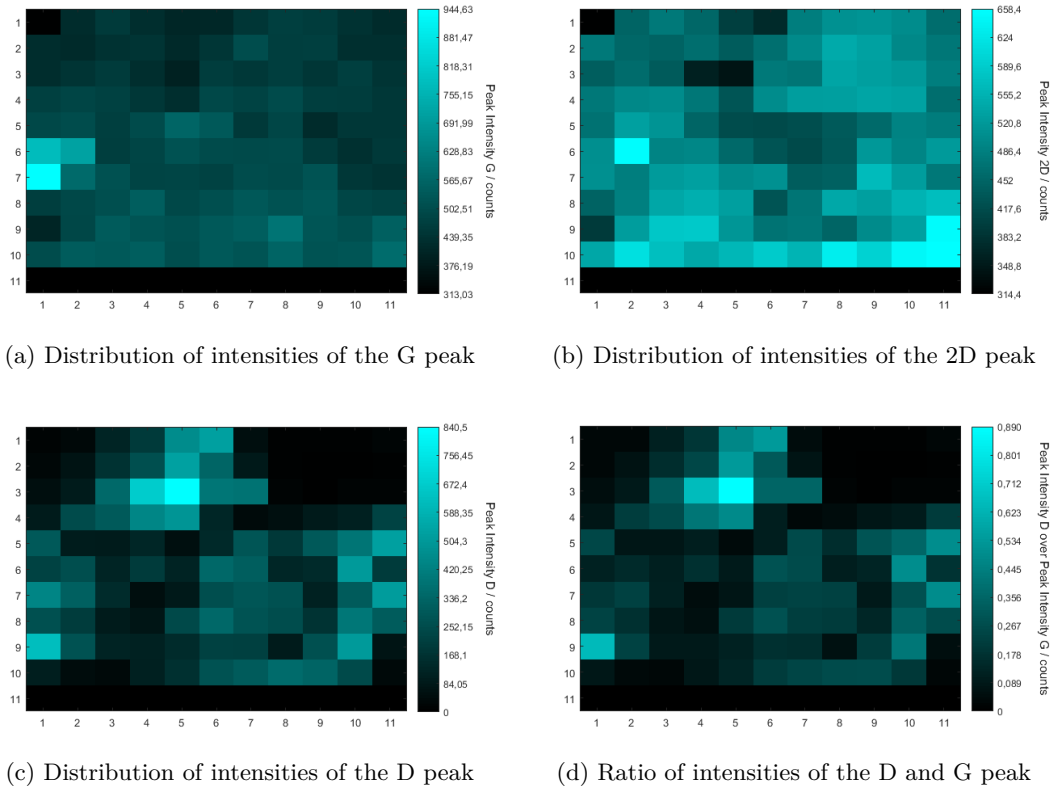
Figure 23: 10×10µm map of graphene transferred onto a Si wafer. Laser power: 5%. Acquisition time: 10 s

The amount of defects between the transferred graphene samples were relatively constant, changes made to the process did not result in significantly more or less defects. The defect distribution on the graphene silver mirror eventually fabricated, is assumed to be comparable to that shown in Figure 23.

At 50% laser power, the laser damaged the graphene mirror samples. A visual inspection showed a black hole in the sample, while the Raman spectra obtained had the characteristics of a blackbody distribution.

Using MATLAB and fitting the Raman spectra to the Planck formula for blackbody radiation,

$$B(\lambda, T) = \frac{2hc^2}{\lambda^5} \frac{1}{e^{\frac{h\nu}{k_B T}} - 1}$$

the laser temperature is estimated at about 1398° C (See A.6). The fitted curve is shown in Figure 24. As the Raman setup does not let us choose arbitrary laser powers, it is not possible to find the lowest temperature that damages the mirrors.

Previous experiments done in the group show that the saturable absorber continues working as a saturable absorber also in the case of holes burnt into the mirror. This indicates that the laser
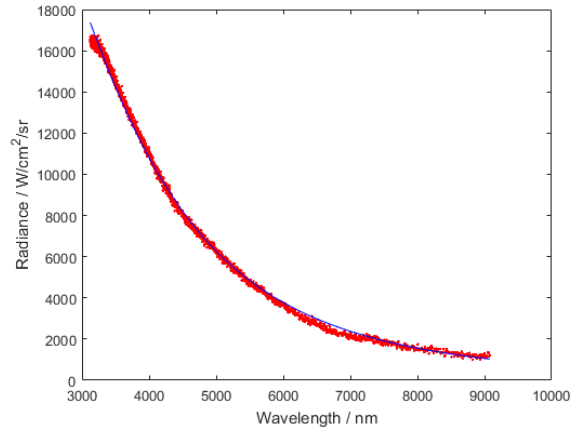
Figure 24: Raman spectra of graphene on silver mirror, obtained at 50% laser power and 10 s acquisition time. Curve fitted to Planck's formula for blackbody radiation. This fit was achieved for an estimated temperature of 1398° C

does not damage the graphene [101]. The prevailing theory has been that the laser damages the PMMA residue from the graphene transfer. This theory was rejected, as hole burning were shown also in areas of the mirror not containing graphene, and therefore not containing PMMA. Samples of graphene on Si wafer substrates did not show any signs of damage, even with large amounts of PMMA residue. This supports the theory that it is not graphene or PMMA, but rather the coating of the silver mirror that is damaged by the laser.

Mode locking a Cr:ZnS laser

The graphene mirror provided successful mode locking of the Cr:ZnS laser. Figure 25a shows both continuous wave and mode locked spectra of the laser, and how the losses in graphene shifts the central wavelength of the laser from 2.4 μm in CW to 2.35 μm in the mode-locked regime.

The input/output characteristics of the laser, both in the mode locked and continuous wave regime, are shown graphically in Figure 26. In the mode locked regime, the laser threshold was found to be 0.4 W, while the threshold for the continuous wave regime was 0.3 W. This is most likely due to the different cavity geometry obtained when moving the graphene mirror, and not due to the mode locking process itself.

Figure 25b shows mode locked spectra obtained at 3 W and 0.8 W input pump powers, with bandwidths 55 nm and 14 nm respectively. As the duration of a mode locked laser pulse depends on the bandwidth, the pulses obtained at 3 W are shorter than the pulses obtained at 0.8 W. This means tuning of the bandwidth and the pulse length is possible.

At 3.2 W input pump power, the mode locking starts to break, giving both mode locked and continuous wave characteristics to the laser output. Spectrally, this shows as a broadband mode locked spectra, with CW peaks on top. After operation for some time at 3.6 W input pump power, mode locking broke completely, resulting in a continuous wave.

The minimum input power necessary to sustain mode-locking was 0.8 W. At this value, the measured output power was 21 mW. This can be used to calculate the saturation energy fluence, J_{sat}, of the graphene mirror.

The saturation energy fluence is given by Equation (7). As the output coupler has a transmission of 8% and the losses in the optical isolator are 30%, the energy inside the laser cavity is
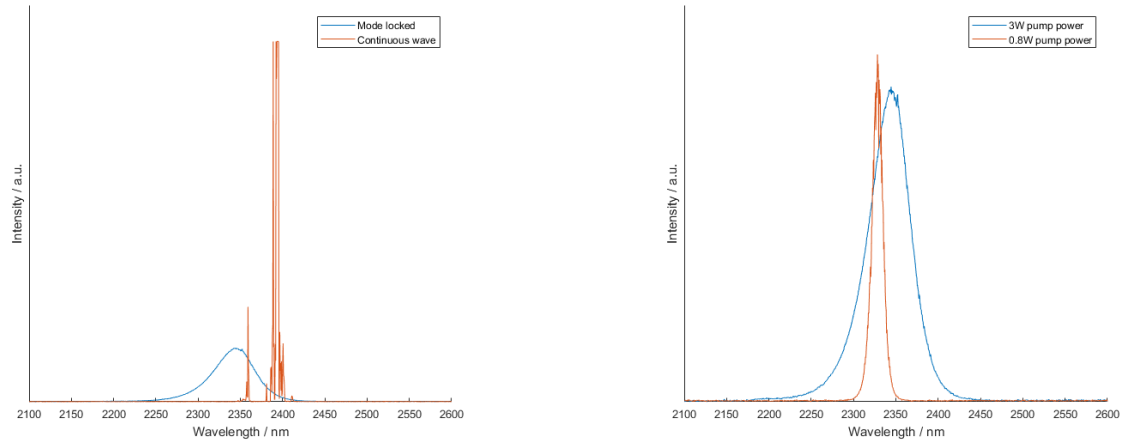
(a) Continuous wave and mode locked spectra of a Cr:ZnS laser

(b) Mode locked spectra of a laser with 3W and 0.8W input pump power, with bandwidths 55 nm and 14 nm respectively

Figure 25
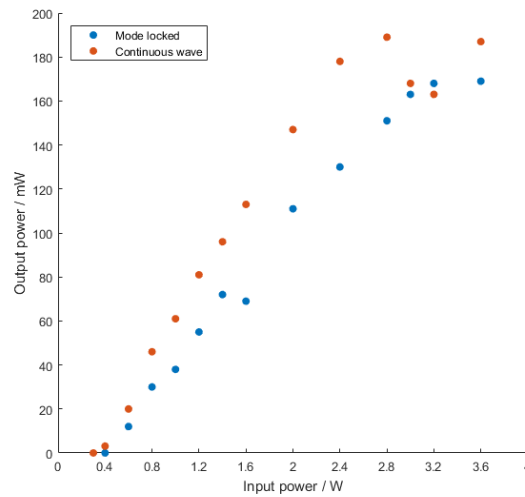
Figure 26: Input/output power for a Cr:ZnS laser in the mode locked and continuous wave regime

significantly higher than the measured output energy. Using the repetition rate $F_{rep} = 250\text{MHz}$ of the laser pulses (Figure 27b), an estimate of the saturtion energy fluence of $J_{sat} = 4.8\mu\,\text{J/cm}^2$ is found (see A.7 for calculations).

The maximum energy fluence the graphene can handle before mode locking breaks, can be found in a similar manner for an input power of 3.6 W, with a measured output power of 130 mW. The calculation yields a fluence of $29.6\mu\,\text{J/cm}^2$.

With operation, the graphene showed signs of degrading. Achieving mode locking became harder and harder, and in the end mode locking was not sustained for a longer period of time. To achieve mode locking, a new area of the graphene mirror had to be tuned in.

Autocorrelator measurements

The processed data from the autocorrelator measurements are shown in figure 27a. Using this plot, the FWHM of the autocorrelator intensity signal is found at $\tau_{AC} = 168.1\,\text{fs}$.

Using tabulated values for a sech^2 pulse shape, the laser pulse duration is determined at $\tau_{pulse} = 0.6482 \cdot \tau_{AC} = 109\,\text{fs}$.
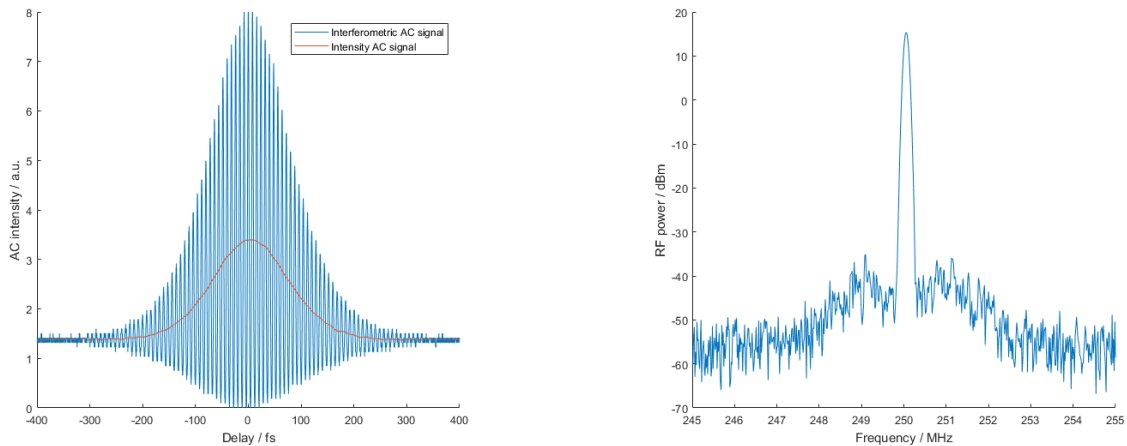
(a) Autocorrelator signal for a Cr:ZnS laser mode locked by a graphene saturable absorber, with 3W input power

(b) Radio frequency spectrum, showing the repetition rate of the mode locked pulses

Figure 27

The stability of the mode locking operation is investigated by measuring the repetition rate of the laser pulses. Figure 27b plots the radio frequency spectrum, showing a repetition rate of 250 MHz.

As a mode locked pulse is released with every pass of the light in the cavity, the repetition rate of the laser pulses can be used to calculate the cavity length in the laser. In this case, the cavity length is shown to be about 1.2 m.

6 DISCUSSION

6.1 Phosphate Glasses Doped With Cr:ZnSe

6.1.1 Challenges with Glass Fabrication

Despite attempts at lowering the melting temperature of the phosphate glass, by crushing glass into powder and remelting, and by changing the compound powders, the phosphate glasses did not melt below 750° C. T_G also did not show a significant change with varying composition and fabrication method.

For this reason, to avoid dissociation of Cr:ZnSe, the powder had to be added to the melted glass as close to the annealing as possible. This showed to result in successful incorporation of Cr:ZnSe, where fluorescence has been demonstrated and lifetime has been measured.

A challenge when adding Cr:ZnSe powder only minutes before annealing, was the lack of stirring equipment. This resulted in powder not evenly distributed in the glass, and the areas of Cr:ZnSe incorporation showed concentrations significantly higher than the target 10 wt%. This problem could be solved by acquiring suitable stirring equipment, to distribute the powder in the molten glass.

The red colour showed in areas of almost all the glasses, is assumed to originate from Cr^{3+} ions dissociating into the glass. Cr^{3+} and higher valencies of Cu absorbs in the visible part of the spectrum, cutting the green and blue frequencies [98]. For this reason, glass including Cr^{3+} ions appear red.

A challenge in all the glasses was Cr:ZnSe agglomerating, and sinking to the bottom of the glass melt. Reducing the time of Cr:ZnSe spent in the molten glass, as well as introducing a stirring mechanism, is believed to be a promising start in alleviating this problem.

6.1.2 Characterisation

Absorption spectroscopy

The absorption spectra does not show the expected absorption around 1800 nm, indicating absorption in Cr^{2+}.

One possible explanation for the lack of visible absorption, is that Cr has dissociated from the ZnSe crystal, and entered the glass as Cr^{3+}. This theory is supported by the appearance of a faint shoulder around 650 nm, visible in three of the first samples fabricated. This shoulder is not present in the absorption spectra of NZP-25-24 and NZP-25-25, indicating that less Cr has dissociated from ZnSe in these samples. This is also supported by the transmission spectra.

Another possible explanation for the lack of visible absorption around 1800 nm, is that scattering in the material disturbs the transmission spectra, covering the possible absorption dip. This is supported by the high values of losses registered in the samples.

All of the absorption spectra show a slight disturbance around 2200 nm. The peak is more prominent in samples with high Cr:ZnSe concentration, indicating the material as the origin. Either due to a contamination or some other unwanted effect, the peak is considered at the moment being an artefact not related to the desired characteristics. Another possibility is an instrumental artefact.

Fluorescence spectroscopy

For all of the Series 1 samples, only NZP-25-17 (10wt% Cr:ZnSe) and NZP-25-18 (8wt% Cr:ZnSe) show an emission signal. The signal of NZP-25-17 is barely stronger than the noise in the measurements, indicating that the amount of fluorescent Cr^{2+} in the sample is very small, or that the signal is quenched. NZP-25-18 shows presence of agglomerations of Cr:ZnSe particles, and exhibits a stronger signal than NZP-25-17. The Cr:ZnSe agglomeration increases the concentration of Cr^{2+} ions enough to show a clear fluorescence signal. The signal is still two orders of magnitude lower than that obtained in NZP-25-25, indicating that a large amount of ions have dissociated.

The strong signal obtained from both NZP-25-24 and NZP-25-25 show the potential of these fabrication methods for incorporation of Cr:ZnSe into glass. The highest fluorescence signal from a glass sample is obtained from NZP-25-25. The distribution of Cr:ZnSe powder in this glass was not uniform, giving areas of Cr:ZnSe concentration higher than 10wt%. This is assumed to contribute to the strong signal shown in the sample.

Emission cross-section

As already mentioned, due to poor calibration and lowered sensitivity of the photodetector above 2 μm, the fluorescence spectra peaks around 2 μm, instead of around the expected $2.2 - 2.4$ μm.

For that reason, the calculated value of the integral in Equation (2) is lower the actual value. This leads to a small denominator, and an overstatement of the calculated σ_{em} at 2 μm. At larger wavelength, the value for $I(\lambda)$ is also smaller than the actual value, compensating for the denominator, and maybe even leading to an underestimation of σ_{em}.

The calculated emission cross-sections for NZP-25-25 are somewhat higher than those commonly reported for Cr:ZnSe, of about $\sim 1.3 \cdot 10^{-18}$ cm^2 [102]. Even though the calculated value does not correspond exactly to the reported value, it is of the correct order of magnitude, around 10^{-18} cm^2. This is a very positive result, which demonstrates that the technological approach is correct and works.

The estimated value of I_{sat} in the glasses, of about 5.1 kW/cm^2, is lower than the reported saturation intensity of bulk Cr:ZnSe crystals of $I_{sat} = 11$ kW/cm^2 [102]. This is likely due to the overestimate of the emission cross-section, along with loss processes in the material that are not taken into account in Equation (6).

Losses

Typical values for losses of an optical silica fiber is on the order of $\sim$ 1dB/km [103]. Chalcogenide glasses typically possess losses of $\sim$ 1dB/m [104], while typical values for phosphate glasses are in the same range [105]. This shows that the losses measured in the doped phosphate glass, on average of the order of 30 dB/cm, are significantly higher than what can possibly be achieved.

The doped glasses show highly non-uniform losses throughout the sample, where scattering on large Cr:ZnSe particles creates high losses, while areas without large particles show higher transmission. Focus when fabricating the samples should therefore be on distributing the powder uniformly in the glass, avoiding large agglomerations.

As a second step, making the Cr:ZnSe particles smaller (sub λ), will further reduce the scattering, as the Rayleigh scattering cross-section decreases with the sixth power of the particle size, shown by the equation [106]

$$\sigma = \frac{128\pi^5 r^6}{3\lambda^4}\frac{n^2 - 1}{n^2 + 2}$$

where r is the radius of the particle, λ is the wavelength of the scattered radiation, and n is the refractive index of the material. As the equation shows, reducing the particle size is the most effective way of reducing the Rayleigh scattering.

The losses obtained with a small aperture at highly localized areas of the sample, show tendencies of being higher at $2.4\,\mu m$ than at $2.04\,\mu m$. This is confirmed in the spectra in Figure 18. This is mainly due to OH groups in the glass, absorbing in this region. Even with a careful gradual heating to eliminate water in the glass, some water is still present, as seen by the increased losses.

Comparison of loss and gain

To evaluate if a material has potential to be used as a laser active material, the gain and loss are compared. If the gain is larger than the losses, lasing can be obtained.

Comparing the gain at $2\,\mu m$ with the losses at $2.04\,\mu m$, show that in the clear areas of the sample, the losses are an order of magnitude lower than the gain ($g(2\mu m) = 4.12\,cm^{-1}$ vs. $\alpha(2.04\mu m) = 0.38\,cm^{-1}$). This indicates that with even distribution of Cr:ZnSe particles, the material is promising as a laser active material. In areas with Cr:ZnSe agglomerations, the losses are ~ 5 times larger than the gain. This shows that areas with Cr:ZnSe particle agglomerations are detrimental, and lead to large scattering losses exceeding the gain in the material. The average value of losses ($6.85\,cm^{-1}$) exceeds the gain, showing that the scattering in the material is still too high for laser action.

Still, this is a very promising beginning for the fabrication of this new type of laser material. These are the very first successful attempts at their fabrication, and several steps can be made to reduce the scattering losses. As already mentioned, the strategy to decrease the losses is, as a first step, to ensure homogeneous particle dispersion by stirring, and as a second step, to fabricate smaller micro-crystals of uniform size, if possible in the sub-1 µm range.

Raman spectroscopy

The lack of Cr:ZnSe spectra in NZP-25-19 outside of the Cr:ZnSe spot, indicates that either micro-crystalline Cr:ZnSe is not incorporated into the glass to a large extent, or that the signal from the micro-particles is quenched by the glass. As the Raman signal of Cr:ZnSe agglomerations in glass is substantially stronger than the Raman signal from the phosphate glasses, one would expect the peaks to show also at lower concentrations.

Still, the weak peak shown in the dark red area of the glass in Figure 20 coincides with the LO peak of Cr:ZnSe, indicating that at least some micro-crystals are incorporated into the glass.

6.2 Graphene Saturable Absorbers

6.2.1 Fabrication - Graphene Transfer

Currently, the challenges in the graphene transfer process lies in the reproducibility of the process, as the end result depends to a large extent on the handling of the material. The only way to overcome this challenge is believed to be by practice, or by acquisition of "easy transfer" graphehe [107]. Easy transfer graphene is already processed with an added PMMA layer and a removed Cu layer, and so is ready for transfer. This significantly reduces the processing time in the lab, and reduces the amount of personal errors that can be made. This graphene is about ten times as expensive as regular graphene on Cu foil [96], making this a cost vs. gain priority that has to be done based on economy and available time.

The heat treatment of the transferred graphene is a critical process for ensuring adhesion of the graphene to the substrate. On a hotplate, the effect is determined by the thickness and the thermal conductivity of the substrate. To eliminate this parameter, a baking furnace can be used.

The 200K PMMA A12 used in this process is suitable, as it provides the thickness of the PMMA layer required to yield mechanical stability. A PMMA solution with shorter polymer chains, can yield the same thickness when spin coated using lower rpm. The problem encountered with PMMA removal should be alleviated with shorter polymer chains [79].

6.2.2 Characterisation

Raman spectroscopy

The Raman spectra of the graphene SA showed the expected G and 2D peaks, along with the D peak indicating defects in the material. This is as expected.

The Raman spectra indicated that heating occurs in the mirror at high laser intensities. This is unfortunate, as heat induced damage to the substrate can lead to distortions of the graphene layer. To avoid this problem, a substrate with better thermal conductivity, such as YAG (yttrium aluminum garnet) or sapphire, could be used in the future experiments.

Mode locking a Cr:ZnSe laser

Successful mode-locking of the Cr:ZnS laser was achieved. According to the author's knowledge, this is the first time mode-locking has been achieved using a graphene SA on a silver mirror. This opens the way to production of rather cheap and versatile silver based graphene saturable absorber mirrors, also for industrial laser production.

The calculated saturation energy fluence of graphene of $4.8\,\mu\,J/cm^2$ is significantly lower than values typically reported. Authors have suggested that saturation energy fluence of graphene decreases with wavelength [19]. The result obtained here agrees with this trend, with reported values of $66\mu\,J/cm^{-2}$ at $800\,nm$ [45], $14\mu\,J/cm^{-2}$ at $1500\,nm$ [75]), and now $4.8\mu\,J/cm^{-2}$ at $2400\,nm$. As this wavelength dependence favours operation at longer wavelengths, graphene shows to be a suitable SA for mode-locking of the targeted all-fiber glass laser operating in a broad spectral region in the mid-IR.

7   CONCLUSION AND OUTLOOK

7.1   Conclusion

A completely new type of glass-ceramic laser material has been developed, emitting in the mid-IR range. A new type of graphene saturable absorber on a silver mirror has also been developed. These components are key components in the future femtosecond pulsed glass-ceramic fiber laser that is the ultimate goal of this research, operating in the broad wavelength range between 2 and 3 μm.

In the course of this work, several conclusions have been made:

- Incorporation of micro-crystalline Cr:ZnSe particles into phosphate glasses, has shown to be a promising route for fabrication of a fiber lasers with broadband emission. The obtained doped glass has shown fluorescence emission in the region $1.6 - 2.6$ μm, characteristic of Cr:ZnSe. The lifetime of the emission was measured at 4.7 μs, showing that incorporation into the glass matrix did not significantly reduce the lifetime from that of the pure Cr:ZnSe powder, with a measured lifetime of 5 μs.

- The main challenges currently lie in inhibiting dissociation of Cr^{2+} from the ZnSe crystals, and in ensuring a homogeneous distribution of the particles in the glass. Reducing the amount of time the Cr:ZnSe crystals spend above $700°$ C has shown to be a promising beginning in inhibiting Cr:ZnSe dissociation. With the development of a suitable stirring mechanism, it is believed that homogeneous particle dispersion can easily be achieved.

- Large scattering losses were measured due to lack of optical uniformity of the samples, with large variations in measured losses depending on region of measurement. Increasing uniformity of the particle distribution, and reducing the size of the micro-crystals in the glass is an important first step towards lowering the amount of scattering losses.

- Comparison of loss and gain in the material shows that despite high losses, the gain exceeds the losses in regions without large Cr:ZnSe agglomerations. This shows that with a more homogeneous distribution of particles, the material is promising as a gain material,

- The developed transfer process of graphene monolayers has shown to yield promising results, as the first mode-locking of a Cr:ZnS laser using graphene transferred onto silver mirrors has been demonstrated. The extremely low saturation energy fluence allowed mode-locking also at very low power. This result, although surprising, agreed with literature indicating that saturation energy fluence decreases with longer wavelength.

- The main challenge currently lies in ensuring reproducibility of the process, as human error is a large factor presently. The durability of the transferred graphene also needs to be improved, by developing a process that ensures increased adhesion with the substrate.

This work has laid the foundation for future research towards development of the laser itself.

7.2   Outlook

In the course of this work, the following strategy for improvements of the materials has been identified:

- The acquisition of suitable stirring equipment, is a first step towards ensuring uniform particle distribution in the glass. As a first step manual stirring is sufficient, and if it turns out to be effective, mechanical stirring of the glass also in the furnace, would be beneficial.

- As a reduced particle size results in lower Rayleigh scattering, reducing the particle size below the current size in the μ m range to sizes in the nm range, will result in less scattering loss.

- As Cr:ZnS has a dissociation temperature higher than that of Cr:ZnSe, incorporation of Cr:ZnS powder into the glass might reduce the problem of dissociation.

- Soft baking in a furnace instead of on a hotplate, will remove the problem of varying thickness and thermal conductivity of he substrates used for graphene transfer.

A   APPENDIX

A.1   Calculation of emission cross-section

Matlab script for integration over the emission curve, using the built in function trapz:

```
1  EmissionSpectra_25 = load('NZP-25-25.txt'); % Loads the emission
       spectra
2
3  Wavelength = EmissionSpectra_25(:,1); % in units nm
4  Wavelength = 10^-7.*Wavelength; % in units cm
5
6  Intensity = EmissionSpectra_25(:,2); % in units V
7  Intensity = 10^3.*Intensity; % in units mV
8
9  Intensity_Wavelength = Intensity.*Wavelength;
10 Integral = trapz(Wavelength, Intensity_Wavelength) % Prints the value
       of the integral
11
12 plot(Wavelength, Emission_crossection) % Plots the emission cross-
       section spectrum
13 xlabel('Wavelength / cm')
14 ylabel('Emission cross-section / mV/cm^2')
```

Calculation of emission cross-section:

$I(2000\,\mathrm{nm}) = 20.8\,\mathrm{mV}$

$I(2200\,\mathrm{nm}) = 11.8\,\mathrm{mV}$

$I(2400\,\mathrm{nm} = 6.0\,\mathrm{mV}$

$\int I(\lambda)\lambda d\lambda = 2.0 \cdot 10^7\,\mathrm{mV\,nm^2} = 2.0 \cdot 10^{-7}\,\mathrm{mV\,cm^2}$.

$\tau_{rad} = 4.7\mathrm{\mu s}$

$n = 1.52$

$$\sigma_{em}(2000\,\mathrm{nm}) = \frac{1}{8\pi \cdot 1.52^2 \cdot 3{\cdot}10^{10}\,\mathrm{cm/s} \cdot 4.7{\cdot}10^{-6}\,\mathrm{s}}\frac{(2{\cdot}10^{-4}\,\mathrm{cm})^5 \cdot 20.8\,\mathrm{mV}}{2.0 \cdot 10^{-7}\,\mathrm{mV\,cm^2}} = 4.1{\cdot}10^{-18}\,\mathrm{cm^2}$$

$$\sigma_{em}(2200\,\mathrm{nm}) = \frac{1}{8\pi \cdot 1.52^2 \cdot 3{\cdot}10^{10}\,\mathrm{cm/s} \cdot 4.7{\cdot}10^{-6}\,\mathrm{s}}\frac{(2.2{\cdot}10^{-4}\,\mathrm{cm})^5 \cdot 11.8\,\mathrm{mV}}{2.0 \cdot 10^{-7}\,\mathrm{mV\,cm^2}} = 3.8{\cdot}10^{-18}\,\mathrm{cm^2}$$

$$\sigma_{em}(2400\,\mathrm{nm}) = \frac{1}{8\pi \cdot 1.52^2 \cdot 3{\cdot}10^{10}\,\mathrm{cm/s} \cdot 4.7{\cdot}10^{-6}\,\mathrm{s}}\frac{(2.4{\cdot}10^{-4}\,\mathrm{cm})^5 \cdot 6.0\,\mathrm{mV}}{2.0 \cdot 10^{-7}\,\mathrm{mV\,cm^2}} = 3.0{\cdot}10^{-18}\,\mathrm{cm^2}$$

A.2   Calculation of number density N for gain coefficient estimation

Sample NZP-25-25 contains 10 g pure glass and 1 g Cr:ZnSe. The concentration of Cr^{2+} in Cr:ZnSe is $\sim 0.02wt\%$.

$1\,\mathrm{g}$ Cr:ZnSe contains $0.0002\,\mathrm{g}$ Cr^{2+}.

$n_{\mathrm{Cr}} = \frac{m_{\mathrm{Cr}}}{M_{\mathrm{Cr}}} = \frac{0.0002\,\mathrm{g}}{52.00\,\mathrm{g/mol}} = 3.85 \cdot 10^{-6}\,\mathrm{mol}$

Number of Cr^{2+} atoms incorporated into the glass:

$N_{\mathrm{Cr}} = n_{\mathrm{Cr}} N_A = 3.85 \cdot 10^{-6}\,\mathrm{mol} \cdot 6.022 \cdot 10^{23}\,/\mathrm{mol} = 2.32 \cdot 10^{18}$

The density of ZnSe is $\rho_{\mathrm{ZnSe}} = 5.27\,\mathrm{g/cm^3}$ [108], while the density of pure phosphate glass is about $\rho_{glass} = 2.9\,\mathrm{g/cm^3}$ [100]. The values are taken as the density of the material with Cr^{2+} ions and Cr:ZnSe crystals incorporated, respectively.

$1\,\mathrm{g}$ Cr:ZnSe has a volume $V_{\mathrm{ZnSe}} = \frac{m_{\mathrm{ZnSe}}}{\rho_{\mathrm{ZnSe}}} = \frac{1\,\mathrm{g}}{5.27\,\mathrm{g/cm^3}} = 0.19\,\mathrm{cm^3}$ The number density of Cr^{2+} in Cr:ZnSe is $\rho_{N,ZnSe} = \frac{N_{\mathrm{Cr}}}{V_{\mathrm{ZnSe}}} = \frac{2.32 \cdot 10^{18}}{0.19\,\mathrm{cm^3}} = 1.22 \cdot 10^{19}\,\mathrm{cm^{-3}}$ This is the maximum achievable concentration of Cr^{2+} ions using this material.

$10\,\mathrm{g}$ NZP glass has a volume $V_{\mathrm{glass}} = \frac{m_{\mathrm{glass}}}{\rho_{\mathrm{glass}}} = \frac{10\,\mathrm{g}}{2.9\,\mathrm{g/cm^3}} = 3.45\,\mathrm{cm^3}$ This is a crude estimate, as the volume will increase with incorporated Cr:ZnSe. The number density of Cr^{2+} in NZP glass is $\rho_{N,glass} = \frac{N_{\mathrm{Cr}}}{V_{\mathrm{glass}}} = \frac{2.32 \cdot 10^{18}}{3.45\,\mathrm{cm^3}} = 6.72 \cdot 10^{17}\,\mathrm{cm^{-3}}$ This is the concentration of Cr^{2+} ion in a material with uniform dispersion of Cr:ZnSe particles.

As the fluorescence spectra were obtained by focusing directly on Cr:ZnSe agglomerations, the effective Cr^{2+} concentration in the area is estimated at about $5 \cdot 10^{18}\,\mathrm{cm^{-3}}$, higher than for a uniform distribution, but lower than for pure Cr:ZnSe.

A.3 Calculation of gain coefficient

$g(2000\,\mathrm{nm}) = 4.1 \cdot 10^{-18}\,\mathrm{cm^2} \cdot 0.2 \cdot 5 \cdot 10^{18}\,\mathrm{cm^{-3}} = 4.1\,\mathrm{cm^{-1}}$

$g(2200\,\mathrm{nm}) = 3.8 \cdot 10^{-18}\,\mathrm{cm^2} \cdot 0.2 \cdot 5 \cdot 10^{18}\,\mathrm{cm^{-3}} = 3.8\,\mathrm{cm^{-1}}$

$g(2400\,\mathrm{nm}) = 3.0 \cdot 10^{-18}\,\mathrm{cm^2} \cdot 0.2 \cdot 5 \cdot 10^{18}\,\mathrm{cm^{-3}} = 3.0\,\mathrm{cm^{-1}}$

A.4 Calculation of saturation intensity

$I_{sat}(2000\,\mathrm{nm}) = \frac{6.63 \cdot 10^{-34}\,\mathrm{Js} \cdot 3 \cdot 10^{10}\,\mathrm{cm/s}}{2 \cdot 10^{-4}\,\mathrm{cm} \cdot 4.1 \cdot 10^{-18}\,\mathrm{cm^2} \cdot 4.7 \cdot 10^{-6}\,\mathrm{s}} = 5136\,\mathrm{W/cm^2} = 5.1\,\mathrm{kW/cm^2}$

$I_{sat}(2200\,\mathrm{nm}) = \frac{6.63 \cdot 10^{-34}\,\mathrm{Js} \cdot 3 \cdot 10^{10}\,\mathrm{cm/s}}{2.2 \cdot 10^{-4}\,\mathrm{cm} \cdot 3.8 \cdot 10^{-18}\,\mathrm{cm^2} \cdot 4.7 \cdot 10^{-6}\,\mathrm{s}} = 5102\,\mathrm{W/cm^2} = 5.1\,\mathrm{kW/cm^2}$

$I_{sat}(2400\,\mathrm{nm}) = \frac{6.63 \cdot 10^{-34}\,\mathrm{Js} \cdot 3 \cdot 10^{10}\,\mathrm{cm/s}}{2.4 \cdot 10^{-4}\,\mathrm{cm} \cdot 3.0 \cdot 10^{-18}\,\mathrm{cm^2} \cdot 4.7 \cdot 10^{-6}\,\mathrm{s}} = 5917\,\mathrm{W/cm^2} = 5.9\,\mathrm{kW/cm^2}$

A.5 Calculation of losses

$L_1 = 2.48\,\mathrm{mm} = 0.248\,\mathrm{cm}$

$L_2 = 0.50\,\mathrm{mm} = 0.050\,\mathrm{cm}$

Arbitrary intensity values are chosen to demonstrate calculations. At $\lambda = 2.4\,\mathrm{\mu m}$:

$I_1 = 5.86\,\mathrm{mW}$

$I_2 = 8.34\,\mathrm{mW}$

Loss calculation (dB/cm):

$\alpha(2.4\,\mathrm{\mu m}) = \frac{10}{0.248\,\mathrm{cm} - 0.050\,\mathrm{cm}} \log_{10}\left(\frac{8.34}{5.86}\right) = 7.74\,\mathrm{dB/cm}$

Absorption coefficient calculation (cm^{-1}):

$T = \frac{I}{I_0} = R \cdot e^{-\alpha l} \implies$ [9]

$\frac{I_2}{I_1} = \frac{e^{-\alpha l_2}}{e^{-\alpha l_1}} = e^{\alpha(l_1 - l_2)} \implies$

$\alpha = \frac{1}{l_1 - l_2} \ln\left(\frac{I_2}{I_1}\right)$

$\alpha = \frac{1}{0.248\,\text{cm} - 0.05\,\text{cm}} \ln\left(\frac{8.34}{5.86}\right) = 1.78\,\text{cm}^{-1}$

A.6 Curve fitting of blackbody radiation

Curve fitting was done using this script [109]:

```
1  % Iterative fit to an experimentally measured blackbody spectrum
2  % to determine the color temperature (in K) and the emissivity.
3  % Uses the fitblackbody.m function.
4  % T. C. O'Haver, May 2008
5  format compact
6  global emissivity
7
8  % Enter data
9  A = load('MR1_SiO2_032_CVD_036_CVD_D1426_532nm_Area0_1100-3200
        _10sec_50perc_Copy.txt');
10 shift = A(:,1);
11 counts = A(:,2);
12 minimum = min(counts);
13
14 data_length = length(shift);
15 i = 0;
16 wavelengthshift = shift;
17 newcounts = counts;
18 for i = 1:data_length
19     wavelengthshift(i) = 10000000/shift(i); % to convert from cm to
            nm
20     newcounts(i) = counts(i) - minimum + 1000; %subtract the
            background, ish
21 end
22
23 wavelength = transpose(wavelengthshift); % Wavelength in nm
24 radiance = transpose(newcounts); % counts
25
26 % Perform an iterative fit using FMINSEARCH and fitblackbody.m
27 start=3000;   % generic initial guess for blackbody temperature
28 options = optimset('TolX',0.1);  % Determines how close the model
        must fit the data
29 Temperature=fminsearch('fitblackbody',start,options,wavelength,
        radiance);
30
31 % Compute a model and plot it (blue line) along with
32 % the original data (red points)
```

---

[9]where R is the Fresnel reflection from the glass surface.

```
33  model=emissivity.*1.19111E+16*wavelength.^(−5)./( exp (14380000./(
        wavelength*Temperature))−1);
34  plot (wavelength, radiance, 'r.', wavelength, model, 'b')
35  xlabel ( 'Wavelength / nm' )
36  ylabel ('Radiance / W/cm^2/sr ')
37  emissivity
38  Temperature
```

The function fitblackbody.m:

```
1  function err = fitblackbody (lambda, wavelength, y, handle )
2  %  Fitting function for a blackbody spectrum.
3  %  T. C. O'Haver, May 2008
4  global emissivity
5  radiance = 1.19111E+16*wavelength.^(−5)./( exp (14380000./( wavelength*
        lambda))−1);
6  emissivity = radiance '\y';
7  z = radiance*emissivity;
8  err = norm (z−y);
```

A.7 Calculation of saturation energy fluence for graphene

$w = 100\,\text{nm}$

$A = \pi w^2 = \pi \cdot (100\mu\,\text{m})^2 = \pi \cdot (1 \cdot 10^{-4}\,\text{m})^2 = 3.14 \cdot 10^{-8}\,\text{m}^2$

$T_{oc} = 0.08\%$, $T_{is} = 0.7\%$

$F_{rep} = 250\,\text{MHz} = 2.50 \cdot 10^8\,\text{Hz}$

Calculation of saturation energy fluence:

$P_{out} = 21\,\text{mW} = 0.021\,\text{W}$

$P_{intra} = \frac{P_{out}}{T_{oc}T_{is}} = \frac{21 \cdot 10^{-3}\,\text{W}}{0.7 \cdot 0.08} = 0.375\,\text{W}$

$E_{intra} = \frac{P_{intra}}{F_{rep}} = \frac{0.375\,\text{W}}{2.50 \cdot 10^8\,\text{Hz}} = 1.1 \cdot 10^{-9}\,\text{J}$

$J_{sat} = \frac{E_{intra}}{A} = \frac{1.1 \cdot 10^{-9}\,\text{J}}{3.14 \cdot 10^{-8}\,\text{m}^2} = 0.048\,\text{J/m}^2 = 4.8\mu\,\text{J/cm}^2$

Calculation of maximum energy fluence:

$P_{out} = 130\,\text{mW} = 0.130\,\text{W}$

$P_{intra} = \frac{P_{out}}{T_{oc}T_{is}} = \frac{0.130\,\text{W}}{0.7 \cdot 0.08} = 2.32\,\text{W}$

$E_{intra} = \frac{P_{intra}}{F_{rep}} = \frac{2.32\,\text{W}}{2.50 \cdot 10^8\,\text{Hz}} = 9.3 \cdot 10^{-9}\,\text{J}$

$J_{sat} = \frac{E_{intra}}{A} = \frac{9.3 \cdot 10^{-9}\,\text{J}}{3.14 \cdot 10^{-8}\,\text{m}^2} = 0.30\,\text{J/m}^2 = 30\mu\,\text{J/cm}^2$

References

[1] Wei Shi, Qiang Fang, Xiushan Zhu, R. A. Norwood, and N. Peyghambarian. Fiber lasers and their applications. *Appl. Opt.*, 53(28):6554–6568, Oct 2014.

[2] E. V. Browell, T. D. Wilkerson, and T. J. Mcilrath. Water vapor differential absorption lidar development and evaluation. *Appl. Opt.*, 18(20):3474–3483, Oct 1979.

[3] VV Dvoyrin, VM Mashinsky, LI Bulatov, IA Bufetov, AV Shubin, MA Melkumov, EF Kustov, EM Dianov, AA Umnikov, VF Khopin, et al. Bismuth-doped-glass optical fibers—a new active medium for lasers and amplifiers. *Optics letters*, 31(20):2966–2968, 2006.

[4] Vladislav V Dvoyrin, Alexander V Kir'yanov, Valery M Mashinsky, Oleg I Medvedkov, Andrey A Umnikov, Alexei N Guryanov, and Evgeny M Dianov. Absorption, gain, and laser action in bismuth-doped aluminosilicate optical fibers. *IEEE Journal of Quantum Electronics*, 46(2):182–190, 2010.

[5] Nikolai Tolstik, Evgeni Sorokin, and Irina T. Sorokina. Graphene mode-locked cr:zns laser with 41 fs pulse duration. *Opt. Express*, 22(5):5564–5571, Mar 2014.

[6] Nikolai Tolstik, Andreas Pospischil, Evgeni Sorokin, and Irina T. Sorokina. Graphene mode-locked cr:zns chirped-pulse oscillator. *Opt. Express*, 22(6):7284–7289, Mar 2014.

[7] Grzegorz Sobon, Jaroslaw Sotor, Iwona Pasternak, Aleksandra Krajewska, Wlodek Strupinski, and Krzysztof M. Abramski. Thulium-doped all-fiber laser mode-locked by cvd-graphene/pmma saturable absorber. *Opt. Express*, 21(10):12797–12802, May 2013.

[8] EV Karaksina, VG Plotnichenko, RA Mironov, RM Shaposhnikov, and LA Ketkova. The composite materials on the basis of as2s3 glass containing crystals zns and zns doped with cr (2+). *Journal of Optoelectronics and Advanced Materials*, 13(11):1433, 2011.

[9] EV Karaksina, VS Shiryaev, and LA Ketkova. Preparation of composite materials for fiber optics based on chalcogenide glasses containing zns (znse): Cr (2+) crystals. *Journal of Non-Crystalline Solids*, 377:220–224, 2013.

[10] EV Karaksina, LA Ketkova, MF Churbanov, and EM Dianov. Preparation of mid-ir-active as2s3/zns (znse): Cr2+ composites. *Inorganic Materials*, 49(3):223–229, 2013.

[11] Orazio Svelto. *Principles of Lasers*, chapter 1. Introductory Concepts. Springer US, 2010.

[12] Jun Dong, Michael Bass, Yanli Mao, Peizhen Deng, and Fuxi Gan. Dependence of the yb3+ emission cross section and lifetime on temperature and concentration in yttrium aluminum garnet. *J. Opt. Soc. Am. B*, 20(9):1975–1979, Sep 2003.

[13] T. Schweizer, D. W. Hewak, B. N. Samson, and D. N. Payne. Spectroscopic data of the 1.8-, 2.9-, and 4.3-um transitions in dysprosium-doped gallium lanthanum sulfide glass. *Opt. Lett.*, 21(19):1594–1596, Oct 1996.

[14] W. Koechner. *Solid-State Laser Engineering*, chapter 1. Energy Transfer Between Radiation and Atomic Transitions. Springer, 2006.

[15] Orazio Svelto. *Principles of Lasers*, chapter 2. Interaction of Radiation with Atoms and Ions. Springer US, 2010.

[16] M. Bass W. Koechner. *Solid-State Lasers*, chapter 9. Mode-Locking. Springer, 2003.

[17] Dan Wilkins F. Graham Smith, Terry A. King. *Optics and Photonics*, chapter 16. Laser Light. Wiley, 2007.

[18] Dan Wilkins F. Graham Smith, Terry A. King. *Optics and Photonics*, chapter 4. Periodic and Non-Periodic Waves. Wiley, 2007.

[19] Amos Martinez and Zhipei Sun. Nanotube and graphene saturable absorbers for fibre lasers. *Nature Photonics*, 7(11):842–845, 2013.

[20] Saturable Absorbers rp photonics. `https://www.rp-photonics.com/saturable_absorbers.html`. Accessed: 2017-08-22.

[21] W. Koechner. *Solid-State Laser Engineering*, chapter 2. Properties of Solid-State Laser Materials. Springer, 2006.

[22] Baldassare Di Bartolo. *Optical Interactions in Solids, Second Edition*, chapter 6. The Magnetic Ion in a Crystal: The Role of Symmetry. World Scientific, 2010.

[23] Selection rules and transition moment integral libretexts. `https://chem.libretexts.org/Core/Physical_and_Theoretical_Chemistry/Spectroscopy/Fundamentals_of_Spectroscopy/Selection_rules_and_transition_moment_integral`. Accessed: 2017-06-14.

[24] Baldassare Di Bartolo. *Optical Interactions in Solids, Second Edition*, chapter 17. Vibrational-Electronic Interaction and Spectra. World Scientific, 2010.

[25] Gerard Panczer Michael Gaft, Renata Reisfeld. *Modern Luminescence Spectroscopy of Minerals and Materials*, chapter 2. Theoretical Background. Springer, 2015.

[26] E. Sorokin, S. Naumov, and I. T. Sorokina. Ultrabroadband infrared solid-state lasers. *IEEE Journal of Selected Topics in Quantum Electronics*, 11(3):690–712, May 2005.

[27] Evgeni Sorokin. *Solid-State Materials for Few-Cycle Pulse Generation and Amplification*, pages 3–73. Springer Berlin Heidelberg, Berlin, Heidelberg, 2004.

[28] Refka Oueslati Omrani, Saida Krimi, Jean Jacques Videau, Ismail Khattech, Abdelaziz El Jazouli, and Mohamed Jemal. Structural and thermochemical study of na2o–zno–p2o5 glasses. *Journal of Non-Crystalline Solids*, 390:5 – 12, 2014.

[29] Richard K Brow. Review: the structure of simple phosphate glasses. *Journal of Non-Crystalline Solids*, 263:1 – 28, 2000.

[30] Lionel Montagne, Gérard Palavit, and Rodolphe Delaval. 31p nmr in (100 - x)(napo3)-xzno glasses. *Journal of Non-Crystalline Solids*, 215(1):1 – 10, 1997.

[31] YUO Barrncnkov, C Sifuentes, and AN Starodumov. Cds and cdse semiconductor nanocrystal doped glasses and their application in fiber-optic sensors. 2000.

[32] N. F. Borrelli, D. W. Hall, H. J. Holland, and D. W. Smith. Quantum confinement effects of semiconducting microcrystallites in glass. *Journal of Applied Physics*, 61(12):5399–5409, 1987.

[33] N. Vivet, J.L. Doualan, M. Morales, and M. Levalois. Luminescence properties of cr2+:znse: Comparison between a single crystal and a film deposited by rf magnetron co-sputtering. *Journal of Luminescence*, 130(8):1449 – 1454, 2010.

[34] L. D. DeLoach, R. H. Page, G. D. Wilke, S. A. Payne, and W. F. Krupke. Transition metal-doped zinc chalcogenides: spectroscopy and laser demonstration of a new class of gain media. *IEEE Journal of Quantum Electronics*, 32(6):885–895, Jun 1996.

[35] Irina T Sorokina. Cr2+-doped ii–vi materials for lasers and nonlinear optics. *Optical Materials*, 26(4):395 – 412, 2004. Third International Symposium on Lasers and Nonlinear Optical Materials (ISLNOM-3).

[36] S. Mirov, V. Fedorov, I. Moskalev, M. Mirov, and D. Martyshkin. Frontiers of mid-infrared lasers based on transition metal doped ii–vi semiconductors. *Journal of Luminescence*, 133:268 – 275, 2013. 16th International Conference on Luminescence ICL'11.

[37] A.V. Podlipensky, V.G. Shcherbitsky, N.V. Kuleshov, V.I. Levchenko, V.N. Yakimovich, M. Mond, E. Heumann, G. Huber, H. Kretschmann, and S. Kück. Efficient laser operation and continuous-wave diode pumping of cr2+:znse single crystals. *Applied Physics B*, 72(2):253–255, 2001.

[38] A. Burger, K. Chattopadhyay, J.-O. Ndap, X. Ma, S.H. Morgan, C.I. Rablau, C.-H. Su, S. Feth, Ralph H. Page, Kathleen I. Schaffers, and Stephen A. Payne. Preparation conditions of chromium doped znse and their infrared luminescence properties. *Journal of Crystal Growth*, 225(2–4):249 – 256, 2001. Proceedings of the 12th American Conference on Crystal Growth and Epitaxy.

[39] Sadao Adachi and Tsunemasa Taguchi. Optical properties of znse. *Phys. Rev. B*, 43:9569–9577, Apr 1991.

[40] L. D. DeLoach, R. H. Page, G. D. Wilke, S. A. Payne, and W. F. Krupke. Transition metal-doped zinc chalcogenides: spectroscopy and laser demonstration of a new class of gain media. *IEEE Journal of Quantum Electronics*, 32(6):885–895, Jun 1996.

[41] Ursula Keller, Kurt J Weingarten, Franz X Kartner, Daniel Kopf, Bernd Braun, Isabella D Jung, Regula Fluck, Clements Honninger, Nicolai Matuschek, and J Aus Der Au. Semiconductor saturable absorber mirrors (sesam's) for femtosecond to nanosecond pulse generation in solid-state lasers. *IEEE Journal of selected topics in QUANTUM ELECTRONICS*, 2(3):435–453, 1996.

[42] In Hyung Baek, Sun Young Choi, Hwang Woon Lee, Won Bae Cho, Valentin Petrov, Antonio Agnesi, Valdas Pasiskevicius, Dong-Il Yeom, Kihong Kim, and Fabian Rotermund. Single-walled carbon nanotube saturable absorber assisted high-power mode-locking of a ti:sapphire laser. *Opt. Express*, 19(8):7833–7838, Apr 2011.

[43] Andreas Schmidt, Philipp Koopmann, Günter Huber, Peter Fuhrberg, Sun Young Choi, Dong-Il Yeom, Fabian Rotermund, Valentin Petrov, and Uwe Griebner. 175 fs tm:lu2o3 laser at 2.07 um mode-locked using single-walled carbon nanotubes. *Opt. Express*, 20(5):5313–5318, Feb 2012.

[44] M. N. Cizmeciyan, J. W. Kim, S. Bae, B. H. Hong, F. Rotermund, and A. Sennaroglu. Graphene mode-locked femtosecond cr:znse laser at 2500 nm. *Opt. Lett.*, 38(3):341–343, Feb 2013.

[45] In Hyung Baek, Hwang Woon Lee, Sukang Bae, Byung Hee Hong, Yeong Hwan Ahn, Dong-Il Yeom, and Fabian Rotermund. Efficient mode-locking of sub-70-fs ti: sapphire laser by graphene saturable absorber. *Applied Physics Express*, 5(3):032701, 2012.

[46] Jin-Long Xu, Xian-Lei Li, Yong-Zhong Wu, Xiao-Peng Hao, Jing-Liang He, and Ke-Jian Yang. Graphene saturable absorber mirror for ultra-fast-pulse solid-state laser. *Optics letters*, 36(10):1948–1950, 2011.

[47] Charles J Koester and Elias Snitzer. Amplification in a fiber laser. *Applied optics*, 3(10):1182–1186, 1964.

[48] SB Poole, David N Payne, and M E Fermann. Fabrication of low-loss optical fibres containing rare-earth ions. *Electronics Letters*, 21(17):737–738, 1985.

[49] DS Funk, JW Carlson, and JG Eden. Ultraviolet (381 nm), room temperature laser in neodymium-doped fluorozirconate fibre. *Electronics Letters*, 30(22):1859–1860, 1994.

[50] P. F. Moulton, G. A. Rines, E. V. Slobodtchikov, K. F. Wall, G. Frith, B. Samson, and A. L. G. Carter. Tm-doped fiber lasers: Fundamentals and power scaling. *IEEE Journal of Selected Topics in Quantum Electronics*, 15(1):85–92, Jan 2009.

[51] Business news optics.org. `http://optics.org/news/3/10/44`. Accessed: 2017-08-16.

[52] Jihong Geng, Sean Staines, Zuolan Wang, Jie Zong, Mike Blake, and Shibin Jiang. Highly stable low-noise brillouin fiber laser with ultranarrow spectral linewidth. *IEEE Photonics Technology Letters*, 18(17):1813–1815, 2006.

[53] Alexander Sell, Günther Krauss, Rüdiger Scheu, Rupert Huber, and Alfred Leitenstorfer. 8-fs pulses from a compact er: fiber system: quantitative modeling and experimental implementation. *Optics express*, 17(2):1070–1077, 2009.

[54] Günther Krauss, Sebastian Lohss, Tobias Hanke, Alexander Sell, Stefan Eggert, Rupert Huber, and Alfred Leitenstorfer. Synthesis of a single cycle of light with compact erbium-doped fibre technology. *Nature Photonics*, 4(1):33–36, 2010.

[55] K Kieu, R Jason Jones, and N Peyghambarian. Generation of few-cycle pulses from an amplified carbon nanotube mode-locked fiber laser system. *IEEE Photonics Technology Letters*, 22(20):1521–1523, 2010.

[56] Evgenii M Dianov, VV Dvoyrin, Valerii Mikhailovich Mashinsky, Andrei Aleksandrovich Umnikov, Mikhail Viktorovich Yashkov, and Aleksei Nikolaevich Gur'yanov. Cw bismuth fibre laser. *Quantum Electronics*, 35(12):1083, 2005.

[57] I A Bufetov and E M Dianov. Bi-doped fiber lasers. *Laser Physics Letters*, 6(7):487, 2009.

[58] Eugeny M. Dianov, Alexandr A. Krylov, Vladislav V. Dvoyrin, Valery M. Mashinsky, Peter G. Kryukov, Oleg G. Okhotnikov, and Mircea Guina. Mode-locked bi-doped fiber laser. *J. Opt. Soc. Am. B*, 24(8):1807–1808, Aug 2007.

[59] JE Aronson, CR Haythornthwaite, DW Hewak, and WS Brocklesby. Optical spectroscopy of cr4+-doped chalcogenide glasses. 2004.

[60] Diederik S. Wiersma. The physics and applications of random lasers. *Nature Physics*, (4):359–367, 2008.

[61] V M Markushev, V F Zolin, and Ch M Briskina. Luminescence and stimulated emission of neodymium in sodium lanthanum molybdate powders. *Soviet Journal of Quantum Electronics*, 16(2):281, 1986.

[62] V. I. Klimov, A. A. Mikhailovsky, Su Xu, A. Malko, J. A. Hollingsworth, C. A. Leatherdale, H.-J. Eisler, and M. G. Bawendi. Optical gain and stimulated emission in nanocrystal quantum dots. *Science*, 290(5490):314–317, 2000.

[63] IrinaT. Sorokina, Evgeni Sorokin, Victor G. Shcherbitsky, Nikolai V. Kuleshov, Guohua Zhu, and M. A. Noginov. Room-temperature lasing in nanocrystalline cr2+:znse random laser. In *Advanced Solid-State Photonics (TOPS)*, page 376. Optical Society of America, 2004.

[64] Irina T. Sorokina, Evgeni Sorokin, Victor Shcherbitsky, Nikolai V. Kuleshov, Guohua Zhu, A. Franz, and M A. Noginov. Novel mid-infrared random power lasers: Cr2+:zns vs. cr2+:znse. In *Conference on Lasers and Electro-Optics/International Quantum Electronics Conference and Photonic Applications Systems Technologies*, page IThG22. Optical Society of America, 2004.

[65] Mikhail A. Noginov, Guohua Zhu, and Ichesia Fowlkes. Fiber-coupled random laser. In *Conference on Lasers and Electro-Optics/International Quantum Electronics Conference*

and Photonic Applications Systems Technologies, page IFB1. Optical Society of America, 2004.

[66] Roman A Mironov, E V Karaksina, A O Zabezhailov, R M Shapashnikov, M F Churbanov, and Evgenii M Dianov. Mid-ir luminescence of cr 2+ : Ii — vi crystals in chalcogenide glass fibres. *Quantum Electronics*, 40(9):828, 2010.

[67] D. V. Martyshkin, J. T. Goldstein, V. V. Fedorov, and S. B. Mirov. Crystalline cr2+:znse/chalcogenide glass composites as active mid-ir materials. *Opt. Lett.*, 36(9):1530–1532, May 2011.

[68] Gregory J. Wagner, Timothy J. Carrig, Ralph H. Page, Kathleen I. Schaffers, Jean-Oliver Ndap, Xiaoyan Ma, and Arnold Burger. Continuous-wave broadly tunable cr2+:znse laser. *Opt. Lett.*, 24(1):19–21, Jan 1999.

[69] M. Natali Cizmeciyan, Huseyin Cankaya, Adnan Kurt, and Alphan Sennaroglu. Kerr-lens mode-locked femtosecond cr2+:znse laser at 2420 nm. *Opt. Lett.*, 34(20):3056–3058, Oct 2009.

[70] Irina T. Sorokina, Evgeni Sorokin, and Timothy Carrig. Femtosecond pulse generation from a sesam mode-locked cr:znse laser. In *Conference on Lasers and Electro-Optics/Quantum Electronics and Laser Science Conference and Photonic Applications Systems Technologies*, page CMQ2. Optical Society of America, 2006.

[71] Tawfique Hasan, Zhipei Sun, Fengqiu Wang, Francesco Bonaccorso, Ping Heng Tan, Aleksey G Rozhin, and Andrea C Ferrari. Nanotube–polymer composites for ultrafast photonics. *Advanced Materials*, 21(38-39):3874–3899, 2009.

[72] Qiaoliang Bao, Han Zhang, Yu Wang, Zhenhua Ni, Yongli Yan, Ze Xiang Shen, Kian Ping Loh, and Ding Yuan Tang. Atomic-layer graphene as a saturable absorber for ultrafast pulsed lasers. *Advanced Functional Materials*, 19(19):3077–3083, 2009.

[73] Gongwen Zhu, Xiushan Zhu, Kaushik Balakrishnan, Robert A. Norwood, and N. Peyghambarian. Fe2+:znse and graphene q-switched singly ho3+-doped zblan fiber lasers at 3 μm. *Opt. Mater. Express*, 3(9):1365–1377, Sep 2013.

[74] Pi Ling Huang, Shau-Ching Lin, Chao-Yung Yeh, Hsin-Hui Kuo, Shr-Hau Huang, Gong-Ru Lin, Lain-Jong Li, Ching-Yuan Su, and Wood-Hi Cheng. Stable mode-locked fiber laser based on cvd fabricated graphene saturable absorber. *Optics express*, 20(3):2460–2465, 2012.

[75] Samuele Davide Di Dio Cafiso, Elena Ugolotti, Andreas Schmidt, Valentin Petrov, Uwe Griebner, Antonio Agnesi, Won Bae Cho, Bo Hee Jung, Fabian Rotermund, Sukang Bae, Byung Hee Hong, Giancarlo Reali, and Federico Pirzio. Sub-100-fs cr:yag laser mode-locked by monolayer graphene saturable absorber. *Opt. Lett.*, 38(10):1745–1747, May 2013.

[76] D. Popa, Z. Sun, F. Torrisi, T. Hasan, F. Wang, and A. C. Ferrari. Sub 200 fs pulse generation from a graphene mode-locked fiber laser. *Applied Physics Letters*, 97(20):203106, 2010.

[77] Zhipei Sun, Tawfique Hasan, Felice Torrisi, Daniel Popa, Giulia Privitera, Fengqiu Wang, Francesco Bonaccorso, Denis M. Basko, and Andrea C. Ferrari. Graphene mode-locked ultrafast laser. *ACS Nano*, 4(2):803–810, 2010. PMID: 20099874.

[78] Han Zhang, Dingyuan Tang, R. J. Knize, Luming Zhao, Qiaoliang Bao, and Kian Ping Loh. Graphene mode locked, wavelength-tunable, dissipative soliton fiber laser. *Applied Physics Letters*, 96(11):111112, 2010.

[79] Seonyeong Kim, Somyeong Shin, Taekwang Kim, Hyewon Du, Minho Song, ChangWon Lee, Kisoo Kim, Seungmin Cho, David H. Seo, and Sunae Seo. Robust graphene wet transfer process through low molecular weight polymethylmethacrylate. *Carbon*, 98:352 – 357, 2016.

[80] Nano PMMA and Copolymer microchem. `http://microchem.com/pdf/PMMA_Data_Sheet.pdf`. Accessed: 2017-06-01.

[81] J. F. Muth, J. H. Lee, I. K. Shmagin, R. M. Kolbas, H. C. Casey Jr., B. P. Keller, U. K. Mishra, and S. P. DenBaars. Absorption coefficient, energy gap, exciton binding energy, and recombination lifetime of gan obtained from transmission measurements. *Applied Physics Letters*, 71(18):2572–2574, 1997.

[82] K Jinguji, Masaharu Horiguchi, and T Manabe. Spectral loss measurement system for ir optical fibers. *Applied optics*, 21(4):571–572, 1982.

[83] T.R. Crompton. *Thermal Methods of Polymer Analysis*, chapter 7. Differential Scanning Calorimetry. Smithers Rapra Technology, 2013.

[84] Peter Larkin. *Infrared and Raman Spectroscopy*, chapter 2. Basic Principles. Elsevier, 2011.

[85] What Raman spectroscopy can tell youl renishaw. `http://www.renishaw.com/en/what-raman-spectroscopy-can-tell-you--25800l`. Accessed: 2017-08-05.

[86] F. L. Galeener and J. C. Mikkelsen. The Raman spectra and structure of pure vitreous P$_2$O$_5$. *Solid State Communications*, 30:505–510, May 1979.

[87] Junmo Koo, Byeong-Soo Bae, and Hoon-Kyun Na. Raman spectroscopy of copper phosphate glasses. *Journal of Non-Crystalline Solids*, 212(2):173 – 179, 1997.

[88] J.J. Hudgens, R.K. Brow, D.R. Tallant, and S.W. Martin. Raman spectroscopy study of the structure of lithium and sodium ultraphosphate glasses. *Journal of Non-Crystalline Solids*, 223(1):21 – 31, 1998.

[89] S. S. Mitra, O. Brafman, W. B. Daniels, and R. K. Crawford. Pressure-induced phonon frequency shifts measured by raman scattering. *Phys. Rev.*, 186:942–944, Oct 1969.

[90] D Nesheva, MJ # 138cepanovic, S Askrabic, Z Levi, I Bineva, and ZV Popovic. Raman scattering from znse nanolayers. *Acta Physica Polonica-Series A General Physics*, 116(1):75, 2009.

[91] Brajesh K. Rai, R. S. Katiyar, K.-T. Chen, and A. Burger. Raman and photoluminescence studies on intrinsic and cr-doped znse single crystals. *Journal of Applied Physics*, 83(11):6011–6017, 1998.

[92] Isaac Childres, Luis A Jauregui, Wonjun Park, Helin Cao, and Yong P Chen. Raman spectroscopy of graphene and related materials. *New developments in photon and materials research*, 1, 2013.

[93] Autocorrelators rp photonics encyclopedia. `https://www.rp-photonics.com/autocorrelators.html`. Accessed: 2017-08-11.

[94] K. Sala, G. Kenney-Wallace, and G. Hall. Cw autocorrelation measurements of picosecond laser pulses. *IEEE Journal of Quantum Electronics*, 16(9):990–996, September 1980.

[95] ZnSe MSDS thor labs. `https://www.thorlabs.com/images/tabimages/Zinc-Selenide_MSDS.pdf`. Accessed: 2017-08-07.

[96] Buy Graphene Films graphenea. `https://www.graphenea.com/collections/buy-graphene-films`. Accessed: 2017-05-30.

[97] 1. What are e-beam resists composed of, and how do they work? allresist. `http://www.allresist.com/faq-ebeamresists-compositing/`. Accessed: 2017-06-01.

[98] Irina Sorokina. personal communication.

[99] M Haouari, M Ajroud, H Ben Ouada, H Maaref, A Brenier, and C Garapon. Spectroscopic properties of cr3+-doped phosphate glasses. *physica status solidi (b)*, 215(2):1165–1177, 1999.

[100] Lionel Montagne, Gérard Palavit, and Rodolphe Delaval. Effect of zno on the properties of (100 - x)(napo3)-xzno glasses. *Journal of Non-Crystalline Solids*, 223(1):43 – 47, 1998.

[101] Nikolai Tolstik. personal communication.

[102] Konstantin L. Vodopyanov Irina T. Sorokina. *Solid-state mid-infrared laser sources*. Springer, 2003.

[103] Single Mode Fiber thorlabs. `https://www.thorlabs.com/newgrouppage9.cfm?objectgroup_id=949`. Accessed: 2017-08-20.

[104] A Zakery and S.R Elliott. Optical properties and applications of chalcogenide glasses: a review. *Journal of Non-Crystalline Solids*, 330(1):1 – 12, 2003.

[105] Takashi Harada, Hiroyuki In, Hiromichi Takebe, and Kenji Morinaga. Effect of b2o3 addition on the thermal stability of barium phosphate glasses for optical fiber devices. *Journal of the American Ceramic Society*, 87(3):408–411, 2004.

[106] A J Bell, J M Mestdagh, J Berlande, X Biquard, J Cuvellier, A Lallement, P Meynadier, O Sublemontier, and J P Visticot. Mean cluster size by rayleigh scattering. *Journal of Physics D: Applied Physics*, 26(6):994, 1993.

[107] Buy Graphene Films Processed in Clean Room Class 1000 graphenea. `https://www.graphenea.com/collections/buy-graphene-films/easy-transfer`. Accessed: 2017-08-23.

[108] Zinc Selenide crystran. `https://www.crystran.co.uk/optical-materials/zinc-selenide-znse`. Accessed: 2017-08-20.

[109] File Exchange mathworks. `https://se.mathworks.com/matlabcentral/fileexchange/20129-fit-blackbody-equation-to-spectrum?focused=5101231&tab=function`. Accessed: 2017-08-20.